



UNIVERSIDAD NACIONAL AUTÓNOMA DE MÉXICO  
DOCTORADO EN CIENCIAS FÍSICAS  
INSTITUTO DE FÍSICA

**CHARACTERIZATION OF A WINDOWLESS  
SUPERSONIC GAS JET TARGET FOR NUCLEAR  
PHYSICS EXPERIMENTS**

DOCTORADO DIRECTO  
QUE PARA OPTAR POR EL GRADO DE  
DOCTOR EN CIENCIAS FÍSICAS

PRESENTA:  
**JOSÉ FRANCISCO FAVELA PÉREZ**

TUTOR PRINCIPAL:  
EFRAÍN RAFAEL CHÁVEZ LOMELÍ  
**IFUNAM**

MIEMBROS DEL COMITÉ TUTOR:  
GUILLERMO CIRANO ESPINOSA GARCÍA  
**IFUNAM**  
ALEJANDRO FRANK HOEFLICH  
**ICN**

MÉXICO, D.F. ABRIL 2016



Universidad Nacional  
Autónoma de México

Dirección General de Bibliotecas de la UNAM

**Biblioteca Central**



**UNAM – Dirección General de Bibliotecas**  
**Tesis Digitales**  
**Restricciones de uso**

**DERECHOS RESERVADOS ©**  
**PROHIBIDA SU REPRODUCCIÓN TOTAL O PARCIAL**

Todo el material contenido en esta tesis esta protegido por la Ley Federal del Derecho de Autor (LFDA) de los Estados Unidos Mexicanos (México).

El uso de imágenes, fragmentos de videos, y demás material que sea objeto de protección de los derechos de autor, será exclusivamente para fines educativos e informativos y deberá citar la fuente donde la obtuvo mencionando el autor o autores. Cualquier uso distinto como el lucro, reproducción, edición o modificación, será perseguido y sancionado por el respectivo titular de los Derechos de Autor.



Universidad Nacional  
Autónoma de México

Dirección General de Bibliotecas de la UNAM

**Biblioteca Central**



**UNAM – Dirección General de Bibliotecas**  
**Tesis Digitales**  
**Restricciones de uso**

**DERECHOS RESERVADOS ©**  
**PROHIBIDA SU REPRODUCCIÓN TOTAL O PARCIAL**

Todo el material contenido en esta tesis esta protegido por la Ley Federal del Derecho de Autor (LFDA) de los Estados Unidos Mexicanos (México).

El uso de imágenes, fragmentos de videos, y demás material que sea objeto de protección de los derechos de autor, será exclusivamente para fines educativos e informativos y deberá citar la fuente donde la obtuvo mencionando el autor o autores. Cualquier uso distinto como el lucro, reproducción, edición o modificación, será perseguido y sancionado por el respectivo titular de los Derechos de Autor.

- 
1. Reviewer: Dr. Efraín Chávez Lomelí
  
  2. Reviewer: Dr. Armando Varela González
  
  3. Reviewer: Dr. Fernando Salazar Posadas
  
  4. Reviewer: Dra. Catalina Elizabeth Stern Forgach
  
  5. Reviewer: Dr. Andrés Sandoval Espinosa
  
  6. Reviewer: Dr. Eduardo Andrade Ibarra
  
  7. Reviewer: Dr. Edgar Álvarez Zauco

Day of the defense:

Signature from head of PhD committee:



## Abstract

Nuclear data (reaction dynamics, structure) becomes harder to obtain when experiments have to be performed with accelerated particles impinging on nuclei that are found in nature as gases. Sometimes it is possible to produce a solid compound that would contain the nucleus of interest (Hydrides for instances to study reactions on H), or build gas cells with thin windows for noble gases. These and other strategies may not always be appropriate because of the interference of the other materials present in the compound or the windows. It can also be unappropriate because the target may have low density as in the case of windowless gas targets. Gas jets are an optimal solution. In the present work, a new facility developed for the Carlos Graef Fernández Laboratory of the Physics Institute at UNAM (CGFL) is described in detail. The CGFL is a facility powered by a CN-Van de Graaff accelerator. This machine provides light ion beams using voltages up to 5.5MV, ideal for low energy nuclear physics studies. First data on different jets (Air, N, Ar) is presented as well as the study of various excited levels of  $^{12}\text{C}$  in the nuclear reaction  $^{14}\text{N}(d, \alpha)^{12}\text{C}$ . An  $^{16}\text{O}$  resonance was also found and it is reported.

## Resumen

La información sobre el núcleo (dinámica de reacción y estructura) se torna aún más difícil de obtener cuando, en los experimentos desarrollados, los núcleos blanco se encuentran en estado gaseoso. Algunas veces es posible hacer un compuesto sólido del núcleo de interés (hidruros en el caso de reacciones en H), o celdas con ventanas delgadas para casos como gases nobles. Estas y otras estrategias pueden no ser siempre apropiadas debido a la interferencia con los otros materiales, del compuesto o las ventanas de la celda que contenga al gas. Adicionalmente puede no ser apropiado debido a una baja densidad como en el caso de los blancos gaseosos sin ventanas. Los jets de gas son una solución óptima. En este presente trabajo, se muestra una instalación nueva para el laboratorio Carlos Graef Fernández dentro del Instituto de Física de la UNAM. El laboratorio tiene un acelerador de tipo Van de Graaff. Esta máquina provee iones ligeros usando voltajes de hasta 5.5MV, lo cual es ideal para la física nuclear de bajas energías. Se muestran los primeros datos en distintos jets (Aire, Nitrógeno y Argón). También se presenta el estudio de diversos niveles de excitación de  $^{12}\text{C}$  en la reacción nuclear  $^{14}\text{N}(d, \alpha)^{12}\text{C}$ . Una resonancia en  $^{16}\text{O}$  fue encontrada y también se reporta.

A mi familia.

## Acknowledgements

### English

Undoubtedly this work couldn't be conceived without the help and support of **Dr. Dan Shapira**, thank you.

I would like to extend my gratitude to my friends at **VTI**, specially to **Jason Alfrey**, for dedicating part of his time and giving support for making this project a reality.

**Jeff Vasgaard**, from **Pfeiffer Vacuum**, was a great help in finding the correct equipment for our necessities. Thank you for your valuable time and support.

### Español

Sin duda mis padres, **Francisco Luis** y **Hortencia**, y mis hermanas **Diana** y **Karina**, han sido un pilar para mi vida. Gracias!!

Quiero agradecer a mis tíos<sup>1</sup>:

- + **Rubén Darío Favela Meráz**
- **Luis Sergio Favela Meráz**
- **Felipe de Jesús Favela Meráz**
- **Gloria Favela de Palavicini**
- + **Rafael Oscar Favela Meráz**
- + **Víctor Manuel Favela Meráz**

---

<sup>1</sup>+ finado

- + **Héctor Favela Meráz**
- + **Josefina Elva Favela de Silva**
  - **David Fidel Favela Meráz**
  - **Fidel Emiliano Favela Meráz**
  - **José Carlos Favela Meráz**
  - **Francisco Luis Favela Meráz**

Le agradezco de todo corazón a mi tía **Josefina Elva Favela de Silva** quien tuvo una vida ejemplar digna de ser recordada y al igual que mi abuelita **Carmen Meráz de Favela** y mis tíos **Rafael Oscar Favela Meráz**, **Rubén Darío Favela Meráz**, **Héctor Favela Meráz**, **Victor Manuel Favela Meráz**. Serán extrañados.

Con mucho cariño agradezco a mis abuelitos **José** y **Julia Pérez** y a mis tíos **Silvia**, **Olivia**, **Esperanza**, **Carlos** y **José**. Siempre me han hecho sentir querido y bienvenido.

El apoyo del **Dr. Roberto Gleason** para la instalación y el equipamiento del laboratorio fue fundamental para poder hacer el sistema funcional, mis más sinceros agradecimientos por su apoyo y dedicación al proyecto.

Sin duda esta tesis fue realizada en gran parte gracias al apoyo incondicional **Roxana Mitzayé del Castillo Vázquez**, rara vez uno encuentra a una persona tan excelentísima.

**Guillermo Ricarte López**, a quien dedico **toodo** este párrafo para agradecerle exclusivamente a el ;P, por su apoyo y amistad. Gracias amigo! Sin duda **Alejandro Ricarte** y **German Ricarte López** tienen su lugar permanente en mis agradecimientos.

A **Elfego Gutierrez** por su amistad, ayuda y sugerencias. Los cuales ayudaron mucho en los experimentos.

A **Daniel** (Dooky) y **Penélope** (señora Dooky), **Nacho** y **Xoch** por su ayuda y seguimiento a mí persona y al proyecto.

Agradezco a **Samantha Contreras León** por sus consejos, apoyo y paciencia.

A mis compañeros del basquet y amigos **Juan, Ariel, Poncho, Jazmín, Pamela, Yair, Doris, Andrés, Nat, Knelo, Talia, Mauricio, Paulino.** Por proveer un factor distractor importante y por su apoyo en momentos difíciles.

**Arcadio Huerta, O. G. de Lucio, M. E. Ortiz y E. Andrade** por su apoyo en conseguir los recursos y por sus aportaciones de conocimiento técnico durante el montado de la línea y de los experimentos.

**Maru Suarez**, por su ayuda en los trámites quitando horas de estrés en mi persona.

**Victoria Araujo y Pedro Santa Rita** por su amistad apoyo y participación en el proyecto.

**Gerardo Rayo, Carlos Canto y Carlos Valencia** los cuales actualmente son el capital humano del acelerador **Van de Graaff 5.5.**

Gracias a la infraestructura que se tiene en el acelerador **Van de Graaff 5.5** este y muchos trabajos han podido llevarse a cabo y múltiples personas de licenciatura maestría y doctorado han podido graduarse.

El **taller del IFUNAM** hizo realidad el proyecto dando soporte, aportando ideas y construyendo parte del sistema, a continuación listo a los ingenieros involucrados:

- **Ing. Marco Antonio Veytia Vidaña**
- **Ing. Hesiquio Vargas Hernández**
- **Ing. Francisco Mercado Ramírez**

Y el personal del taller:

- **Carlos Sánchez Bribiesca**
- **Victor Monteagudo Galindo**
- **Victor Monteagudo Juárez**
- **Ricardo Flores Olvera**
- **Moises Zúrita Meza**
- **Ángel Zúrita Meza**

- José Ángel Flores Orozco
- Amando Vega Hernández
- David Chávez Belleza
- Gerardo Reza Villanueva
- Roberto Martínez Moreno

El apoyo de la **Dra. Catalina Stern** y de **Yadira Salazar** fue muy valioso, sus conocimientos sobre la materia (fluidos) y el acceso a sus instalaciones fue muy importante para el trabajo, gracias!

Por último me gustaría agradecer al **Dr. Efraín Chávez**, por haberme propuesto y apoyado a lo largo de este interesantísimo proyecto.

Este trabajo fue hecho gracias al apoyo de **CONACYT** 51600, 82692, 123655 y **DGAPAUNAM** IN-118310, IN-112609, IN-105510, IN-115213, TA-100213, IN-103312.

---



# Contents

<b>List of Figures</b>	<b>xi</b>
<b>List of Tables</b>	<b>xv</b>
<b>Glossary</b>	<b>xvii</b>
<b>1 Introduction</b>	<b>1</b>
1.1 Motivation . . . . .	2
1.2 Background . . . . .	4
<b>2 Aims of the project</b>	<b>7</b>
2.1 Final aim . . . . .	8
2.1.1 Alternative reactions . . . . .	11
2.2 Preliminary aims . . . . .	12
<b>3 Theoretical framework</b>	<b>15</b>
3.1 Nuclear physics . . . . .	16
3.2 Q-values . . . . .	18
3.3 Excitation levels . . . . .	19
3.3.1 Cross sections . . . . .	21
3.3.2 Astrophysics . . . . .	23
3.3.2.1 Nucleosynthesis . . . . .	23
3.4 Fluid Considerations . . . . .	27
3.4.1 Differential Pumping System . . . . .	36
3.4.2 Pumpdown theory . . . . .	41

## CONTENTS

---

<b>4</b>	<b>Experimental Methods</b>	<b>43</b>
4.1	Design . . . . .	44
4.1.1	Old Designs . . . . .	44
4.1.2	Final Designs . . . . .	46
4.2	The Built System . . . . .	52
4.2.1	Overview . . . . .	52
4.2.2	The Train . . . . .	55
4.2.3	Power Facility . . . . .	55
4.2.4	The concentric pipes . . . . .	56
4.2.5	Introducing The Roots System . . . . .	58
4.2.6	The Nozzle . . . . .	59
4.2.7	The Beamline Alignment And Inner Walls . . . . .	62
4.2.8	The Experimental array . . . . .	64
4.2.8.1	Scattering chamber . . . . .	64
4.2.8.2	Recent Updates . . . . .	65
4.2.8.3	EBS Setup . . . . .	66
4.2.8.4	Germanium Detector Setup . . . . .	67
4.2.8.5	E- $\Delta$ E Telescopic detector array . . . . .	68
4.3	Optical Tests . . . . .	69
<b>5</b>	<b>Tests, results and discussion</b>	<b>73</b>
5.1	Pump data . . . . .	74
5.2	Schlieren Tests . . . . .	79
5.2.1	Rectangular Nozzle Schlieren . . . . .	82
5.3	EBS tests . . . . .	83
5.3.1	EBS with air . . . . .	83
5.4	Tests with Nitrogen . . . . .	85
5.5	Tests with Argon . . . . .	88
5.5.1	Argon and nitrogen pressure tests . . . . .	90
5.5.2	Germanium Tests . . . . .	95
5.6	Experiments . . . . .	97
5.6.1	EBS of air, nitrogen and argon experiments . . . . .	98
5.6.2	Nuclear Physics Experiments . . . . .	101

<b>6</b>	<b>Conclusions and Future of the project</b>	<b>111</b>
6.1	Conclusion . . . . .	112
6.2	Future of the project . . . . .	113
<b>A</b>	<b>Software development</b>	<b>117</b>
A.1	Rebining . . . . .	118
A.2	columnScript . . . . .	121
A.3	matchColumns . . . . .	122
A.4	isonav . . . . .	124
<b>B</b>	<b>E-<math>\Delta</math>E detector array calibration</b>	<b>125</b>
<b>C</b>	<b>Published Articles</b>	<b>133</b>
	<b>References</b>	<b>137</b>

## CONTENTS

---

# List of Figures

1.1	Typical Experiment . . . . .	2
1.2	Jet representation . . . . .	3
2.1	D-D Reaction . . . . .	9
3.1	Minimum distance . . . . .	16
3.2	Energy Levels . . . . .	20
3.3	Gamow peak . . . . .	26
3.4	Area ratio . . . . .	29
3.5	Nozzle and catcher . . . . .	29
3.6	Nozzle dimensions . . . . .	32
3.7	Pumping array . . . . .	36
4.1	Old jet . . . . .	44
4.2	Square chamber . . . . .	45
4.3	Cylindrical chamber . . . . .	46
4.4	Old nozzle . . . . .	47
4.5	Beamline sketch . . . . .	48
4.6	Beamline front view . . . . .	50
4.7	Chamber holder . . . . .	52
4.8	Finished line . . . . .	53
4.9	Transitory Connection . . . . .	54
4.10	The Train . . . . .	55
4.11	Power Facility . . . . .	56
4.12	<b>The concentric pipes</b> - Seen from different perspectives. . . . .	57

## LIST OF FIGURES

---

4.13 <b>The catcher</b> - Shows the adjustable height jet catcher and the scattering chamber. . . . .	58
4.14 Roots Cart . . . . .	59
4.15 Nozzle Dimensions . . . . .	60
4.16 Nozzle System . . . . .	61
4.17 Inner Wall . . . . .	62
4.18 The Beam . . . . .	63
4.19 Bull's eye . . . . .	64
4.20 Inside The Scattering Chamber . . . . .	65
4.21 <b>Detector holders</b> - A newer more robust setup for the detectors. . . .	66
4.22 EBS Setup . . . . .	67
4.23 Germanium Detector . . . . .	68
4.24 Telescopic array . . . . .	69
4.25 The Schlieren Setup . . . . .	70
4.26 The Schlieren Physical Setup . . . . .	71
5.1 Turbo and mechanical data . . . . .	74
5.2 Diffusion pump data . . . . .	76
5.3 Roots pumping . . . . .	77
5.4 Supersonic flow . . . . .	79
5.5 Tongue Height . . . . .	81
5.6 Nitrogen and Oxygen . . . . .	83
5.7 Protons in Nitrogen . . . . .	86
5.8 2.8 MeV protons in Nitrogen . . . . .	87
5.9 Low energy protons . . . . .	88
5.10 Argon Pressures . . . . .	89
5.11 3D Argon . . . . .	90
5.12 Argon various angles . . . . .	91
5.13 Argon various angles 60V . . . . .	91
5.14 40V vs 60V . . . . .	92
5.15 Background detectors . . . . .	92
5.16 Argon again . . . . .	93
5.17 Nitrogen data . . . . .	94

---

**LIST OF FIGURES**

5.18 Argon Germanium Data . . . . .	95
5.19 Argon Germanium Data Zoomed . . . . .	96
5.20 Argon Germanium Data $^{40}\text{Tl}$ Zoom . . . . .	97
5.21 Air multiplot . . . . .	98
5.22 Argon peak . . . . .	99
5.23 Oxygen detector . . . . .	100
5.24 SIMNRA air fit . . . . .	101
5.25 2D $\Delta E$ vs $E_{tot}$ histogram . . . . .	102
5.26 2D histograms . . . . .	103
5.27 2D histograms 2 . . . . .	104
5.28 histogram projection 1 . . . . .	105
5.29 histogram projection 2 . . . . .	105
5.30 Alpha cross section . . . . .	107
5.31 Oxygen levels . . . . .	108
A.1 QR . . . . .	124
B.1 Alpha Peak Calibration . . . . .	126
B.2 Energy to channel relationship . . . . .	127
B.3 2D histogram for calibration . . . . .	127
B.4 E projection . . . . .	128
B.5 $\Delta E$ projection . . . . .	128
B.6 $\Delta E$ calibration . . . . .	129
B.7 $E_{tot}$ vs $\Delta E$ . . . . .	130
B.8 $E_{tot}$ projection . . . . .	130
C.1 Phys. Rev. ST . . . . .	134
C.2 X LASNPA . . . . .	134
C.3 Cocoyoc 1 . . . . .	135
C.4 Cocoyoc 2 . . . . .	135

## LIST OF FIGURES

---



# List of Tables

2.1	Comparison between a solid CD <sub>2</sub> (deuterated polyethylene) target and a supersonic gas jet target of pure deuterium with a beam current of 100 nano Amperes. . . . .	11
2.2	(d,n) reactions on gas targets with positive Q-value. . . . .	11
2.3	There are only seven channels open for beam energies below 5 MeV. . .	14
3.1	Proton minimum energy for nuclear reaction with various elements. . . .	17
3.2	Q-values for different reactions, the proton's mass is; $m_p = 1.00782503223u$ . 19	
3.3	Gamow energies for various fusion reactions. . . . .	24
3.4	$E_M$ values for various reactions, $kT \approx 0.2\text{MeV}$ . . . . .	27
3.5	Knudsen's number . . . . .	38
5.1	Estimated vs calculated pressures. In the different chambers. . . . .	78
5.2	Channel and height (count number) of the various peaks. . . . .	84
5.3	Channel, height, peak channel and adjusted peak counts. . . . .	89
5.4	Background comparison. . . . .	93
5.5	Comparison of the old vs new and reported percentages in Air. . . . .	100
5.6	Center of mass energies and the corresponding alpha energies for the different <sup>12</sup> C excitation levels for all deuteron beam energies ran in this experiment. The values in bold correspond to Figure 5.25. <b>Note:</b> All energies are in MeV. . . . .	106
6.1	Problem Solution . . . . .	114
B.1	Alpha energy and energy loss in the telescopic detector array. . . . .	126

## LIST OF TABLES

---

B.2 Telescope detector array conditions. The threshold for the $\Delta E$ detector was set at -92mV. . . . .	126
--	-----

# Glossary

$^2\text{H}$  is an isotope of hydrogen, its nucleus contains one proton and one neutron. [10](#), [116](#)

$^3\text{He}$  an isotope of helium, it contains 2 protons and one neutron. It can be used as a tag for a neutron in the associated particle technique. [8–10](#)

**aluminum profile** light and modular profiles that allow for fast construction of important hardware such as tables. [51](#)

$^{40}\text{Ar}$  the most common isotope of Argon. [13](#)

**associated particle technique** in the reaction  $^2\text{H} + ^2\text{H} \rightarrow ^3\text{He} + \text{n}$  at a specific energy given by the beam, and a specific angle for the  $^3\text{He}$  measurement there is a kinematical relationship with a neutron which is called the associated particle. [8](#), [10](#)

**AWK** an interpreted programming language typically used for data extraction. Its name is formed from the initials of their creators; *Alfred Aho, Peter Weinberger and Brian Kernigham*. [118](#), [119](#), [121](#), [123](#)

**bar** Unit of pressure, it is roughly equivalent to an atmosphere and approximately 750 Torr. [12](#), [85](#), [87–89](#)

**Bash** The Bourne again shell. [118](#), [119](#), [121](#), [123](#)

**beam** a stream of energized particles produced by a particle accelerator. [2](#), [12](#), [83](#), [88](#), [89](#), [94](#)

**beam profile monitor** sends electrical signals to an oscilloscope that define the  $x$  and  $y$  components of the beam. [55](#)

**beam selector magnet** allows to bend the accelerator's beam to a respective beamline. [55](#), [112](#)

**beamline** a vacuum system that is connected to an accelerator so the beam can go through it and perform a specific experiment. [44](#), [46](#), [47](#), [50–53](#), [55](#), [63](#), [64](#), [68](#), [79](#), [112](#)

**chamber holder** Holds the vacuum chambers. [51](#), [52](#), [55](#), [63](#), [64](#)

## Glossary

---

**channel** natural scale for a detector, the channel number can be related to the energy via a linear relationship. 84–86, 88, 89, 121

**clamp** a piece that is tightened in order to seal shut a vacuum system. 54, 57, 68

**CNO** Carbon Nitrogen Oxygen cycle. 5

**concentric pipes** are part of the central pumping stages, one goes to a high speed mechanical pump and the other to the roots system. 46, 53, 54, 56–58, 78, 116

**differential pumping system** a series of pumping stages where gas flow is allowed in between them and the pressure at each stage can be considerably lowered. 41, 47, 49, 54–56, 62, 63, 78, 112, 114–116

**diffusion pump** a vacuum pump that can achieve high vacuum, it works by heating oil generating a jet that drags molecules to its walls where the oil gets condensed. It has to be backed by a mechanical pump. 40, 41, 49, 50, 53, 56, 63, 78, 114, 115

**EBS** Elastic backscattering spectrometry, a technique used for determining the composition of a material

using backscattered ions, the scattering can be non-Rutherford. 13, 83, 85–87, 98, 112, 114

**Faraday cup** Monitors the beam and integrates the charge. 52, 55, 94

**germanium detector** high purity germanium crystal that is used as a detector to measure the energy from gamma rays. 13, 49, 64, 66–68, 95, 112, 116

**gnuplot** a command line plotting program. 118

**ISO** International Organization for Standardization. 47

**Knudsen's number** is a parameter that uses the mean free path ( $\lambda$ ) and a characteristic length, to classify the flow regime. 37, 38, 40

$\lambda$  the mean free path. xviii, 37, 40

**laser** Light Amplification by Stimulated Emission of Radiation, a device that emit highly amplified and coherent radiation. It is used to visualize the jet. 70, 82

**LF250** a 10 inch in diameter ISO flange, the LF standard is referred as the large flange. 82, 95

- LUNA** Laboratory Underground for Nuclear Astrophysics. 5
- Mach** or Mach speed represents the speed of the flow, with respect to the local speed of sound. 28, 30, 31, 34, 79–82
- mass flow rate** The net movement of matter from one location to another. 30
- mechanical pump** can pump gas from atmospheric pressure to around,  $10^{-3}$ Torr. 35
- neutron** an electrically neutral subatomic particle in the baryon family. 8–10, 116
- $^{14}\text{N}$  the most common isotope of nitrogen. 13
- nozzle** a projecting part with an opening where the gas flows through. 28–32, 34–36, 45, 46, 52, 59–61, 65, 67, 69, 70, 79–83, 86, 115, 116
- nucleosynthesis** The process by which heavier chemical elements are synthesized from hydrogen nuclei in the interiors of stars. 5
- Oxygen** A nonmetallic element constituting approximately 21 percent of the atmosphere. 13, 83–86, 98, 100
- proton** A stable, positively charged subatomic particle in the baryon family. 5, 83, 87, 88, 95
- psi** Or pounds per square inch. Is a unit of pressure that is approximately 51 Torr. 12
- pumping speed** represents the effective pump’s volume displacement speed at a given pressure. The unit used is liters per second. 28, 30, 34, 35, 40, 44, 53
- QF40** a 1.5 inch in diameter ISO flange, the QF standard is also commonly known as NW and KF, and referred as quick flange and klein flange. 74, 116
- quadrupole magnet** consists of 4 electromagnets surrounding the beamline, allowing to focus the beam. 55
- ROOT** A modular scientific software framework. It provides all the functionalities needed to deal with big data processing, statistical analysis, visualisation and storage. It is mainly written in C++ but integrated with other languages such as Python and R.. 118, 129, 131

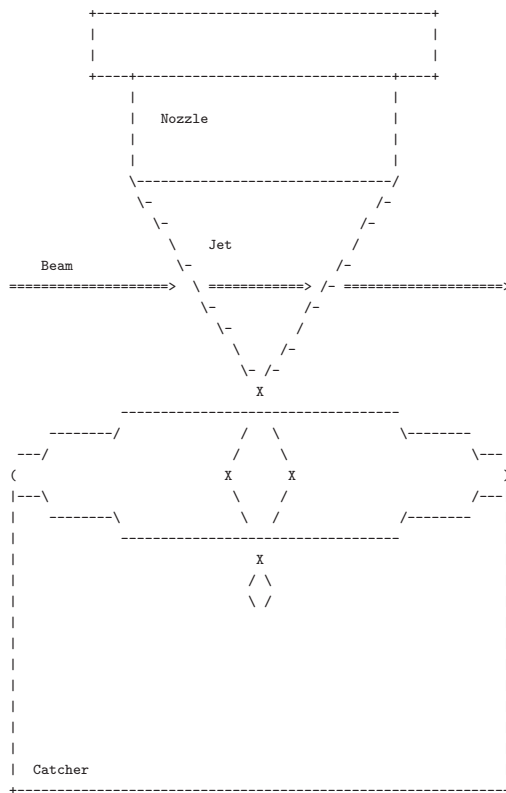
## Glossary

---

- roots system** consist of 3 devices a large and a medium roots pump and a mechanical backing pump. It has a high pumping speed in the intermediate flow region. 35, 36, 77, 78, 115, 116
- scattering chamber** a vacuum chamber where the beam hits the target and scatters. 45, 49, 54, 59, 62–65, 67, 70, 78, 82, 86, 87, 95, 112, 115, 116
- Schlieren** a technique used to visualize transparent media. 45, 69, 70, 79, 82, 113
- shock** a region of the flow where thermodynamic properties change dramatically. 28, 32, 34, 61, 70, 79–82
- solid state detector** A detector for detecting charged particles. 9, 65, 83, 89, 90
- supersonic gas jet target** a windowless high density and well defined target for nuclear experiments. 4, 5, 8, 10, 12, 13, 28
- the train** consists of a colimator, a beam profile monitor, and a Faraday cup. 55, 62
- throughput** defines the amount of gas flowing through an aperture, it is represented by  $Q$ . 30, 34, 37–41, 60, 62
- torr** Unit of pressure, 1 atm = 760 Torr. 12, 30, 34, 35, 37, 39
- tsv** tab separated value. 122
- tunnel effect** a quantum-mechanical process by which a particle can pass through a potential energy barrier that is higher than the energy of the particle. 5
- turbo pump** a high vacuum pump that resembles a turbine, it has to be backed by a mechanical pump. 41, 49, 52, 56, 63, 75, 76, 78, 115
- view port** a glass that allows to see inside the vacuum chamber. 51, 62, 63, 70, 74, 82

1

# Introduction



“Rule number 1: Cardio”

– *Columbus*

Zombieland

## 1. INTRODUCTION

---

### 1.1 Motivation

A typical nuclear physics experiment involves a **beam** of particles (for example protons, deuterons or alphas) impinging on a target. Figure 1.1 shows schematically such a setting; some of the particles of the **beam** will be scattered by the target in different directions. There could also be outgoing particles that were not present in the **beam** nor the target. These particles are the product of nuclear reactions.

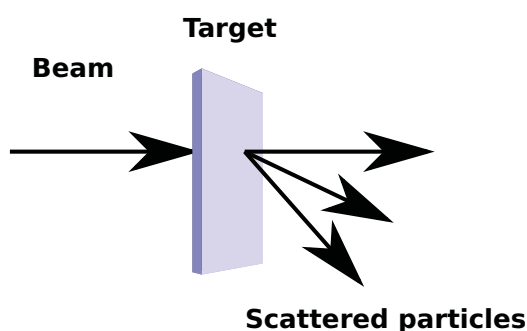


**Figure 1.1: Typical Experiment** - Beam from the accelerator hitting a target.

A fact to keep in mind while planning a study of any nuclear reaction is that the number of outgoing particles of interest in any given direction, is typically 3 orders of magnitude smaller than the elastically scattered ones. Counting statistics is an important issue.

If the beam intensity is increased (or the target density) the amount of time required to achieve the necessary statistics in an experiment is smaller. However, incrementing the beam intensity comes at a price. The target is typically a thin solid<sup>1</sup> and it is placed inside a vacuum chamber. Vacuum is important so that the beam interacts marginally with the chamber's atmosphere. However, the beam deposits thermal energy on the target which dissipates relatively slow because convection<sup>2</sup> is considerably decreased in vacuum. The target could get overheated, modified and eventually destroyed before the data acquisition is completed.

Some of the potential targets of interest for nuclear studies are found in nature as gases (H, N, O, Noble Gases and others). In some cases, a solid target containing such

---

<sup>1</sup>A sheet thin enough to let the scattered particles out.

<sup>2</sup>Convection is heat transfer due to actual movement of warmed matter.



elements (a chemical compound) can be produced<sup>1</sup>, and the target can be placed inside the scattering chamber. However, withstanding high beam currents without modifying the target as mentioned above remains an issue. Not to mention that there could be unwanted reactions with the other elements introduced in the compound.

For the case of noble gases such as Neon or Argon, making a solid compound is out of the question. Typically, a thin walled gas cell is used for those cases. The idea is that most of the beam will be able to penetrate the walls react with the gas and then detect the outgoing particles outside the cell. However similar problems arise: the beam does interact with the cell walls, the scattered particles have to get out of the cell and reach the detectors and the thin walls could also be destroyed by an intense beam.

Not to mention that the deposited heat induces pressure gradients inside the gas cell, modifying the properties of the target. A high density well defined region of the single element of choice which is not affected by the interaction with a high intensity beam constitutes the ideal target. A supersonic gas jet is the best approximation to such an ideal target.

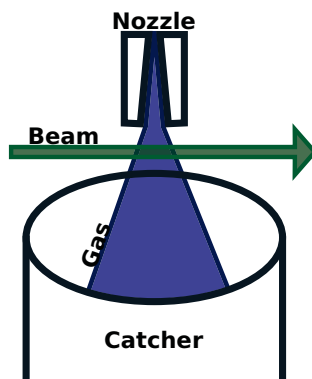


**Figure 1.2: Jet representation** - An artistic representation of the jet is shown as a well defined windowless column of gas.

It is true that the achievable densities are smaller than those a solid provides, but such a decrease in the target density can be largely compensated by the increase in the beam intensity in terms of counting statistics. Depending now only on the accelerators limitations we can have orders of magnitude higher counting statistics. An artistic

---

<sup>1</sup>Such as polyethylene (C<sub>2</sub>H<sub>4</sub>)<sub>n</sub>

## 1. INTRODUCTION

---

representation of the target is given in figure 1.2. It is, in essence, a well-defined high density column of gas surrounded by a very low pressure (high vacuum) region.

### 1.2 Background

The condition seems rather extreme. It is a gas without constrictions inside a vacuum chamber. Gases tend to occupy all the volume of their enclosure as soon as they are released. However, this condition has been achieved several times in the past (1, 2). Becker (3) is another important antecedent, he worked with various gas types which include  $^2\text{H}$ ,  $^3\text{He}$ , Nitrogen, Oxygen, Neon and Argon. Modern work can be seen in JENSA (4) and HIPPO (5) where Helium is the main topic.

Systems like this have various applications within nuclear experiments. Either as a target (as in the present work) or even as a stripper (not necessarily supersonic flow) as in the case of FRIB (6) using a Helium jet.

Such types of experiments require intense beams since they are performed under the Coulomb barrier where cross sections are small and decreasing exponentially as the bombarding energy is reduced.

Non-supersonic jets have also been used as targets as in the case of (7, 8, 9), they provide most of the properties of the [supersonic gas jet target](#) such as the ability to withstand high current from the accelerator. However, they lack of the well-defined high density region that allows us to better resemble an ideal solid target, an indestructible one.

There are in fact studies in the resemblance of laboratory jets and astrophysical jets (10) and good numerical results that support the fact. However, we are more interested in nuclear reactions given astrophysical conditions.

This work will not concentrate in calculating specific, interesting, details of supersonic jet flow. It is important to eventually have a more complete background of the fluid dynamics, such as in (11, 12), applied to the conditions our system is subjected<sup>1</sup>.

An example of nuclear cross section measurements made on a solid target that is relevant to this work, performed by our group, is  $^{12}\text{C} + ^{12}\text{C}$ . This and other work can be seen in (13, 14, 15, 16, 17). Carbon is a nice target to use in the laboratory, it stands large temperatures, is not toxic and largely available. The chosen reaction for

---

<sup>1</sup>Low atmospheric pressures.

this thesis involves carbon and the results are shown in section 5.6.2. Efforts have been made in using Nitrogen as a gas target such as the LUNA accelerator (18, 19) in Gran Sasso Italy<sup>1</sup> such efforts give estimations of the age of the stars since the proton capture reaction in Nitrogen forms part of the important CNO burning cycle in the stars.

The LUNA facility, being a mile underground, is optimal for all sorts of astrophysical experiments (21). A  $10^6$  background suppression factor in cosmic ray flux is achieved by the rock shield and an extra  $10^3$  neutron flux reduction comes from the special geology of the site.

Astrophysical experiments are of such great importance that entire facilities such as the aforementioned LUNA accelerator and the CLAIRE (22) facility<sup>2</sup> are dedicated entirely to this subject. The CLAIRE project claims to produce currents of up to  $100mA$  and to have a supersonic gas jet target.

The main objective with these astrophysical experiments is to understand the stellar evolution and how the nucleosynthesis is made. Clayton (23), Reeves (24) and Steigman (25) give a good introduction to the subject.

Stellar nucleosynthesis tends to be “slow” since since the nuclear reactions driving it occur at energies below the Coulomb barrier by means of the tunnel effect. The reaction rate is measured and from this the age of the stars is estimated from their initial state to their “current observed”<sup>3</sup> state. From an experimental point of view Angulo (26) and Hoffman (27) are modern references.

In general gas target systems are also important for higher energy physics studies, such as in the Stringfellow paper (28) or the PANDA experiment (29).

---

<sup>1</sup>See the official site (20) for more information. NOTE: The link may be broken.

<sup>2</sup>Currently under development.

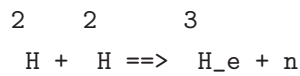
<sup>3</sup>Light from the sun takes about 8 minutes to reach the earth, whatever happens on our closest star we can't know about until *8 minutes* later.

## 1. INTRODUCTION

---

## 2

# Aims of the project



```
-----
-/ppppppp\ -   -/ppppppp\ -   -/ppppppp\ -
/ppppppppppp\ /ppppppppppp\ /ppppppppppp\
|ppppppppppp| |ppppppppppp| |ppppppppppp|
\ppppppppppp/ \ppppppppppp/ \ppppppppppp/
-\ppppppp/- | -\ppppppp/- +--\ -\ppppppp/- /nnnnnnnnnn\ | /nnnnnnnnnn\
----- -+--- ----- | |= ----- |nnnnnnnnnn|---+---|nnnnnnnnnn|
-/nnnnnnnn\ - | -/nnnnnnnn\ - +--/ -/ppppppp\ - \nnnnnnnnnn/ | \nnnnnnnnnn/
/nnnnnnnnnn\ /nnnnnnnnnn\ /ppppppppppp\ -\nnnnnnn/- -\nnnnnnn/-
|nnnnnnnnnn| |nnnnnnnnnn| |ppppppppppp| -----
\nnnnnnnnnnn/ \nnnnnnnnnn/ \ppppppppppp/
-\nnnnnnnn/- -\nnnnnnnn/- -\ppppppp/-
-----
```

“The earth is blue, how wonderful. It is amazing.”

– *Yuri Gagarin*

World’s first cosmonaut

## 2. AIMS OF THE PROJECT

---

This is a very ambitious project. This chapter concentrates in contextualizing the thesis within the entire project.

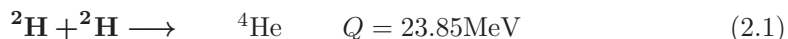
### 2.1 Final aim

One of the principal motivations for the project is [neutron](#) production. Past work on measurement of cross section has been done before at multiple angles and at energies between 1keV-200MeV (30).

However, there is a significant lack of data for small angle scattering, between 0 and 10 degrees, because of the intrinsic difficulty of separating the incident neutron flux from the scattered outgoing one. Despite the systematic obstacles some work has been done in this angular region (31, 32).

[Neutrons](#) are a fantastic probe, having zero net charge <sup>1</sup>, they interact almost exclusively via strong nuclear interaction<sup>2</sup>.

There are many ways to produce neutrons in an accelerator laboratory using nuclear reactions. For example; we can produce them using deuterium beams. Deuterons have a single a proton and a single neutron in their nucleus. If we can produce a deuteron target, we can induce a number of nuclear reactions listed in equations 2.1-2.4. The reaction we are interested is marked in bold 2.3:



That is using Deuterium as the beam as well as the target (with a [supersonic gas jet target](#)), we obtain a [<sup>3</sup>He](#) nucleus and a [neutron](#), see figure 2.1.

The [<sup>3</sup>He](#) nucleus is a charged particle and the detection efficiency is practically 100%. this leads to the “[asociated particle technique](#)”. Here through the detection and

---

<sup>1</sup>There is still work being done regarding the charge distribution of the neutron see for example (33).

<sup>2</sup>They have magnetic moment and are affected by gravity (see (34)), most of the time this interactions are vanishingly small with respect the strong nuclear interaction. Not to mention that they also decay via the weak interaction.

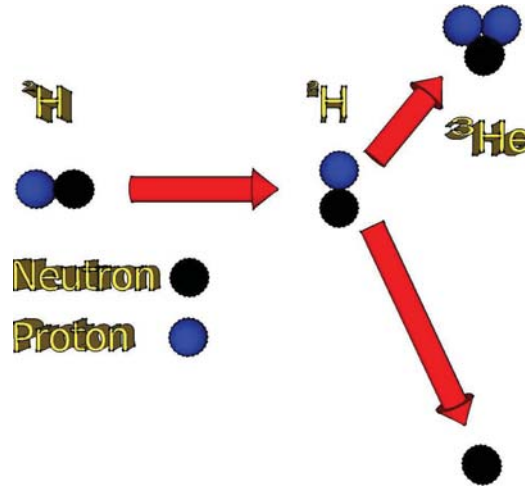


**Figure 2.1: D-D Reaction** - A sketch of the reaction  ${}^2\text{H} + {}^2\text{H} \rightarrow {}^3\text{He} + \text{n}$

identification of the  ${}^3\text{He}$  we know that a kinematically associated neutron is moving in a specific direction with a well-defined energy. That is, given a specific angle of detection for the  ${}^3\text{He}$  at a given beam energy produces a neutron flux in a specific direction with a well-defined energy.

Even if we don't detect the neutron we can have a good knowledge of how many neutrons there are because the solid state detector for  ${}^3\text{He}$  sees basically all the them, and there is a one to one correspondence between them and the neutrons<sup>1</sup>.

It is also important to notice that all neutrons produced in this way are tagged by the detection of its associated particle within a temporal window.

The neutron detection efficiency of any detector can be measured using this technique. The  ${}^3\text{He}$  nucleus and the neutron detectors are placed at angles that satisfy kinematics. Then, given an event in the solid state detector we expect to have an event in the neutron detector. The detection efficiency becomes the simple ratio between the number of neutrons to  ${}^3\text{He}$  detected.

In this procedure the definition and construction of the time window (gate) for the coincidence condition is important:

- We know the distances between the detectors.

<sup>1</sup>The detectors also measure background due to cosmic rays, unaccounted radiation sources, etc. Special care must be taken in removing the background, however most of it can be removed via energy discrimination.

## 2. AIMS OF THE PROJECT

---

- We know the energies of both  $^3\text{He}$  and the **neutron** (because of kinematics).

Therefore we know the traveled length in a specified amount of time<sup>1</sup>. This gate rids us from most of the background in the **neutron** detector.

A very important aspect of the reaction is that it has a small set of outcomes and only one in which  $^3\text{He}$  is involved. This is a very clean way of producing fast mono-energetic **neutron** fluxes.

This procedure is called the **associated particle technique**, where the associated particle is the **neutron**. This technique, combined with a **supersonic gas jet target**, can be used as an intense source of mono-energetic **neutrons**. Due to the fact that the jet can take a lot more beam than a solid target<sup>2</sup>.

A source like this is a valuable asset. To mention just a few applications:

- Small angle scattering with **neutrons** in lead could be measured (31, 32) and also (35).
- **Neutron imaging**: A big solid angle detector with good position resolution, neutrons could be used in the same manner as X-rays for imaging. However **neutrons** probe much deeper into matter, seeing through lead poses no problem<sup>3</sup>.

There are antecedents to a system like this, not specifically for neutron production but for handling a jet with hydrogen. Back in 1995 *Doskow* (36) talked about a hydrogen jet, so there is an important antecedent that this can be done. In fact since we are concerned with deuterium, the molecules are about twice as heavy.

A comparison of a solid target with the supersonic jet is shown in table 2.1. It compares a pure deuterium supersonic jet with the typical solid equivalent  $CD_2$ , or deuterated polyethylene.

It shows that even though the density of the  $^2\text{H}$  gas target has less particles per square centimeter, the important value that actually increases the reaction rate (Beam  $\times$  Areal density) is larger in the gas case. It is also worth noting, that the spurious reaction with the carbon targets in the polyethylene is not present in the jet target.

---

<sup>1</sup>Within an error of 100ns

<sup>2</sup>Deuterium at standard conditions is a gas, in order to solidify it we combine it with carbon, making the compound *deuterated polyethylene*.

<sup>3</sup>Example from DARPA: <http://www.darpa.mil/news-events/2014-09-24>. NOTE: The link may be broken.



## 2.1 Final aim

solid	$CD_2$		gas	Deuterium	
thickness	$1.00 \times 10^{-3}$	cm	pressure	100	torr
Areal density (CD2)	$3.88 \times 10^{19}$	p/cm <sup>2</sup>			
Carbon Tgts	$7.61 \times 10^{18}$	p/cm <sup>2</sup>			
Deuterium Tgts	$1.52 \times 10^{19}$	p/cm <sup>2</sup>	Deuterium Tgts	$3.3 \times 10^{18}$	18
Max Beam	$6.25 \times 10^{11}$	p/s	Max Beam	$6.25 \times 10^{14}$	p/s
Beam $\times$ Areal density	$9.51 \times 10^{30}$		Beam $\times$ Areal density	$2.05 \times 10^{33}$	
			Gain Factor	$2.2 \times 10^2$	

**Table 2.1:** Comparison between a solid CD<sub>2</sub> (deuterated polyethylene) target and a supersonic gas jet target of pure deuterium with a beam current of 100 nano Amperes.

### 2.1.1 Alternative reactions

Table 2.2 lists (d,n) reactions with different potential gas targets with positive Q-values. The row in bold corresponds to the aforementioned d(d,n)<sup>3</sup>He reaction.

Target	Residue	Q[MeV]	Coulomb E[MeV]
<b><sup>2</sup>H</b>	<b><sup>3</sup>He</b>	<b>3.27</b>	<b>0.48</b>
<sup>3</sup> H	<sup>4</sup> He	17.59	0.44
<sup>14</sup> N	<sup>15</sup> O	5.07	2.29
<sup>20</sup> Ne	<sup>21</sup> Na	0.21	3.02
<sup>21</sup> Ne	<sup>22</sup> Na	4.51	2.99
<sup>22</sup> Ne	<sup>23</sup> Na	6.57	2.95
<sup>40</sup> Ar	<sup>41</sup> K	5.58	4.62
<sup>80</sup> Kr	<sup>81</sup> Rb	2.63	7.76

**Table 2.2:** (d,n) reactions on gas targets with positive Q-value.

In the Table, <sup>2</sup>H and <sup>21,22</sup>Ne are rare and expensive substances. <sup>3</sup>H is also radioactive so in spite of having the lowest Coulomb barrier and the highest Q-value it is not necessarily the best choice to routinely produce fast neutron beams. The large Coulomb barrier on heavy noble gases make them difficult to use in a low energy facility like ours. <sup>14</sup>N(d,n)<sup>15</sup>O stands as an appealing option to produce fast neutrons in comparison with the traditional d(d,n)<sup>3</sup>He reaction using a solid CD<sub>2</sub> (deuterated polyethylene) target. Atmospheric <sup>14</sup>N is readily available at no cost, and has a larger

## 2. AIMS OF THE PROJECT

---

Q-value.

### 2.2 Preliminary aims

There will be several preliminary scientific objectives to be accomplished on the way.

1. Produce a [supersonic gas jet target](#), inside a vacuum chamber, not just theoretically but experimentally.
2. Characterize the target using the accelerator's beam.
3. Perform a nuclear physics experiment with the system and produce reliable data.

The **first aim** is a very radical condition, chapter 3 concentrates in the calculations designs and construction of such a system particularly sections 3.4, 3.4.1 and 3.4.2. Since we are handling fluids the specific behavior tends to differ from the theoretical prediction, the pumping speeds of most of the available pumps were estimated (in response of the lack of documentation), some of the pumps had been there for decades<sup>1</sup>, and such values were the ones used for the calculations and the design.

Order of magnitude estimates are good enough for our design purposes. Also the units used will be in accordance with the gauges and pumps we use in the laboratory, that is the pressure is measured in [Torr](#) (sometimes [psi](#) or [bar](#)) and the pumping speed in liters per second. However, as it was proven in the experiments in section 5.1 the calculations (given in chapter 3) were in accordance to the experiment.

Most of chapter 4 is dedicated to the setup this required. It also shows the built system in section 4.2, were it presents additional equipment necessary for the target system such as the train 4.2.2 and the power facility 4.2.3.

The time consuming process of alignment is outlined in section 4.2.7. This was a difficult task since the pumping system demanded plenty of vacuum chambers and small apertures connecting them, through which the beam had to go through in order to reach the jet. We developed a technique that used the [beam](#) itself to fine-tune the alignment.

---

<sup>1</sup>Restorations of old mechanical pumps and diffusion pumps were in order. But potential leaks due to deterioration were a concern.

Pressure data from pump-downs in the system and stationary states were obtained and are presented in chapter 5.

A Schlieren setup was made in order to visualize the shock patterns that are present in the jet, section 4.3 shows the optical setup in order to perform the test. The results are shown in section 5.2.

Once the first aim was attained, we proceed to tackle the **second one** results are shown in chapter 5. Data of the first performed experiments is given in section 5.3, with air, Nitrogen ( $^{14}\text{N}$ ) and Argon ( $^{40}\text{Ar}$ ) as targets. Using an air **supersonic gas jet target**, we were able to locate mainly its 2 most abundant elements in the first set of experiments (Nitrogen and **Oxygen**) shown in section 5.3. The corresponding experimental setup is shown in section 4.2.8.3. In improved versions of the **EBS** setup (using what is shown in 4.2.8.2) Argon started to show, the data is presented in section 5.6.1.

Energy, pressure and counting statistics curves with Nitrogen and Argon were made and shown in section 5.5.1. Those were the chosen gases mainly because:

- They are cheap.
- They are relatively safe.
- In the case of Nitrogen and Argon, they are almost isotopically pure. Almost all Nitrogen is  $^{14}\text{N}$  and almost all of Argon is  $^{40}\text{Ar}$ .

Finally the **third aim** nuclear physics was also done in the laboratory. Chapter 3 dedicates the first sections (3.1, 3.2, 3.3, 3.3.1, 3.3.2 and 3.3.2.1) in establishing some basic concepts.

A system like this is particularly interesting for nuclear astrophysics. Basic theory is shown in section 3.3, 3.3.2, and 3.3.2.1. The experimental setup to study  $^{40}\text{Ar}(p, \gamma)^{41}\text{K}$  is shown in section 4.2.8.4, where we used a **germanium detector** for this purpose. The data is presented in chapter 5 in section 5.5.2. The results from the measurements were inconclusive for several reasons:

- The beam energy was too low (we ran in parasite of a the  $^{12}\text{C}(p, \gamma)$  experiment on a different beam line).
- Then the proton beam was not available anymore.

## 2. AIMS OF THE PROJECT

---

- And the Germanium detector went off line for repair.

However there were good indicators in the data that we might be able to observe the desired nuclear reaction.

Apart from astrophysics, standard nuclear physics can also be subject of study. We got interested in particular with the  $^{14}\text{N} + d$  reaction, which has several exit channels with relatively high Q values, table 2.3. The Coulomb barrier is around 2.3 MeV to form the  $^{16}\text{O}$  compound nucleus. Since the Q-value (see sections 3.1 and 3.2) for fusion is very large (20.74 MeV) we are able to study a high excitation region in  $^{16}\text{O}$ .

Ejectile	Residual	Q[MeV]
$\gamma$	$^{16}\text{O}$	20.74
$\alpha$	$^{12}\text{C}$	13.57
$p$	$^{15}\text{N}$	8.61
$4\alpha$	—	6.29
$n$	$^{15}\text{O}$	5.07
$d$	$^{14}\text{N}$	0
$^3\text{He}$	$^{13}\text{C}$	-2.06
$^3\text{H}$	$^{13}\text{N}$	-4.30

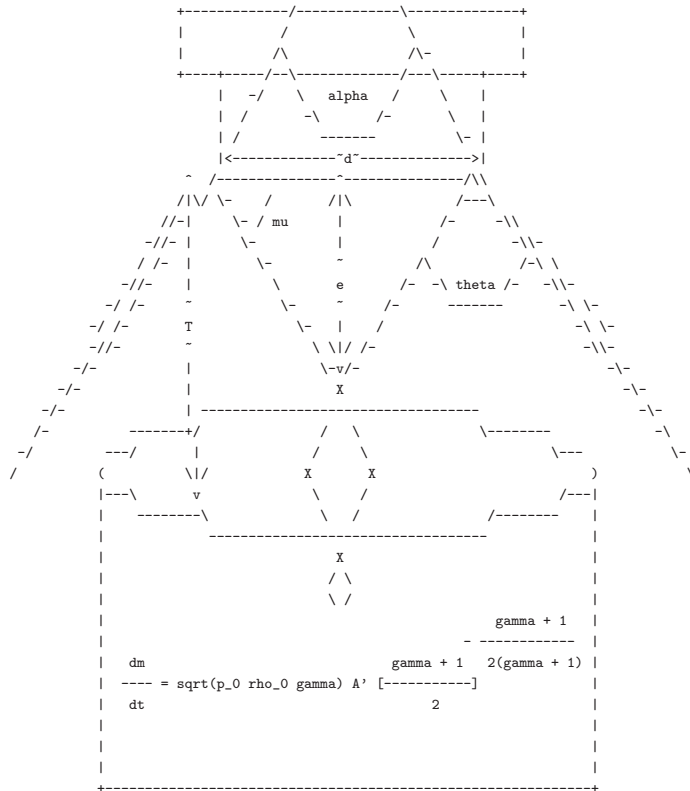
**Table 2.3:** There are only seven channels open for beam energies below 5 MeV.

In this work we concentrate on the  $^{14}\text{N}(d, \alpha)^{12}\text{C}$  channel where alpha particles are detected at a fixed angle in the laboratory (section 4.2.8.5 depicts the array), while the bombarding energy is changed between 2.2 and 3.36 MeV. So our study spans an energy interval right at and above the top of the barrier. The results are presented in chapter 5 in section 3.1 where we were able to measure an absolute nuclear differential cross section, given the data and with the help of the theoretical development shown in section 3.3.1.

The published articles, that were a direct product from this work, are shown as links and QR codes in appendix C.

# 3

## Theoretical framework



“Today me will live in the moment  
unless it’s unpleasant  
in which case  
me will eat a cookie.”  
– *Cookie Monster*  
Muppet on Sesame Street.

### 3. THEORETICAL FRAMEWORK

---

This chapter reviews some basic nuclear theory and fluid theory for the project. The fluid theory was used extensively for the design presented in chapter 4.

#### 3.1 Nuclear physics

One can imagine a nuclear reaction taking place once the repulsive Coulomb force between the positive charged target and projectile has been overcome and both nuclei are “touching” each other as in figure 3.1.

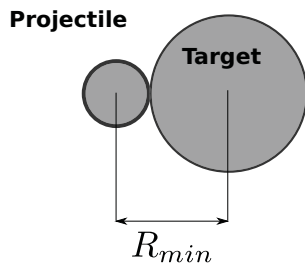


**Figure 3.1: Minimum distance** - A minimum, *classical*, distance (for a head on collision) has to be attained between the projectile and the target in order to have a nuclear reaction.

The minimum energy ( $E_{min}$ ) is:

$$E_{min} = \frac{Z_p Z_t e^2}{4\pi\epsilon_0 R_{min}} \quad (3.1)$$

Where the variables  $Z_p$ ,  $Z_t$ ,  $e$ , and  $\epsilon_0$  are respectively; the projectile’s and target’s atomic number, the electron’s charge and the vacuum’s permittivity.

This relationship can be simplified if we use  $\alpha$  (the fine structure constant), and the  $\hbar c$  relationship:

$$\alpha = \frac{e^2}{4\pi\epsilon_0 \hbar c} \approx \frac{1}{137} \quad (3.2a)$$

$$\hbar c \approx 197 \text{MeV} \text{fm} \quad (3.2b)$$

Substituting 3.2a into equation 3.1 we get:

$$E_{min} = \frac{Z_p Z_t \alpha \hbar c}{R_{min}} \quad (3.3)$$

We can estimate the radius of each nucleus ( $R$ ) using:

$$R = r_0 A^{1/3} \quad (3.4)$$

Where  $r_0 \approx 1.25 fm$  and  $A$  is the nucleon number. Assuming the projectile is a proton,  $Z_p = 1$  and  $A = 1$ , and using equation 3.2b we get:

$$E_{min} \approx \frac{1.2 Z_t}{1 + A^{1/3}} \text{MeV} \quad (3.5)$$

The facility has a 5.5 MV Van de Graaff electrostatic accelerator which can deliver beams of energy up to 5.5 MeV for single charged positive charged particles (protons, deuterons, Helium isotopes and so on). Table 3.1 shows the minimum energy (as defined above, equation 3.5) for a proton beam on a variety of targets. Comparing with the maximum energy the accelerator can provide to a proton with the table values, we conclude that the facility is well suited to study nuclear reactions on light elements.

Element	$Z_t$	$A$	$E_{min}$ (MeV)
He	2	4	0.92
N	7	14	2.45
O	8	16	2.7
Ne	10	20	3.23
Ar	18	40	4.88

**Table 3.1:** Proton minimum energy for nuclear reaction with various elements.

In particular, the type of nuclear reaction we are interested in is fusion reactions. Such as :



### 3. THEORETICAL FRAMEWORK

---

Such capture reactions occur at some point along the evolution of a star and in the stellar nucleosynthesis processes. They are the core of nuclear astrophysics. As mentioned above, these reactions can be studied in our facility. Emulating experimentally a star in the lab is quite a project!

As it has already been mentioned, these reactions can be obtained in the facility. Simulating experimentally a star astrophysical reactions in the lab, it becomes a difficult problem to tackle<sup>1</sup>. Section 3.3.2 discusses more on this type of reactions.

#### 3.2 Q-values

The Q-value is basically<sup>2</sup>:

$$Q = (m_{initial} - m_{final})c^2 = T_{final} - T_{initial} \quad (3.7)$$

Where  $m_{initial}$ ,  $T_{initial}$ ,  $m_{final}$  and  $T_{final}$  are respectively the initial and final masses and kinetic energies of a nuclear reaction. The expression came from rearranging the terms of the conservation of energy in a nuclear reaction as in equation 3.7.

$$m_X c^2 + T_X + m_a c^2 + T_a = m_Y c^2 + T_Y + m_b c^2 + T_b \quad (3.8)$$

Where the corresponding subscripts  $X$  and  $a$  are for the particles before the reaction and  $Y$ ,  $b$  for after the reaction. The rearrangement consists in placing all the mass terms in one side of the equation and the kinetic terms in the other.

$$\begin{aligned} Q &= (m_X + m_a - (m_Y + m_b))c^2 \\ &= T_Y + T_b - (T_X + T_a) \end{aligned} \quad (3.9)$$

The top side of equation 3.9 is the mass member in equation 3.7 and the bottom side of equation 3.9 is the kinetic energy member in equation 3.7.

We can write the Q-value for the reactions shown in equations 3.6a and 3.6b. They are shown in table 3.2.

Given the reaction,  $^{41}\text{K}$  will be formed at an excitation energy given by the Q-value (7.8 MeV) plus the center of mass energy. The energy and angular momentum in excess

---

<sup>1</sup>Due to the low energy at which they occur.

<sup>2</sup>See Krane for better reference (37).



will be emitted in the form of a sequence of gamma rays until eventually reaching the ground state. If one of the gammas shown in figure 3.2 is emitted as part of the gamma cascade, the  $^{41}\text{K}$  parent, and thus the reaction 3.6b will be identified.

Detection of such gamma rays may not be as straight forward as it seems due to background as we will show latter, but it is always an unmistakable evidence to look for.

Q-values		
Reaction	Masses ( $u$ )	Q-value (MeV)
$p + ^{14}\text{N} \rightarrow ^{15}\text{O} + \gamma's$	$m_{^{14}\text{N}} = 14.0030740044$ $m_{^{15}\text{O}} = 15.003065618$	7.3
$p + ^{40}\text{Ar} \rightarrow ^{41}\text{K} + \gamma's$	$m_{^{40}\text{Ar}} = 39.9623831237$ $m_{^{41}\text{K}} = 40.9618252579$	7.8

**Table 3.2:** Q-values for different reactions, the proton's mass is;  $m_p = 1.00782503223u$ .

The data used to fill table 3.2 was taken from Krane (37) and also from an online nuclear web-app made by Peter Ekström (38).

### 3.3 Excitation levels

The excess energy from the nuclear reactions could<sup>1</sup> take the form of gamma ( $\gamma$ ) radiation<sup>2</sup>. We will discuss briefly the structure of the gamma energies in this section.

As in the case of atomic physics, the nuclei have internal structure. Different internal configurations or states of its constituents (electrons in the case of atomic physics and nucleons in the case of nuclear physics) correspond to different energy levels of the system<sup>3</sup>.

These states are all unstable and the system decays into a lower energy state after some amount of time, typically a fraction of a second, and in each step down this energy ladder the system's energy is released in the form of a photon<sup>4</sup>. This decay process

<sup>1</sup>Section 5.6.2 treats a case where the nucleus breaks up into other particles.

<sup>2</sup>The binding energy per nucleon is above 8MeV and given table 3.2 the threshold is not passed. Therefore, no nucleons are ejected.

<sup>3</sup>For the sake of simplicity, we will ignore degeneracy or different states that correspond to the same energy level.

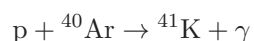
<sup>4</sup>High energy photons, as in the case of nuclear physics, are called gammas

### 3. THEORETICAL FRAMEWORK

(or de-excitation) occurs until the system reaches a base state, from where the system acquires the lowest possible energy.

The de-excitation, from higher energy states to lower ones have to conserve certain properties such as angular momentum and parity. However we will not go into those details. But it is worth mentioning that the level's energy and particular de-excitation photons is unique to each system. A fingerprint in both the atomic case, as well as in the nuclear one.

Taking as example the reaction shown in equation 3.6b, that is:



Potassium 41 happens to be a stable isotope (that is, it will not decay into another element). From table 3.2 we also know that  ${}^{41}\text{K}$  will have 7.2MeV that will be released as  $\gamma$ 's. Figure 3.2 shows some of the  $\gamma$ 's that are close to the ground state.

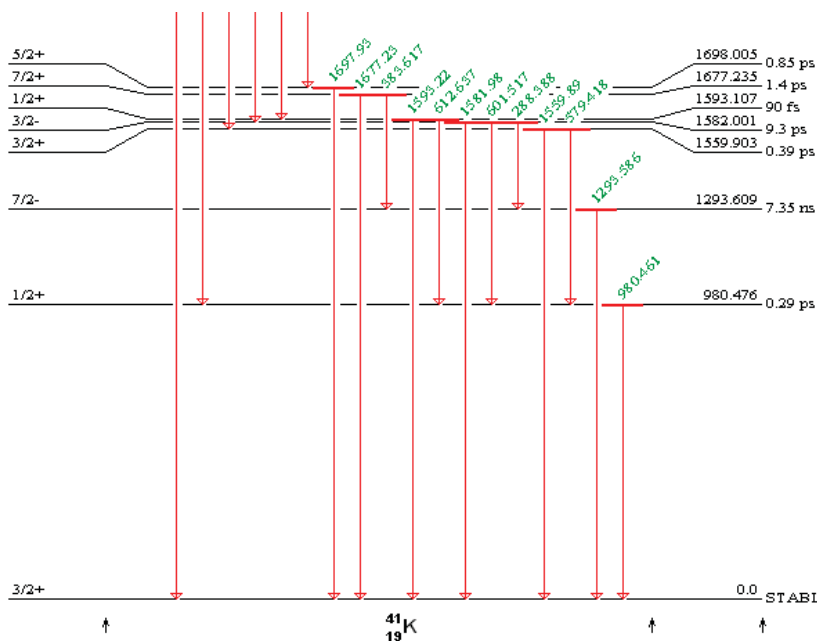


**Figure 3.2: Energy Levels** - Shows some of  ${}^{41}\text{K}$   $\gamma$ 's close to it's ground state. The image was generated with Peter Ekström's Isotope Explorer (39).

The diagonal numbers in figure 3.2 represent the energy of the corresponding gamma, represented by a downward arrow, in units of keV. The energy of the state is

the last but one number on the right and the units are also keV.

Given the reaction, the maximum populated level will be at about 7200keV. But since all of the states eventually go to the ground state emitting various gammas, no matter which path they take, one of the gammas shown in figure 3.2 has to be emitted.

It may not be as straight forward as suggested, due to the background, but it is always a good starting point.

#### 3.3.1 Cross sections

To measure absolute cross sections, we used the experimental array shown in section 4.2.8.5 (of chapter 4). Since the elastically scattered particles and the nuclear reaction products share the same beam intensity, target density and solid angle, it can be easily shown that the alpha cross section can be computed using the following equation:

A relationship between the nuclear and Rutherford cross sections can be established. The corresponding experimental array that uses this fact is shown in section

To measure absolute cross sections, we used the experimental array shown in section 4.2.8.5. Since the elastically scattered particles and the nuclear reaction products share the same beam intensity, target density and solid angle, it can be easily shown that the alpha cross section can be computed using the following equation:

$$\left(\frac{d\sigma_\alpha}{d\Omega}\right)_{\theta_{\text{Lab}}} = \frac{N_\alpha}{N_d} \left(\frac{d\sigma_{\text{El}}}{d\Omega}\right)_{\theta_{\text{Lab}}} \quad (3.10)$$

Which directly links the elastic scattering cross section to the nuclear reaction of interest for each corresponding energy region. This relation makes the normalization of the data for the cross section calculation very direct.  $N_\alpha$ , and  $N_d$ , stand for the number of alphas and deuterons reaching the detector. And  $\left(\frac{d\sigma_{\text{El}}}{d\Omega}\right)_{\theta_{\text{Lab}}}$  stands for the elastic scattering differential cross section at the same angle and energy, in the laboratory reference frame.

The cross section in the center of mass is given by:

$$\frac{d\sigma_\alpha}{d\Omega} = \frac{N_D}{d\Omega T} \quad (3.11)$$

Where  $d\Omega = \pi (r/R)^2$ ,  $N_D$  the particle count at the detector and it is measured by integrating the counts at the region of interest.

### 3. THEORETICAL FRAMEWORK

---

The  $T$  represents the product of the number of projectiles times the number of particles per unit area, it can be taken as a constant factor for each respective run.

$$\left(\frac{d\sigma_R}{d\Omega}\right)_{\theta_{\text{cm}}} = \left(\frac{zZ\alpha\hbar c}{4E_{\text{cm}}}\right) \left(\frac{1}{\sin^4\theta_{\text{cm}}}\right) \quad (3.12)$$

Where  $\alpha = \frac{e^2}{4\pi\epsilon_0\hbar c} \approx \frac{1}{137}$  and  $\hbar c = 197.33\text{MeV} - \text{fm}$ .

In order to transform the Rutherford Cross Section from center of mass to the Lab frame of reference, the following relationship is used (40):

$$\left(\frac{d\sigma}{d\Omega}\right)_{\theta_{\text{Lab}}} = \left(\frac{d\sigma}{d\Omega}\right)_{\theta_{\text{cm}}} \frac{[1 + K + 2K\cos\theta_{\text{cm}}]^{3/2}}{1 + K\cos\theta_{\text{cm}}} \quad (3.13)$$

Where  $K$  is the ratio of masses between the projectile and the target ( $K \approx 1/7$  in the case of deuterons on nitrogen). The relationship of the lab and center of mass angles is given by:

$$\tan(\theta_{\text{Lab}}) = \frac{\sin\theta_{\text{cm}}}{\cos\theta_{\text{cm}} + K} \quad (3.14)$$

Which was solved numerically, given  $\theta_{\text{Lab}} = 35^\circ$  and the corresponding center of mass angle was found to be  $\theta_{\text{cm}} = 39.7^\circ$ . These values were plugged into the differential Cross Section relationship (equation 3.11) and the expected Rutherford differential cross section (equation 3.13) we get, for the case of the elastic scattered deuterons:

$$T = \frac{N_d}{d\Omega \left(\frac{d\sigma_R}{d\Omega}\right)_{\theta_{\text{Lab}}}} \quad (3.15)$$

Using equation 3.11 for the alpha differential CS, in the laboratory system, we get:

$$\left(\frac{d\sigma_\alpha}{d\Omega}\right)_{\theta_{\text{Lab}}} = \frac{N_\alpha}{d\Omega T} \quad (3.16)$$

Expressing 3.16 in terms of 3.15 we obtain:

$$\left(\frac{d\sigma_\alpha}{d\Omega}\right)_{\theta_{\text{Lab}}} = \frac{N_\alpha}{d\Omega \left(\frac{N_d}{d\Omega \left(\frac{d\sigma_R}{d\Omega}\right)_{\theta_{\text{Lab}}}}\right)} = \frac{N_\alpha}{N_d} \left(\frac{d\sigma_{\text{El}}}{d\Omega}\right)_{\theta_{\text{Lab}}} \quad (3.17)$$

Leaving the alpha differential cross section independent of the solid angle.

### 3.3.2 Astrophysics

#### 3.3.2.1 Nucleosynthesis

The experimental array used for this part is shown in section 4.2.8.4 (chapter 4) and the performed tests are presented in section 5.5.2.

Stars are basically massive nuclear reactors, they not only radiate tremendous amounts of energy, they actually *cook* new elements. This process, of fusing light elements into heavier ones, is called nucleosynthesis.

As mentioned before, nuclear fusion can actually take place in the laboratory<sup>1</sup>, the kinetic energy reached by the accelerator's beam is much greater than what is conventionally achieved in a star by their temperature<sup>2</sup>.

Nuclear fusion reactions nevertheless occur in the stars, and the reason for this is the tunnel effect. There is a nonzero probability of fusing nuclei, although their energy is not high enough to overcome Coulomb's repulsion.

Nonzero but it becomes vanishingly small, as the energy decreases. However, given the large amounts of mass<sup>3</sup>, the events are frequent enough to keep the star shining. See references (41) and Krane (37) for this subject, they use slightly different notations but the overall concept is the same.

Given the small cross sections and its temperature dependence (or energy distribution). One can express the cross section ( $\sigma(E)$ ) as (42):

$$\sigma(E) = \frac{S(E)}{E} G(E) \quad (3.18)$$

Where  $E$  is the kinetic energy of the particles at the center of mass,  $G(E)$  is called the *Gamow factor*. The  $S(E)$  is called *astrophysical factor*<sup>4</sup>.

The *Gamow factor* can be expressed in the form:

$$G(E) = e^{-\sqrt{\frac{E_G}{E}}} \quad (3.19)$$

<sup>1</sup>Nuclear scattering can also occur.

<sup>2</sup>And therefore, their average kinetic energy.

<sup>3</sup>And therefore large number of particles (around  $10^{38}$ ).

<sup>4</sup>Also known as *cross section factor*.

### 3. THEORETICAL FRAMEWORK

---

Where  $E_G$  is the so called *Gamow energy*, the square root of the fraction of the energies happens to be:

$$\sqrt{\frac{E_G}{E}} = \frac{2\pi Z_1 Z_2 e^2}{4\pi\epsilon_0 \hbar v} \quad (3.20)$$

Where  $v$  is the velocity,  $Z_1$  and  $Z_2$  are the atomic numbers<sup>1</sup> of the interacting nuclei, etc. The velocity related to the energy via:

$$E = \frac{1}{2}\mu v^2 \implies v = \sqrt{\frac{2E}{\mu}} \quad (3.21)$$

Where  $\mu$  is the reduced mass of the interacting particle pairs  $\mu = \frac{M_1 M_2}{M_1 + M_2}$ . So the *Gamow energy* turns out to be:

$$E_G = 2\pi^2 Z_1^2 Z_2^2 \mu \left( \frac{e^2}{4\pi\epsilon_0 \hbar} \right)^2 \quad (3.22)$$

Equation's 3.22 terms were conveniently grouped in order to use the fine structure constant, equation 3.2a, once again for simplification. Equation 3.22 becomes:

$$E_G = 2\pi^2 Z_1^2 Z_2^2 \alpha^2 \mu c^2 \quad (3.23)$$

Reaction	$Z_1$	$Z_2$	$\mu c^2$ [MeV]	$E_G$ [MeV]
${}^1H + {}^1H$	1	1	469.13	0.4933
${}^1H + {}^{14}N$	1	7	875, 32	24.17
${}^1H + {}^{18}Ne$	1	10	893.66	49.33
${}^1H + {}^{40}Ar$	1	18	915.19	159.86

**Table 3.3:** Gamow energies for various fusion reactions.

Table 3.3 shows the *Gamow energies* for various reactions.

If  $n$  is the density of nuclei present (per cubic centimeter), say protons, then the fusion reaction rate  $R$ . Can be represented by:

$$R = \frac{n_1 n_2}{2} \langle \sigma v \rangle \quad (3.24)$$

---

<sup>1</sup>Also known as proton numbers.

The  $\frac{1}{2}$  factor is for counting the pair of nuclei interacting, the subscripts are for the types of particles interacting. In the case that they are the same, say the proton-proton interaction, we have  $n_1 = n_2 = n$  and therefore  $n_1 n_2 = n^2$ . The angle brackets represent an average of the cross section ( $\sigma$ ) and the particle's velocity ( $v$ ). The Maxwell-Boltzmann velocity distribution ( $f(v)$ ) is:

$$f(v) = \left( \frac{M}{2\pi kT} \right)^{3/2} e^{-\frac{Mv^2}{2kT}} 4\pi v^2 \quad (3.25)$$

Where  $v$  represents the magnitude of the velocity, that is  $v = \sqrt{v_x^2 + v_y^2 + v_z^2}$ ,  $k$  is Boltzmann constant<sup>1</sup>,  $M$  is the mass of the particles and  $T$  is the temperature (in Kelvin  $K$ ).

Using equation 3.25 we can obtain  $\langle \sigma v \rangle$ :

$$\langle \sigma v \rangle = \int_0^\infty \sigma v f(v) dv \quad (3.26)$$

However, for the sake of consistency, we will express equation 3.26 in terms of energy. For non relativistic particles the energy can be expressed as:

We therefore have:

$$dE = Mv dv = \sqrt{2EM} dv \implies dv = \frac{dE}{\sqrt{2EM}} \quad (3.27)$$

Expressing 3.26 and 3.25 in terms of energy with equations 3.21 and 3.27 as well as the cross section from equation 3.18 we get:

$$\begin{aligned} \langle \sigma v \rangle &= \int_0^\infty \frac{S(E)}{E} G(E) \sqrt{\frac{2E}{M}} \left( \frac{M}{2\pi kT} \right)^{3/2} e^{-\frac{E}{kT}} 4\pi \frac{2E}{M} \frac{dE}{\sqrt{2EM}} \\ &= \frac{8\pi}{\sqrt{M}} \left( \frac{1}{2\pi kT} \right)^{3/2} \int_0^\infty S(E) G(E) e^{-\frac{E}{kT}} dE \\ &= \frac{8\pi}{\sqrt{M}} \left( \frac{1}{2\pi kT} \right)^{3/2} \int_0^\infty S(E) e^{-\left(\frac{E_g}{E}\right)^{1/2}} e^{-\frac{E}{kT}} dE \\ &= \frac{8\pi}{\sqrt{M}} \left( \frac{1}{2\pi kT} \right)^{3/2} \int_0^\infty S(E) e^{-\left(\frac{E}{kT} + \sqrt{\frac{E_g}{E}}\right)} dE \end{aligned} \quad (3.28)$$

---

<sup>1</sup> $k = 1.38064 \times 10^{23} J/K = 8.61735 \times 10^{-5} eV/K$

### 3. THEORETICAL FRAMEWORK

Temperatures can vary from their surface to their center, and also from different types of stars. For the sake of simplicity we shall take only one temperature for the stars in the analysis  $10^9 K$ . For comparison we'll use a common fact, that is; at room temperature ( $T_{rt} \approx 300K$ ) and:

$$kT_{rt} \approx \frac{1}{40} \text{eV} = 0.025 \text{eV} \quad (3.29)$$

So  $8kT_{rt} \approx 0.2 \text{eV} \implies 8kT_{rt} \times 10^6 \approx 0.2 \text{MeV}$ , substituting  $T_{rt}$  it turns that the temperature is around  $T \approx 10^9 K$  for an energy of about  $0.2 \text{MeV}$ .

The integral in (3.28) is basically defined by the combined exponentials, since the S factor  $S(E)$  changes slowly. Figure 3.3 shows the individual exponentials and the resulting product.

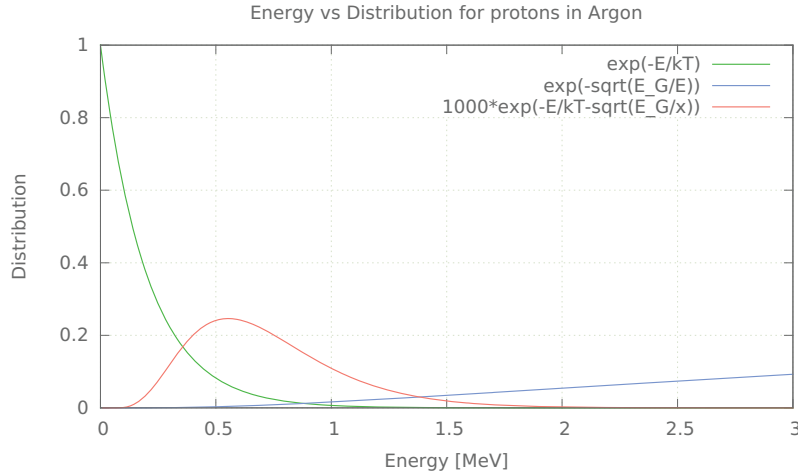


**Figure 3.3: Gamow peak** - An example of the gamow peak, at  $kT = 0.2 \text{MeV}$  for protons in Argon. We present  $1000e^{-\frac{E}{kT} - \frac{E_G}{E}}$  instead of the single exponential part, so the peak is clearly shown.

The peak is conventionally fitted to a Gaussian distribution function and it's standard deviation is called *Gamow window*, which defines a range of energies at which fusion occurs. So for equation (3.26), since  $S(E)$  does not change considerably, the integral only matters around  $E_M$ .



The peak of  $e^{-\frac{E}{kT}-\sqrt{\frac{E_G}{E}}}$  is found when  $\frac{E}{kT} + \sqrt{\frac{E_G}{E}}$  is minimum. That is:

$$\frac{d\left(\frac{E}{kT} + \sqrt{\frac{E_G}{E}}\right)}{dE} = 0 \quad (3.30)$$

That happens at an energy  $E_M$ :

$$E_M = \left(\frac{(kT)^2 E_G}{4}\right)^{1/3} \quad (3.31)$$

So for the different reactions shown in table 3.3 we can obtain the respective  $E_M$ . These energies are low compared to the ones shown in table 3.1, but nevertheless thanks to the tunnel effect fusion is possible in the stars and the maximum probability at which this occurs, is given by the distribution function

Reaction	$E_G$ [MeV]	$E_M$ [keV]
${}^1\text{H} + {}^1\text{H}$	0.493	170.23
${}^1\text{H} + {}^{14}\text{N}$	6.443	400.89
${}^1\text{H} + {}^{18}\text{Ne}$	9.39	454.522
${}^1\text{H} + {}^{40}\text{Ar}$	17.32	557.42

**Table 3.4:**  $E_M$  values for various reactions,  $kT \approx 0.2\text{MeV}$ .

### 3.4 Fluid Considerations

The relations for supersonic flow discussed in this section are in particular for gas flow. The corresponding experimental setup is shown in chapter 4. The data is presented in chapter 5 in sections 5.1 and 5.2.

An extensive systematic parameter search was performed for optimizing the characteristics of the gas jet target and, at the same time, adapt the corresponding gas flows to the pumping capabilities we expected to achieve.

This was done with the help of software that automated much of the calculations, the software was originally written, in the C programming language, by Dan Shapira. Part of the work I performed was an effort to update the program so it may compile with the latest compiler available and transcribe part of the program to the computer, since there was only a printed version available.

### 3. THEORETICAL FRAMEWORK

---

Fox and Ackroyd (43, 44) are the basic literature references used for the fluid theory, however (45) and (3) were also consulted. The way the [supersonic gas jet target](#) is obtained is through the flow of a [nozzle](#) from a high pressure reservoir to a low pressure one.

Once the critical pressure ratio condition between the intake of the [nozzle](#) and the surrounding jet exit pressure is attained, then the flow becomes invariantly sonic. If the [nozzle](#) area increases as the flow goes through the [nozzle](#) then the local speed of the flow increases and the flow becomes supersonic.

The thermodynamic relations for the supersonic flow, also called isentropic flow equations, are:

$$\frac{T}{T_0} = \left[ 1 + \frac{\gamma - 1}{2} M^2 \right]^{-1}, \quad (3.32a)$$

$$\frac{\rho}{\rho_0} = \left[ 1 + \frac{\gamma - 1}{2} M^2 \right]^{\frac{-1}{\gamma - 1}}, \quad (3.32b)$$

$$\frac{p}{p_0} = \left[ 1 + \frac{\gamma - 1}{2} M^2 \right]^{\frac{-\gamma}{\gamma - 1}}, \quad (3.32c)$$

$$\frac{A}{A^*} = \frac{1}{M} \left[ \frac{1 + \frac{\gamma - 1}{2} M^2}{\frac{\gamma + 1}{2}} \right]^{\frac{\gamma + 1}{2(\gamma - 1)}} \quad (3.32d)$$

Where the  $T$ ,  $\rho$ ,  $p$  and  $A$  are the exit flow properties temperature, density, pressure and area. The subscript zero represents the initial condition of the flow right before the nozzle.

The  $A^*$  represents the throat area of the nozzle,  $M$  the [Mach](#) of the exit flow. And lastly  $\gamma$ , represents the specific heat ratio that is  $\gamma = C_p/C_v$ , where  $C_p$  is the heat capacity at a constant pressure and  $C_v$  is the heat capacity at a constant volume.

With these equations we can determine the thermodynamic state. From the area ratio equation we can determine the [Mach](#) number of the flow for Nitrogen ( $\gamma = 1.4$ ), see figure 3.4.

In our case the area ratio is close to 10 therefore the corresponding [Mach](#) is around 4. It is important to note that the deductions of these formulas assume that there are no [shocks](#) inside the [nozzle](#).

In figure 3.5 the [nozzle](#) and the catcher are shown. The initial pressure of the gas and the properties of the [nozzle](#) define the [pumping speeds](#) and the target properties.

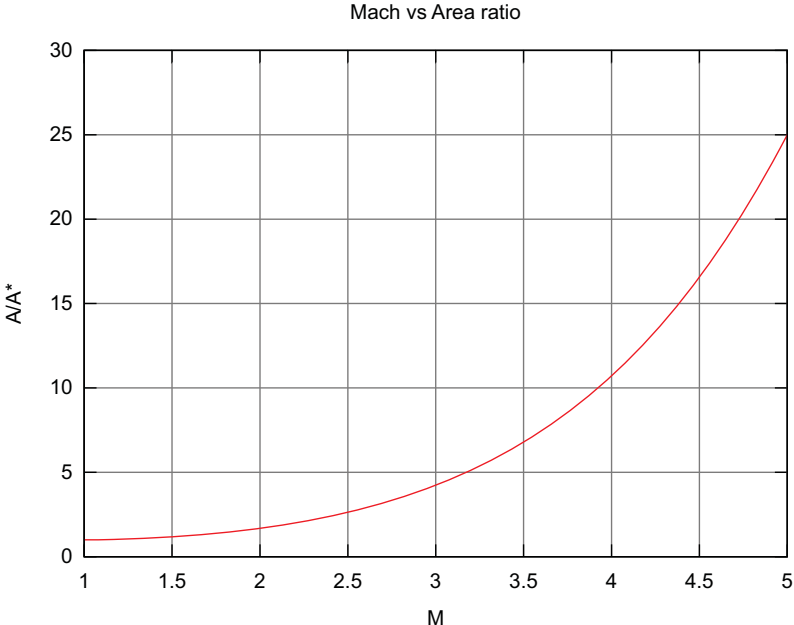


Figure 3.4: Area ratio - Shows the area ratio between the nozzle aperture and its throat.

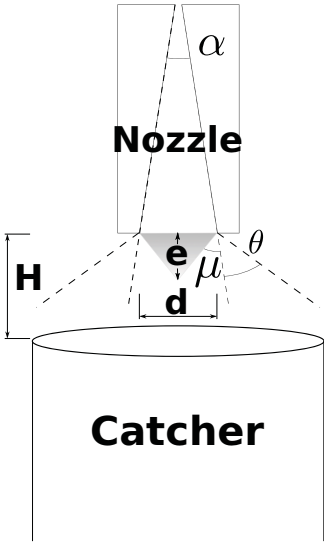


Figure 3.5: Nozzle and catcher - Layout of the nozzle and its catcher.

### 3. THEORETICAL FRAMEWORK

---

Its important to know that given a shock pattern we can measure the angles of the “X”’s in the shock region and infer the [Mach](#) number via (43):

$$\beta = \sin^{-1}\left(\frac{1}{M}\right) \quad (3.33)$$

From the equation:

$$\dot{m} = \gamma^{1/2} \left[ \frac{\gamma + 1}{2} \right]^{-\frac{\gamma+1}{2(\gamma-1)}} (p_0 \rho_0)^{1/2} A^* \quad (3.34)$$

We are able to obtain the [mass flow rate](#). Notice that it only depends on parameters before the throat. If we want the to express the pressure in [Torr](#), the density in grams/cm<sup>3</sup>, and the area in cm<sup>2</sup> we have to multiply it by  $\sqrt{133.32 \times 10} = 36.5$ .

In the case of nitrogen  $\gamma = 1.4$ , using atmospheric pressure  $p_0 = 760$  [Torr](#), and its respective density  $\rho_0 = 10^{-3}$  g/cm<sup>3</sup>, the throat area of the [nozzle](#) is  $A^* = 2 * 10^{-2} * 7.5 * 10^{-1} \text{cm}^2 = 1.5 * 10^{-2} \text{cm}^2$ .

This gives us a [mass flow rate](#) of:

$$\dot{m} \approx 0.17 \text{g/s} \quad (3.35)$$

We will use this value to calculate the [throughput](#) for the central stage and the surrounding one. We obtain this value by:

$$q_m = \frac{\dot{m}}{\text{molweight}} (760 \times 22.4) = \frac{\dot{m}}{\text{molweight}} (17024) \quad (3.36)$$

So in our case molweight=28g/mole:

$$q_m \approx 10^2 \text{Torr(liter/sec)} \quad (3.37)$$

We shall remember this value when we calculate the [pumping speeds](#) of the central stages of our system.

From equation 3.32b we can obtain:

$$n = n_0 \left[ 1 + \frac{\gamma - 1}{2} M^2 \right]^{\frac{-1}{\gamma-1}} \quad (3.38)$$

Remembering that  $M \approx 4$ ,  $\gamma = 1.4$  and  $n_0 = 2.6 \times 10^{19}$  molecules/cm<sup>2</sup>, we obtain:

$$n \approx 7 \times 10^{17} \frac{\text{molecules}}{\text{cm}^3} \quad (3.39)$$

### 3.4 Fluid Considerations

---

The exit pressure, from the nozzle, is estimated by using equation 3.32c remembering that the Mach at the exit of the nozzle is around 4 we get ( $p_0 \approx 760$  Torr):

$$p \approx 5 \text{ Torr} \tag{3.40}$$

In the same manner we can calculate the expected temperature ( $T_0 \approx 300$  K):

$$T = 300(1 + 0.2 * 16)^{-1} \approx 70 \tag{3.41}$$

Using these values we can estimate the density by using the formula:

$$n = \left(\frac{N_A}{R_0}\right) \left(\frac{P}{T}\right) = 9.656 \times 10^{18} \frac{P}{T} \tag{3.42}$$

Plugging in the calculated values of P and T we get:

$$n \approx 6.8 \times 10^{17} \frac{\text{molecules}}{\text{cm}^3} \tag{3.43}$$

Which is consistent with the past result. If we multiply by the nozzle thickness we obtain the number of particles per square centimeter. Since the nozzle is rectangular we can obtain the maximum (length = 0.75cm) and the minimum (length = 0.28cm) thickness. Rectangular nozzles are not uncommon in nuclear physics experiments reference (46) uses a rectangular nozzle. They have also been subject of numerical simulation studies in (12).

Giving us respectively:

$$n \approx 5.25 \times 10^{17} \text{ molecules/cm}^2 \tag{3.44}$$

and

$$n \approx 1.96 \times 10^{17} \text{ molecules/cm}^2 \tag{3.45}$$

Considering molecular nitrogen  $N_2$  we can express equation 3.44 in terms of particles per square centimeter:

$$n \approx 1.5 \times 10^{18} \text{ particles/cm}^2 \tag{3.46}$$

### 3. THEORETICAL FRAMEWORK

---

The expected length of the target, before the first **shock** can be estimated from the characteristics of the nozzle, as seen from the figure. The angle  $\mu$  can be calculated from the equation:

$$\mu = \frac{\pi}{2} - \tan^{-1} \sqrt{M^2 - 1} \quad (3.47)$$

Using  $M=4$  we get:

$$\mu = \frac{\pi}{2} - \tan^{-1} \sqrt{15} \approx 0.25 \quad (3.48)$$

Now the length of the target is given by:

$$e = \frac{d}{2} \tan \left( \frac{\pi}{2} - \mu + \frac{\alpha}{2} \right) \quad (3.49)$$

$\alpha$ , see figure 3.5, can be obtained from the entrance and exit **nozzle** apertures and length, as seen from figure 3.6.

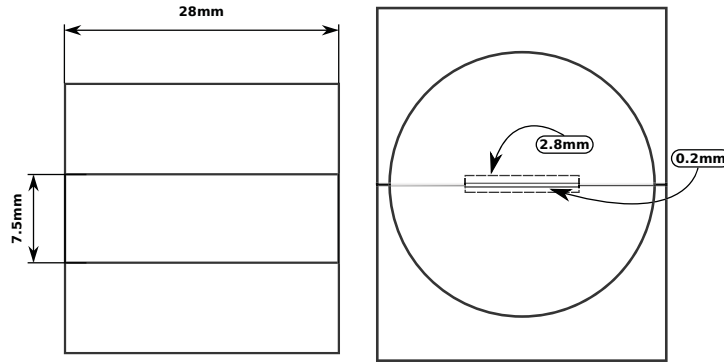


**Figure 3.6: Nozzle dimensions** - Shape and sizes for one of the nozzles. Left side shows one half of the nozzle seen from the top, right side shows the nozzle seen from the back.

$$\begin{aligned}
\alpha &= \tan^{-1} \left( \frac{(\text{exit} - \text{entrance})/2}{\text{length}} \right) \\
&= \tan^{-1} \left( \frac{(2.8 - 0.2)/2}{28} \right) \\
&= \tan^{-1} \left( \frac{1.2}{28} \right) \\
&\approx \tan^{-1}(0.043) \approx 0.043
\end{aligned} \tag{3.50}$$

We know that  $d = 2.8\text{mm}$  so we get:

$$e \approx 6\text{mm} \tag{3.51}$$

We call this the length of the target, the tongue. Now from the first figure another angle is defined . We can use it for estimating how much of the flow escapes the central catching system.

This angle is defined by the equation:

$$\begin{aligned}
\theta &= \frac{\pi}{2} \left( \sqrt{\frac{\gamma+1}{\gamma-1}} - 1 \right) + \tan^{-1} \left( \sqrt{M^2 - 1} \right) \\
&\quad - \sqrt{\frac{\gamma+1}{\gamma-1}} \tan^{-1} \sqrt{\frac{\gamma-1}{\gamma+1}} (M^2 - 1)
\end{aligned} \tag{3.52}$$

For air with  $M=4$  we have  $\theta = 64.6^\circ$ , from the image we see that the escape angle ( $\theta_e$ ) of the flow goes as:

$$\theta_e = \theta + \alpha/2 \approx \theta = 64.6^\circ. \tag{3.53}$$

The projection radius onto the catcher is  $T \times \tan(\theta_e)$ , T is around 1cm so the outer projection is  $(1\text{cm}) \times (2) = 2\text{cm}$ .

This is for the escaped part, the catcher has 5cm in radius so it catches most of the jet (we purposely over estimated it). However we know some part of it must have escaped, a small fraction of what entered we estimate around 10% of what entered.

The free expansion depends on the pressure surrounding the jet. The jet will self adjust (within limits) to variations in pumping speed of the roots blower. This is what makes this setup so easy to achieve.

### 3. THEORETICAL FRAMEWORK

---

Since we calculated, equation 3.37, that the [throughput](#) should be around:

$$q_m = 10^2 \text{ Torr(liter/sec)} \quad (3.54)$$

The escaped [throughput](#) is around:

$$q_m \text{ Fraction} = 10 \text{ Torr(liter/sec)} \quad (3.55)$$

To obtain the [pumping speed](#) we must first know the stagnation conditions of the jet, that is what happens with the flow after it has slowed down (after the [shocks](#)). First we need to know the [Mach](#) number in free expansion and from there we are able to get the stagnation pressure.

For the pressure surrounding the jet we can calculate it by knowing the [throughput](#) which we estimated to be around 10% of the overall, given our [pumping speed](#) in that stage we expect the surrounding pressure to be about 0.1 Torr ( $p_3$ ).

To get the [Mach](#) in free expansion we use equation 3, naming  $M_2$  the [nozzle](#) exit [Mach](#) and  $M_3$  the free expansion [Mach](#).

$$\frac{p_3}{p_2} = \left( \frac{\frac{\gamma-1}{2} M_2^2 + 1}{\frac{\gamma-1}{2} M_3^2 + 1} \right)^{\frac{-\gamma}{\gamma-1}} \quad (3.56)$$

From here we just express  $M_3$  in terms of everything else in the equation:

$$M_3 = \sqrt{\frac{-1 + \left(1 + \frac{\gamma-1}{2} M_2^2\right) \left(\frac{p_2}{p_3}\right)^{\frac{\gamma-1}{\gamma}}}{\frac{\gamma-1}{2}}} \quad (3.57)$$

We want the pressure ratio to be around  $p_2/p_3 \approx 100$  this gives us an  $M_3$  of about eight.

Using  $M_3$  we can finally estimate the value of the stagnation pressure the approximate pressure the central pump will be pumping.

$$p_s = p_0 \left(1 + \frac{2\gamma}{\gamma+1} (M_3^2 - 1)\right)^{\frac{-1}{\gamma-1}} \left(\frac{(\gamma+1)M_3^2}{(\gamma-1)M_3^2 + 2}\right)^{\frac{\gamma}{\gamma-1}} \quad (3.58)$$

If  $p_0 = 760$  Torr then  $p_s \approx 1.7$  Torr, given the [throughput](#) and this pressure we can calculate the approximate [pumping speed](#) for the central stage.

$$S_m = \frac{q_{massflow}}{p_s} = \frac{10^2 \frac{\text{Torr liter}}{\text{sec}}}{1.7 \text{ Torr}} \approx 58 \frac{\text{liter}}{\text{sec}} \quad (3.59)$$



The actual **pumping speed** is a bit higher (around 60 l/s). The measured pressure at the intake of the central pump in our system was about 0.56 **Torr** which is close to the expected 1.7 **Torr**.

And the **pumping speed** of the surrounding area is estimated by:

$$S_m = \frac{q_m \text{Fraction}}{p_3} \approx \frac{10 \frac{\text{Torr liter}}{\text{sec}}}{0.1 \text{ Torr}} = 100 \frac{\text{liter}}{\text{sec}} \quad (3.60)$$

We over estimated the the outer **pumping speed**, since that was the most expensive part we had to make sure it was going to be upgradable for handling other types of gases eventually. The **pumping speed** is about 1400 liters/sec, the measured pressure is about 0.1 **Torr**.

It is important to notice that the surrounding pressure affects  $\theta$ , see figure 3.5, which affects at the same time the amount of gas that escapes which affects the pressure. More importantly,  $\theta$  does not follow a straight profile. In order to take into account this problems we used about 10 times the estimated pumping speed for the pump used in this stage. Also the system itself has an air cooling system which at the same time gets inside the **roots system**, a “*cooling leak*”.

The system was arranged in accordance with figure 3.7 in which we have. Among multiple configurations this arrangement turned out to be optimal. We decided to use a well accepted standard within the vacuum industry, everything separated in modules which would allow independence in each pumping stage and to make improvements to parts of the system maintaining, at the same time, the rest of the system functional.

This means that in the future we can improve the **pumping speed** in a stage, just by connecting an extra pump to the crosses. We only need to replace one of the flanges (or lids) with a pump adapter.

The standard allows us to connect and disconnect quickly any of the flanges or adapters, allowing us to quickly make changes to our experimental array. Moving a detector, replacing them, changing the target angle with respect with the beam (so we get a variable thickness target). Even changing the entire experimental setup can be performed in minutes.

In figure 3.7 we have the main chamber which is the scattering chamber for the jet. Here we have a special feedthrough flange which is connected to our **nozzle** so the supersonic jet can occur, immediately the jet is caught by a catcher defined by a central pipe that goes to a high speed **mechanical pump**, this pipe is concentric to a larger in

### 3. THEORETICAL FRAMEWORK

---

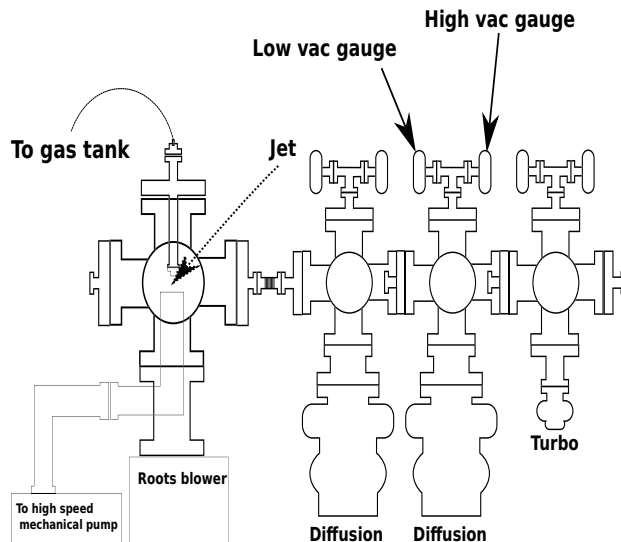


**Figure 3.7: Pumping array** - The pumping system array schematic. See also section 4.1.2 for more details

diameter pipe that pumps most of what was not caught by the central one, we use for this stage a high speed [roots system](#).

The catcher is threaded at the bottom so the distance from it to the [nozzle](#) can be varied just by turning it, this was mainly done for fine tuning. So we can alter the height in case the experiment requires it to be so.

Note that we have ignored some interesting phenomena that also may occur. For example the gas molecules can be excited because of the violence on which the gas flows. Verkhovtseva treats the case of Argon excitations in the article (47).

Being the energy scale for nuclear physics much higher than the electronic excitation levels, we can safely ignore most of this effects in our detectors.

In order to visualize the flow an experimental technique called Schlieren is intended to be used (48).

#### 3.4.1 Differential Pumping System

The experimental results for this section are found in section 5.1 of chapter 5.

The theoretical framework for handling the [throughputs](#) is mostly taken from [\(49\)](#) and partly from [\(50\)](#). However, as in the past section. It is applied specifically for our system's conditions.

From there on we have what we call a differential pumping system, the expected pressure in the volume surrounding the jet is about 0.1Torr which is low compared to the supersonic jet column ( $\approx 10$  Torr) however 0.1Torr is too high for an accelerator we need the system to be at least  $10^{-6}$  Torr to be able to connect it to the accelerator.

This is where the differential pumping system comes into place. In a simplified manner, a differential pumping system is a series of pumping stages (vacuum chambers) connected by holes that are big enough so most of the accelerator beam can go through but small enough so that the [throughput](#) between each chamber is limited in such a way that the pump in the respective stage can handle it.

There are various flow regimes and multiple ways of classifying them. Since we are going to handle low pressures (less than atmospheric), it is best we use the [Knudsen's number](#), which is the ratio of the mean free path ( $\lambda$ ) and the aperture size:

$$K_n = \frac{\lambda}{D} \tag{3.61}$$

Where  $\lambda$  (in centimeters) can be expressed in terms of the pressure (for Nitrogen) as:

$$\lambda = \frac{5 \times 10^{-3}}{p} \tag{3.62}$$

And  $D$  is the characteristic length of the aperture (the diameter in our case), which is about 5mm. Typically the inverse of [Knudsen's number](#) is used to determine the flow regime.

$$\text{flow regime} = \begin{cases} 110 < \frac{1}{K_n} & \text{Viscous} \\ 1 < \frac{1}{K_n} < 110 & \text{Intermediate} \\ \frac{1}{K_n} < 1 & \text{Molecular} \end{cases}$$

In [table 3.5](#) the  $\lambda$ , Knudsen's number  $K_n$  and its inverse are shown in terms of the pressure.

### 3. THEORETICAL FRAMEWORK

---

p(Torr)	$\lambda$ (cm)	$K_n$	$\frac{1}{K_n}$
760	$6.5 \times 10^{-6}$	$1.3 \times 10^{-5}$	$7.6 \times 10^4$
10	$5 \times 10^{-4}$	$10^{-3}$	$10^3$
1	$5 \times 10^{-3}$	$10^{-2}$	$10^2$
$10^{-1}$	$5 \times 10^{-2}$	$10^{-1}$	10
$10^{-2}$	$5 \times 10^{-1}$	1	1
$10^{-3}$	5	10	$10^{-1}$
$10^{-4}$	$5 \times 10^1$	$10^2$	$10^{-2}$
$10^{-5}$	$5 \times 10^2$	$10^3$	$10^{-3}$
$10^{-6}$	$5 \times 10^3$	$10^4$	$10^{-4}$

**Table 3.5: Knudsen's number** - Mean free path, **Knudsen's number** and its inverse in terms of the pressure. The aperture diameter used for  $K_n$  is 0.5cm.

In our case the flow, from the surrounding area of the jet to the first chamber in the differential pumping system, is intermediate ( $p \approx 0.1$  Torr).

$$\frac{1}{K_n} = 10 \quad (3.63)$$

From there on the flow is molecular. To be able to calculate the pressures on the chambers of the differential pumping system, we first need calculate the **throughput** and we also need to know the pumping speeds of the available pumps.

The total the total throughput for each chamber is:

$$Q_{\text{Tot}} = Q_{\text{Chambers}} + Q_{\text{Leaks}} \quad (3.64)$$

We can't really estimate beforehand the  $Q_{\text{Leaks}}$  term, in equation 3.64, since it depends in whether the system was sealed correctly or that the pumps<sup>1</sup> might have a leak etc. The strategy is to assume that the  $Q_{\text{Leaks}}$  term is much smaller than the  $Q_{\text{Chambers}}$  term. Therefore we have:

$$Q = Q_{\text{Tot}} \approx Q_{\text{Chambers}} \quad (3.65)$$

The idea is to over estimate the pressure requirements, much lower than the required for the connection to the accelerator and in that matter compensate for the  $Q_{\text{Leaks}}$ .

---

<sup>1</sup>Some haven't been used in a long time and their vacuum integrity is in question.

The [throughput](#) through an aperture is calculated from the general formula:

$$Q = AP_1 \left( \frac{P_2}{P_1} \right)^{\frac{1}{\gamma}} \left[ \frac{2\gamma}{\gamma-1} \frac{R_0 T_1}{M} \left( 1 - \frac{P_2}{P_1} \right)^{\frac{\gamma-1}{\gamma}} \right]^{1/2} \quad (3.66)$$

Which is zero for  $P_1 = P_2$  and is maximum for:

$$\frac{P_2}{P_1} = \left[ \frac{2}{\gamma+1} \right]^{\frac{\gamma}{\gamma-1}} = r_c \quad (3.67)$$

Where  $r_c$  is the critical pressure ratio. For the case of nitrogen (basically air in general) the critical ratio is:

$$r_c = 0.525 \quad (3.68)$$

Simplifying with the appropriate units we can express the critical throughput as:

$$Q_c \approx 20AP_1 \quad (3.69)$$

Where  $P_1$  is in [Torr](#) and  $A$  is in  $cm^2$  giving us  $Q_c$  in [Torr](#) (liter/sec).

In the case where the flow is molecular we use:

$$Q = 11.6AP \quad (3.70)$$

Again, with the appropriate units. We would normally consider the throughput out of chamber a connected to chamber b as:

$$Q_{a \rightarrow b} = 11.6A(P_a - P_b) \quad (3.71)$$

However the pressure drop of each successive chamber is estimated to be 0.1 smaller than the last one so we can basically ignore  $P_b$  for the sake of simplicity.

Now, since there is no proper way to treat intermediate flow from the jet chamber to the first pumping stage of the differential pumping system, we will over estimate the flow by considering it viscous with the  $Q_c$  formula.

$$Q_{J \rightarrow 1} = 20AP_J \quad (3.72)$$

### 3. THEORETICAL FRAMEWORK

---

We used the same opening diameter for all the holes which is  $D = 0.5\text{cm}$  so the area is:

$$A = \pi D^2/4 \approx 0.2\text{cm}^2 \quad (3.73)$$

Remembering that  $P_J \approx 0.1\text{Torr}$  we therefore have:

$$Q_{J \rightarrow 1} \approx 8 \times 10^{-1} \text{Torr (liter/sec)} \quad (3.74)$$

This is what goes into the first stage of the differential pumping system. In order to calculate the expected pressure we use the next relation:

$$P = \frac{Q}{S} \quad (3.75)$$

Where  $P$  is the maintained pressure at the chamber and  $S$  is the pumping speed of the respective chamber. From our estimations we calculated that the [pumping speed](#) was around  $S_1 \approx 10^3$  liters/sec so the expected pressure in that chamber is:

$$P_1 = \frac{Q_{J \rightarrow 1}}{S_1} \approx \frac{8 \times 10^1 \text{Torr (liter/sec)}}{10^3 \text{ liter/sec}} = 8 \times 10^{-4} \text{Torr} \quad (3.76)$$

As it was mentioned before the the flow from this chamber to the next is molecular since the pressure is so low, that the  $\lambda$  of the gas molecules is about 6cm. Remembering that the aperture's hole is only half a centimeter, we get the inverse [Knudsen's number](#) to be:

$$\frac{1}{K_n} \approx 0.08 \quad (3.77)$$

Which confirms the former declaration that the flow is molecular. It's important also to notice that the pressure range at which the [diffusion pump](#) can start to work is around that pressure (the expected [pumping speed](#) decreases if the pressure is higher) so it is paramount that the pressure, the flow regime and the [pumping speed](#) match up like this in the first stage.

For the next pumping stage the [throughput](#) is:

$$\begin{aligned} Q_{1 \rightarrow 2} &= 11.6AP_1 = 11.6(0.2)(8 \times 10^{-4}) \text{Torr (liters/sec)} \\ &\approx 1.8 \times 10^{-3} \text{Torr (liters/sec)} \end{aligned} \quad (3.78)$$

Since, according to our design, we used a second almost identical [diffusion pump](#) ( $S_2 \approx S_1 \approx 10^3 \text{liters/sec}$ ) we get the corresponding expected pressure to be:

$$P_2 = \frac{Q_{1 \rightarrow 2}}{S_2} = \frac{1.8 \times 10^{-3}}{10^3} \text{ Torr} = 1.8 \times 10^{-6} \text{ Torr} \quad (3.79)$$

At this expected pressure we could theoretically finally connect the system to the accelerator. However we added a last stage just to be safe, since all of the calculations have been estimates and our physical system is itself perfect. The [throughput](#) for the last stage is:

$$Q_{2 \rightarrow 3} = 11.6AP_2 = 11.6(0.2)(10^{-6}) \text{ Torr liter/sec} \approx 4 \times 10^{-6} \text{ Torr liter/sec} \quad (3.80)$$

According to our design, the pump to be used is a  $S_3 = 200 \text{liters/sec}$  [turbo pump](#), so therefore the expected pressure is:

$$P_3 = \frac{Q_{2 \rightarrow 3}}{S_3} = \frac{4 \times 10^{-6}}{200} \text{ Torr} \approx 2 \times 10^{-8} \text{ Torr} \quad (3.81)$$

This is, in principle, lower than the accelerators pressure. For the two last stages, small leaks might affect significantly the final expected pressure. Also when connected to the accelerator's pipe gas flow can enter the chamber, not to mention that the conductance of the (long) pipes from the accelerator to the turbo chamber. Basically making impossible to reach this theoretical pressure.

#### 3.4.2 Pumpdown theory

So far we have concentrated in an equilibrium state, where the throughput of the pump equals the throughput of the leak of the orifices. However this is done at low pressures, the system has to be turned on eventually to reach the pressures at which the pumps are expected to perform inside the [differential pumping system](#).

This can give us an estimate in how much time we need to reach certain pressures, at given pumping speeds.

The pressure time relationship happens to be exponential and the reason can be deduced more or less simply. At a given temperature and a fixed volume, the pressure decrease can be attributed to a decrease in number of particles in the system.

### 3. THEORETICAL FRAMEWORK

---

This can be easily seen from the ideal gas law:

$$PV = NkT \quad (3.82)$$

Where  $P$ ,  $V$ ,  $T$ ,  $N$  and  $k$  are respectively the pressure, volume, temperature, number of particles and the Boltzmann constant<sup>1</sup>.

However, in practice, the quantities that can ultimately be controlled and measured directly are  $P$ ,  $V$ , and  $T$ , *not*  $N$ . If we want to know the rate of change of  $N$  at a fixed temperature we have to know the rate of change of  $PV$ <sup>2</sup>. This will ultimately be related to the rate of change of the pressure and we can obtain the desired time-pressure relationship. So we have:

$$\frac{dN}{dt} \propto Q = \frac{d(PV)}{dt} = P \frac{dV}{dt} + \frac{dP}{dt} V \quad (3.83)$$

The  $P \times dV/dt$  is zero since we considered a constant volume. Actually there should be another term that is related to leaks, the number of particles fluctuates because of this. However we are ignoring it for the sake of simplicity. So from equation 3.83 we get:

$$\frac{dN}{dt} \propto Q = \frac{dP}{dt} V \quad (3.84)$$

Now, the throughput of the pump is related to its pumping speed and the pressure of the chamber to be evacuated via  $Q = -SP$ <sup>3</sup>, where  $S$  is the pumping speed<sup>4</sup>. So we have that:

$$Q = -SP = V \frac{dP}{dt} \implies \frac{dP}{P} = -\frac{S}{V} dt \quad (3.85)$$

Solving equation 3.85 we get:

$$P(t) = P_0 e^{-\frac{S}{V}t} \quad (3.86)$$

Where  $P_0$  is an initial pressure, we obtain the aforementioned exponential relationship. Leak sources<sup>5</sup> were ignored, and also the flow regime of the gas was ignored<sup>6</sup>.

---

<sup>1</sup> $k \approx 1.38 \times 10^{-23} J/K$ .

<sup>2</sup>The  $dN/dt \propto d(PV)/dt$  happens to be the throughput  $Q$ .

<sup>3</sup>It is negative since the chamber is being evacuated.

<sup>4</sup>Its units are in volume per unit time, liters/second for example.

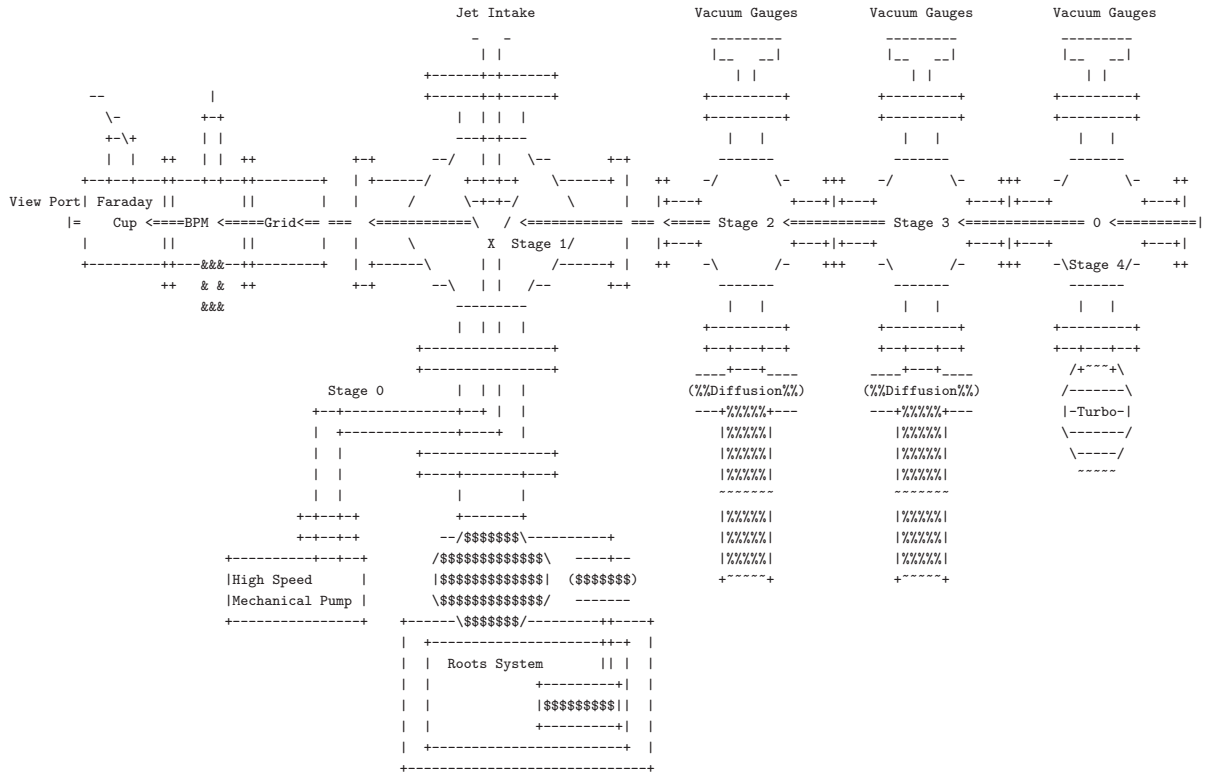
<sup>5</sup>It's important to remember that  $Q_{\text{Tot}} = Q_{\text{Chambers}} + Q_{\text{leaks}}$ , equation (3.64)

<sup>6</sup>The conductance of the pipes change with the flow regime.



# 4

## Experimental Methods



“When one knows of what a man is capable, for better and for worse, one also knows that it is not the human being itself who must be protected but the possibilities that he has within him— in other words, his freedom”

—*Albert Camus*

French Nobel Prize winning author

## 4. EXPERIMENTAL METHODS

---

The hardware of the project was the most time consuming part. It required coordinated effort to put the system together and get it working.

For the sake of brevity I shall only cover part of the work in this chapter.

### 4.1 Design

During the theoretical calculation phase the design was also being done and re-done. The calculations were done in terms of what we estimated our facility capabilities would be, [pumping speeds](#), height of the [beamline](#)<sup>1</sup>, power supply etc. And consequently the design was adapted to the new numbers, adding pumping stages, changing aperture sizes, removing and adding vacuum hardware in order to adapt to the “better” calculations.

Additionally we had to cope with the limitations of what could be built in a reasonable time at our shop.

#### 4.1.1 Old Designs

Taking into account everything above, the design phase was started. The best starting place was the previous work on these systems.

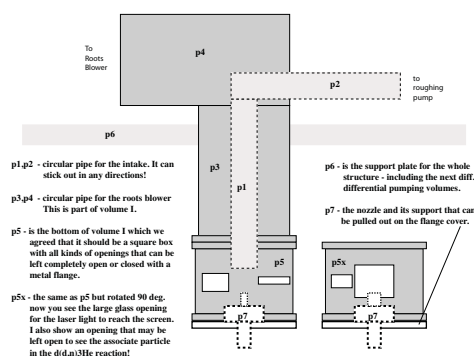


Figure 4.1: Old jet - An old version of the system.

Figure 4.1 shows a sketch of one of the first versions of the jet system. The sketch was done by Dan Shapira in our first discussions of ideas of how the system should be designed.

---

<sup>1</sup>Around 180cm.

It only presents the first two pumping stages, the ones inside the [scattering chamber](#).

Discussion in leaving apertures for the detectors and optical windows is also partly shown in the figure. The windows would provide us with the ability of mounting an optical system outside the [scattering chamber](#) in order to characterize the jet via a technique called [Schlieren](#)<sup>1</sup>.



**Figure 4.2: Square chamber** - A 3D sketch of the [scattering chamber](#) as a box. It has X-ray view so the inside is shown.

A 3D version of this was made, see [figure 4.2](#), some of the apertures were for the detectors and others for the windows. The [nozzle](#) and the catcher are also shown in the inside of the chamber.

However the first problems with the construction started to arise. It was still not clear how to connect the rest of the stages. The square chamber was to be surrounded by a third stage and that included the [nozzle](#). The system was starting to get a bit too big.

Another concern was that the square chamber posed a threat to the vacuum. It is a lot cleaner to weld a circular region than a square one, the main reason is that the corners tend to be problematic and they are potential leaks.

One of the latter designs, [figure 4.3](#), solved most of the problems. It showed how to include the third stage and eliminated the potential leak problem, it also started to show us insight in how to put the charged particle detectors inside the system.

---

<sup>1</sup>The final system also takes this into account.

## 4. EXPERIMENTAL METHODS

---

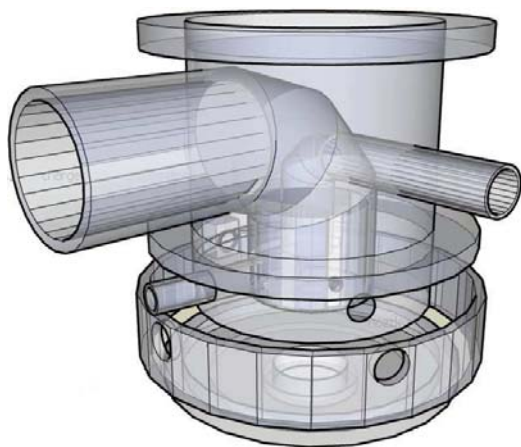


**Figure 4.3: Cylindrical chamber** - A 3D sketch of the cylindrical chamber. It has an X-ray view so the inside can be seen, one of the detectors is also shown.

However the problem of the size and weight started to become a real concern. Additionally the [concentric pipes](#) (they are 3), started to become a real technical challenge to be performed.

The height of the [beamline](#) also had to be considered afterwards since information on the roots system started to be available. It was going to be big and heavy, we could not adapt the roots system to the current design, it had to be the other way around.

For the jet, the orientation was unimportant, flowing upwards, downwards, sideways had no considerable performance problem.

Meanwhile the [nozzle](#) was also under development, [figure 4.4](#). Right from the beginning we wanted a square [nozzle](#) since it best resembles a solid target. The cylindrical base was a chamber where the hose from the gas bottle was to be connected.

These designs helped visualize how the system should be placed. What we should and shouldn't do. They were the most representative of the multiple iterations the system went through.

### 4.1.2 Final Designs

The designs in the past section, as well as others that were not included, had a common problem. They were too specific and required us to build a whole set of pieces just for the system.

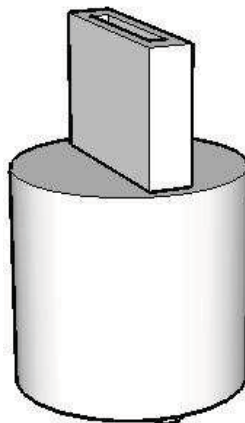


**Figure 4.4: Old nozzle** - One of the first designs of the nozzle it has a rectangular aperture to better resemble a solid target

This appeared as a big challenge since we would like to use the jet with different gases, upgrade it in general so we could re-use the jet for different experiments.

We can't afford to re-build from scratch a different system for each type of gas and each type of experiment. That is inadmissible.

Among many different possibilities evaluated we decided to adopt a vacuum standard from which we could:

1. Purchase most of the parts needed.
2. Modify a reduced number of parts.
3. Adapt our pumps and gauges easily.
4. Easy and fast to assemble.

The [ISO](#) vacuum standard allowed us to satisfy all of these points. Not only that, it also suggested how the design should be in a very natural manner. It almost became obvious how the entire array should be.

Figure 4.5 shows the main idea on how it was originally thought (an insight was given in figure 3.7). The entire [differential pumping system](#) was spread out into the [beamline](#) . This allowed us to easily adapt the available pumps to the system, since there was enough space.

#### 4. EXPERIMENTAL METHODS

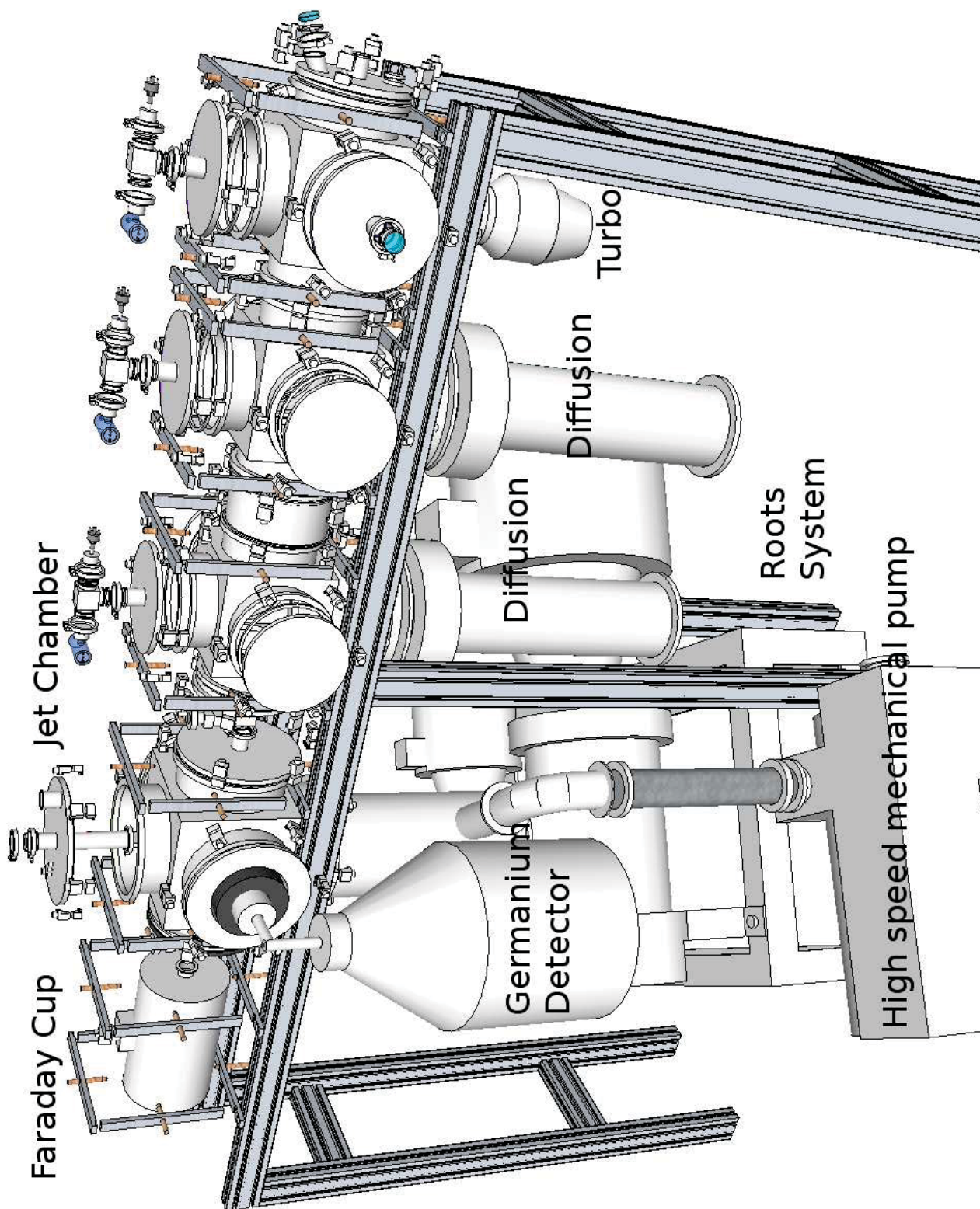


Figure 4.5: Beamline sketch - A close sketch to the final system.

The [differential pumping system](#) consists of one [turbo pump](#) (where the beam enters) of about 200 liters per second, and two [diffusion pumps](#) each of them of about a thousand liters per second.

The standard connection of most of the [differential pumping system](#) is LF200 that means that the aperture size of the aperture is around 8 inches.

An LF200 nipple had to be placed in between the consecutive diffusion chambers in order to be able to fit them together, since the bellies of the [diffusion pumps](#) were too wide.

The [scattering chamber](#) has only the first 2 stages. Notice that this chamber is connected to the [differential pumping system](#) through a QF40 valve. This allowed us to isolate completely the [scattering chamber](#) from the [differential pumping system](#).

Additionally flexible QF40 hoses were used in order to move, in a rather independent manner, this chamber.

Giving us the freedom to modify the experimental setup on the fly (in a manner of minutes), without having to let up the entire system up to air<sup>1</sup>.

The [germanium detector](#) was adapted through a modified LF250 flange (the nose), the main idea of the flange was to allow the germanium to be as close to the jet as possible, keeping in consideration the fact that it had to be outside of the vacuum system.

Another important aspect of the flange was to allow the possibility to accommodate shielding from external radiation around the Germanium detector. The aperture size of the LF250 (25 cm) gave us room for the detector and also for some lead shielding around it.

Notice that all the differential pumping chambers have two vacuum gauges on top. They have a thermocouple as a low vacuum gauge and an ion gauge as a high vacuum gauge they are connected to their respective chambers through a QF40 tee, that at the same time, is connected to a LF200 to QF40 adapter.

They are intended simply to monitor the system and allow us to know when the system is ready to be used, in case of leaks or malfunction of the system. These are our sources of information in this part of the system.

---

<sup>1</sup>It takes hours to acquire high vacuum in the [differential pumping system](#) if the starting condition was up to air.



## 4. EXPERIMENTAL METHODS

---

The blank flanges in the rest of the chambers can be used for, among other things, placing additional pumps in order to increase the pumping speed of the system.

Upgrading it, either to use other gases or to simply compactify the system, is done by removing differential pumping chambers and adding more powerful pumps in the remaining chambers. Being the keyword “modular”.

Also, in between the consecutive [diffusion pump](#) chambers, one of the inner walls is also shown. The QF40 adapter is also shown, a blank flange with small aperture is used<sup>1</sup>.

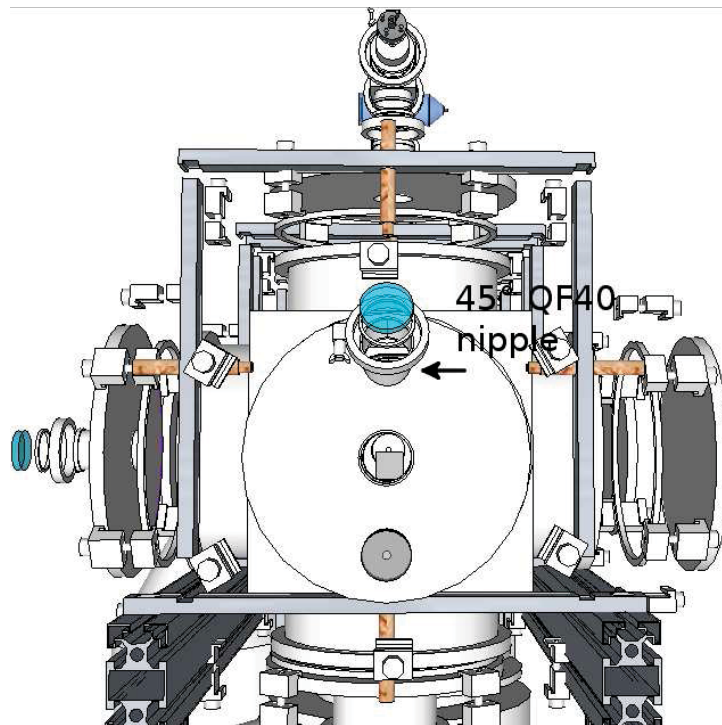


**Figure 4.6: Beamline front view** - The system seen from the entrance of the differential pumping system.

A great advantage of the design is that we can change the aperture size by simply changing the, relatively inexpensive, QF40 flange. Also, as it will be shown, it was paramount for aligning the [beamline](#) either optically as well as with the accelerators beam.

---

<sup>1</sup>The aperture we used was a 5mm in diameter circular aperture.



A front view of the system is shown in figure 4.6, the [chamber holder](#) can be better seen, in the center of the image one of the apertures can also be seen.

Additionally, a phosphor target is shown as a small rectangle inside the chamber, it is still not in the physical system, however it can and will be adapted in the future. It is intended for visualization of the beam as it enters the system.

The phosphor target is intended to be moved out of the way and in front of the beam through an external circular handle, shown in the bottom part of the flange, by simply rotating it.

In the same figure, above the entrance a [view port](#) at a 45° nipple viewport is shown, it is intended for viewing the glow of the phosphor target getting hit by the beam.

The side window in the turbo chamber, also shown in figure 4.5, is intended for better illumination of the phosphor target.

The table is made from [aluminum profiles](#), the base is 45 millimeters wide and 90 millimeters in height. Various table materials were also under evaluation, the traditional steel table was also under consideration. However, the lightness and strength of the [aluminum profile](#) had the edge.

Using [aluminum profile](#) seemed to be the best choice. They allow us to build quickly many types of tables, and basically the only requirement from the shop is a cutter.

Around halfway of the [beamline](#) the two central table legs were not originally considered. However while the system was being assembled the weight of the system was so great that the table deformed about a millimeter in the center.

The two central legs corrected this problem and the installation took only minutes. Of course the calculation time for the right size cuts and the cutting itself have to be considered.

This saves a lot of precious shop time. So it can be better used in making special vacuum, leak proof, pieces rather than tables.

Another important aspect is the rail the profiles have, they allow to slide and lock the system's vacuum chambers easily. As well as assembling the tables and they were proven very useful for the [chamber holder](#) as it was seen in figure 4.6.

A better view of the system is shown in the picture presented in figure 4.7. The [chamber holder](#) were designed to be as generic as possible and also to be as simple to construct as possible.

## 4. EXPERIMENTAL METHODS

---

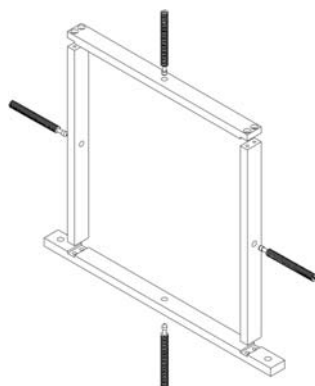


Figure 4.7: Chamber holder - Generic holder for the beamline.

The chamber holder consist of 4 aluminum pieces (two of them equal), 4 threaded brass pieces. And the bolts to put them together. The chamber holder took advantage of the rails of the table by making it easy to fasten them with the standard bolts that the tables use to get assembled. The holes on both sides of the chamber holder base are used for this purpose.

The table as well as the chamber holder were designed and built in terms of the size of the chambers and the height of the beamline.

## 4.2 The Built System

### 4.2.1 Overview

Figure 4.8 shows the finished system. A gas bottle is already connected to the system. The jet chamber is open and part of the nozzle and the catcher can be seem.

The last chamber was to be used as an extra pumping stage in order to lower the pressure enough for a Faraday cup. However during the experiment we simply connected the Faraday cup directly to the jet chamber, the photograph does not show the Faraday cup since it was removed to be used somewhere else in the laboratory.

Notice that the turbo pump and the diffusion chambers are a bit tilted, this was due an earthquake. Since the whole system was already aligned, the chamber holder were already tightened, the system twisted around the central axis where the beam goes through.



**Figure 4.8: Finished line** - A photograph showing the finished beamline for the supersonic gas jet target.

The beam did go all the way through almost perfectly, when tested afterwards. At the bottom to the left, in the table right before the aluminum one, we have the cooling system for the diffusion pumps. It consists of simply water, the water goes through hoses into the diffusion pumps, where the water spirals in the outside walls of them and recirculates back to the cooling reservoir.

The diffusion pumps have additionally another system, at their top, it is simply a cold section, cooled either with liquid Nitrogen or simply a special refrigerator. They improve the pumping speed however the system worked fine without them.

Notice, also in figure 4.8, that not all of the thermocouple and ion gauges are connected. This was due to the lack of controllers. However we can switch between the different gauges and measure the pressure one at a time.

The concentric pipes are also in place for the roots system, and starting from the exit of the pipe, we again used standard vacuum pieces. This time they were LF100, that is 4 inches in aperture sizes.

We used one 90 degree elbow, one nipple<sup>1</sup>, and two flexible nipples (one short and one long).

---

<sup>1</sup>Basically for increasing the distance between the Roots system and the mechanical pump.

## 4. EXPERIMENTAL METHODS

---

The long nipple connects directly to the high speed mechanical pump, it isolates much of the vibration. The short one connects directly to the exit of the [concentric pipes](#) and it is basically for ease of connection.

A noticeable change between the design, in figure 4.5, and the final version, in figure 4.8, is the orientation of the mechanical pump, and therefore also the [concentric pipes](#). The reason for the change was that the mechanical backing pumps of the [differential pumping system](#) got the opposite side of the line too crowded.



**Figure 4.9: Transitory Connection** - A pipe that will be replaced for a LF250 flexible nipple.

In figure 4.9 a transitory adapter between the jet chamber and the [concentric pipes](#) is shown.

It is worth mentioning that the [scattering chamber](#) was previously aligned. And afterwards the [concentric pipes](#) were aligned, with respect the jet chamber, while attached rigidly to the 1.5 ton Roots system!

Notice that in figure 4.9 there are no [clamps](#), the [concentric pipes](#) were supported all the way down from the roots system. This was one of the trickiest parts of the alignment<sup>1</sup>, and it was done with an error of the order of millimeters<sup>2</sup>.

---

<sup>1</sup>The flexible nipple was hard to find, by the time I got the quote, the funds were already spent.

<sup>2</sup>This will be improved once the flexible LF250 nipple is acquired.

### 4.2.2 The Train



**Figure 4.10: The Train** - Right after the beam selector magnet and before the differential pumping system. It consists on a quadrupole magnet, slits, a beam profile monitor and a Faraday cup.

In between the differential pumping system and the beam selector magnet, another section was added to the beamline we call this section the train, see figure 4.10.

This section is for controlling better the beam (through the quadrupole magnet and the slits), and monitoring it better (beam profile monitor and Faraday cup).

This section is important since it helps us optimize the beam before the differential pumping system, where due to the walls, a lot of the beam tends to get blocked.

Notice that part of the train is also held by the generic chamber holder we used for the chambers.

A steel table was used for the train, instead of the aluminum ones, mainly because the table was already made. However the height was not enough for the beamline, leg extensions were put on place and welded to the table to correct this problem.

### 4.2.3 Power Facility

The entire system required a brand new electrical installation so the laboratory could power up the required pumping system for the jet.

## 4. EXPERIMENTAL METHODS

---



**Figure 4.11: Power Facility** - An image of part of the new electrical system to power the supersonic jet beamline.

In figure 4.11 an image of part of the new electrical installation is shown. It is able to power up all of the pumps used in the system. That is :

- all mechanical backing pumps.
- the [diffusion pumps](#).
- [turbo pump](#).
- Roots system.
- high speed mechanical pump.

The pumps have to be turned on in a certain sequence in order to get the system running. However, as mentioned before, the jet chamber and the [differential pumping system](#) are isolated through a valve. This allow us to operate the two sections independently when the valve is closed.

Thanks to the electrical system the most of the jet line can be controlled via push-off buttons. Simplifying much of the operation of the system.

### 4.2.4 The concentric pipes

Even though the design was greatly simplified, the [concentric pipes](#) section was always present in every design. In figure 4.12 the piece can be appreciated from different perspectives.



**Figure 4.12:** The concentric pipes - Seen from different perspectives.

The picture from the left in figure 4.12, shows the **concentric pipes** seen from the side, the transitory piece as well as the LF100 90 degree elbow and the flexible hose are presented.

The picture from the left, in the same figure, shows the **concentric pipes** from the top. From here 2 unmentioned aspects of the pipes are shown:

1. Three centering bars support the inner pipe with the outer.
2. The central pipe has also a LF100 connection from the inside.

The first aspect was designed while the piece was still under construction. It is meant for greater stability and it also corrected small imperfections in the angle of the central pipe. These imperfections were due to the welding process.

The second aspect was intended for a movable, and potentially a replaceable, piece. Since it corresponds to the movable catcher shown in figure 4.13.

The catcher attaches to the **concentric pipes** with a standard LF100 connection, it is only needed the respective centering ring assembly and 3 **clamps** for tightening them together<sup>1</sup> shown in the bottom of the picture.

The LF100 connection was made from a blank flange where a hole with an internal thread was done. A pipe (with external threads) was placed through the hole. This

<sup>1</sup>The **clamps** can't be too tight or else the catcher won't move.



## 4. EXPERIMENTAL METHODS

---



**Figure 4.13: The catcher** - Shows the adjustable height jet catcher and the scattering chamber.

was the second machined piece since in the original design we intended to use fine threading<sup>1</sup>.

The design allows us to replace the catcher diameter without the need to replace the [concentric pipes](#). More capricious catcher shapes can be used.

A special centering ring assembly was placed before each of the pump apertures (the mechanical and the roots), in order to prevent large solid pieces from falling into the pumps.

### 4.2.5 Introducing The Roots System

The Roots system is an amazing piece of machinery. It pumps in the intermediate flow range faster than any mechanical pump<sup>2</sup>. And it is optimal for the pressure maintained in the surrounding region of the jet.

---

<sup>1</sup> The piece was left unusable once it was finished and fitted to the female thread, both pieces got permanently stuck.

<sup>2</sup>The cryogenic pump can pump very fast in this flow regime, however it gets saturated quickly since it does not expel the gas.



Images of it have already been shown in figure 4.8, multiple technical problems had to be solved regarding this system just to get it working. It has already been mentioned that an electrical system was made and that the alignment was tricky. Another problem that had to be solved on the fly was simply to get the 1.5 ton system inside the laboratory.

The laboratory lacked of a crane and the proper height in the undocking area for the truck in order to unload the system's box. After careful evaluation it was concluded that the quickest (and cheapest) way of introducing the equipment to the laboratory was to build a special cart for it.

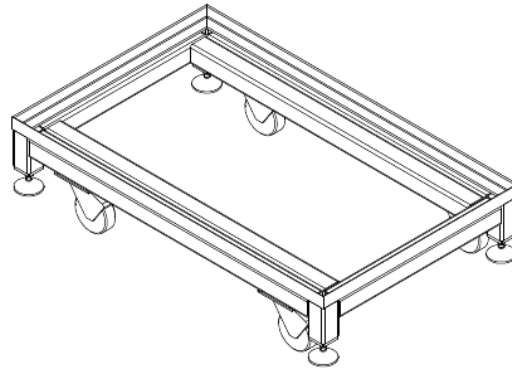


**Figure 4.14: Roots Cart** - Needed for getting the Roots pumping system inside the laboratory.

Figure 4.14 shows the design for the cart. The cart was made from steel, robust enough for the equipment, four wheels were used for mobility<sup>1</sup>, two of them with brakes.

In the four corners, lifters were placed<sup>2</sup>. They were used in order for the system not to be held by the wheels all the time, the system could simply rest on the lifters after moving.

### 4.2.6 The Nozzle

The **nozzle** is effectively the controlled leak aperture on how the gas enters the **scattering chamber**. The dimensions of the **nozzle** helps us estimate the properties of the gas flow into the chamber. Figure 4.15 shows a sketch of the **nozzle** dimensions.

---

<sup>1</sup>The intention was to literally roll the system into the lab.

<sup>2</sup>They came with the equipment so they could be attached to the metal frame.

#### 4. EXPERIMENTAL METHODS

---

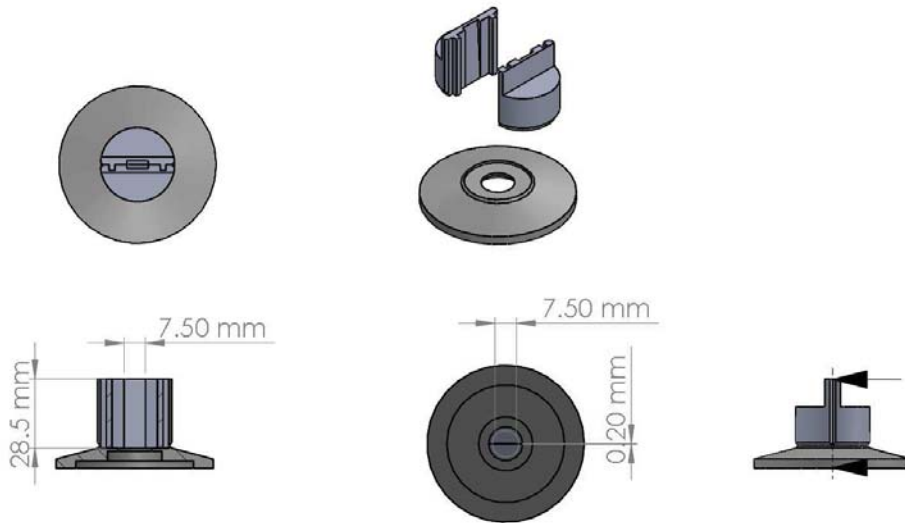


**Figure 4.15: Nozzle Dimensions** - Construction sketches of the nozzle pieces with dimensions.

The **nozzle** areas and the **nozzle** area ratio gives us the amount of gas **throughput** and an estimate of the expected Mach speed. In chapter 3 this was calculated and from figure 4.15 one can infer which are the required **nozzle** parameters (see figure 3.5) for this calculation.

As it was shown in figure 4.15, the **nozzle** was rectangular and the only change in size between the entrance of the **nozzle** and the exit was the height of the rectangle<sup>1</sup>. This made the construction of the **nozzle** relatively simple.

In order to get the desired **nozzle** dimensions, the orifice of the **nozzle** was made from 2 identical parts fitted together. On each half part of the material was scraped at an angle with a milling machine.

A third part was also built for adapting the **nozzle** to the rest of the system. It was a QF40 adapter, and it was attached and welded to the **nozzle** parts once they were also welded together.

The standard QF40 connection was also used for this case for the ease and quickness that it provides. However this time it was not used for vacuum but for handling

---

<sup>1</sup>Future **nozzle** designs change both height and width.

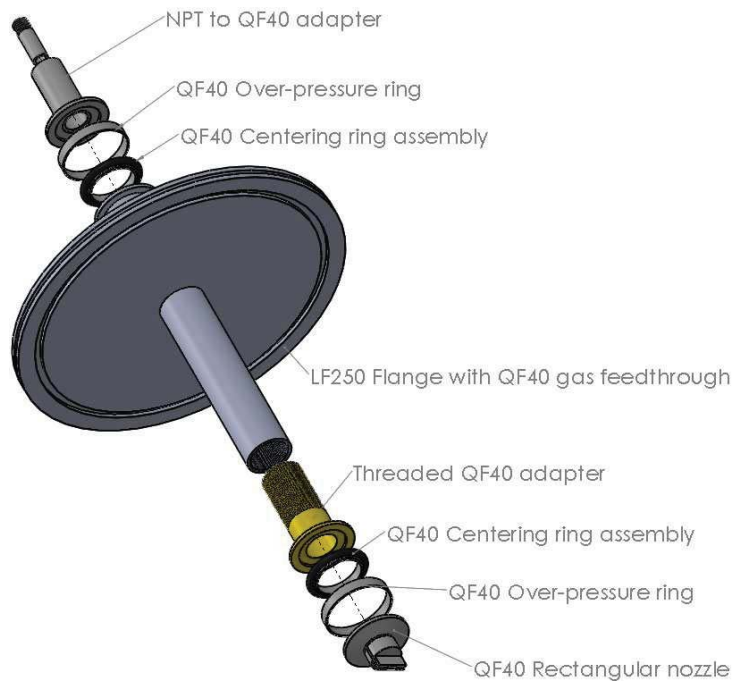


**Figure 4.16: Nozzle System** - Shows the nozzle system components.

“negative pressures”. That is, having pressures higher on the inside of the piece than from the outside.

Being a standard developed for vacuum systems it prevents, very effectively, gas from flowing inside the vacuum chamber. But when the pressure is “negative” the O-ring from the centering ring assembly gets blown out, generating unintended additional leaks from the side of the [nozzle](#).

This problem was corrected by placing an over pressure ring. The piece prevents the O-ring from blowing out and thus preventing these lateral leaks.

A circular [nozzle](#) was also constructed, it was a 1.5mm straight tube<sup>1</sup>. The construction for this [nozzle](#) was simpler, simply to drill a straight hole. Despite conventional theory, the straight tube circular [nozzle](#) did present [shock](#) patterns, typical of supersonic flow.

<sup>1</sup>It was latter modified so that the exit area increased to two millimeters.

## 4. EXPERIMENTAL METHODS

---

### 4.2.7 The Beamline Alignment And Inner Walls

As mentioned before, in order for the [differential pumping system](#) to be able to gradually reduce the pressure from the [scattering chamber](#) to the accelerator, inner walls with small apertures were used in between each chamber.

They helped to limit the gas [throughput](#) between each chamber while allowing the accelerator's beam to go all the way through to the jet chamber.



**Figure 4.17: Inner Wall** - A wall with a QF40 adapter was placed in between the differential pumping chambers. For placing QF40 blank flanges with small apertures.

Figure 4.17 shows a picture of how this is seen. In the picture a [view port](#) is instead of the QF40 blank flange with a hole. This was done with the intention of aligning with the beam by literally looking at it and moving the chambers in accordance so that the beam goes through the center of the [view port](#).

The beam alignment was preceded by an optical alignment with a telescope and an alignment done through the electronics with the beam profile monitor located right before the [differential pumping system](#) in “the train”.

In figure 4.18, the accelerator's beam is shown through the [view port](#). The left image shows also damages to the [view port](#) previously done by the beam (near the beam region).

In the picture to the right the beam is seen through a 5mm diameter aperture placed in front of the [view port](#). This was not the blank flange, with a hole, that was finally placed there. It was actually a special centering ring assembly that was also



**Figure 4.18: The Beam** - Shows how part of how the alignment was made with the beam hitting the [view port](#) inside the differential pumping chambers. Left shows the beam, right shows the beam through a 5mm diameter hole.

used in the connection of the [differential pumping system](#) with the [scattering chamber](#).

The pure optical alignment would have failed and it would have been very difficult to find the beam without the [view ports](#), considering that the beam has to go through three 5mm apertures before it gets to the jet target<sup>1</sup>.

The alignment had to be done with the pumps attached to their respective chambers mainly because:

1. The weight of the pumps might move the chambers if placed after alignment.  
and
2. Depending on the part being aligned, the pumps had to be on.

Although it was convenient it added a serious weight problem when it came to moving the chambers with the holders<sup>2</sup>. Without mentioning the fact that the [diffusion pumps](#) heat up in order to function, making the task dangerous not only for the [beamline](#) alignment and vacuum but to the people aligning the [beamline](#).

The problem was solved by using a crane, that held the weight from the bottom of the [diffusion pump](#) (the part that heats up the most), unloading most of the weight from the [chamber holder](#) screws allowing us to perform fine adjustments by turning the screws more easily.

---

<sup>1</sup>One between the [turbo pump](#) and a diffusion, the next between the 2 [diffusion pumps](#) and the last one between a [diffusion pump](#) and the [scattering chamber](#).

<sup>2</sup>Via the brass screws.

## 4. EXPERIMENTAL METHODS

---

In order to align the roots system, the beam alignment was also tried. However given the huge load of the roots system, moving it with precision was a great challenge. The entire [beamline](#) was moved while trying to align the roots system and everything got misaligned.

The alignment of the last chamber was finally done optically, with the previous alignment of the differential pumping system re-done, while the roots system was detached. Afterwards the roots system was moved to the location of the [scattering chamber](#) without touching the [beamline](#). The system was then lifted with its threaded legs.

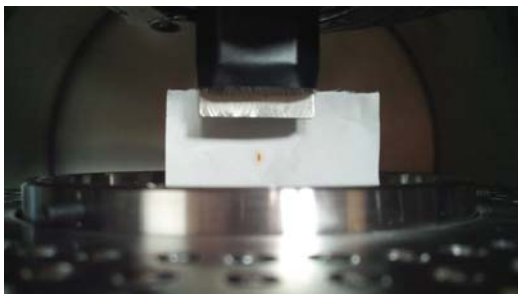


**Figure 4.19:** Bull's eye - Fax paper burned by the beam. This is inside the scattering chamber, the catcher is shown below and the nozzle is right above the burned mark.

To test the alignment we held fax paper to the nozzle, so that the beam burns it precisely where the beam goes through. Some minor adjustments had to be made to the lateral position of the [scattering chamber](#), these were done with the [chamber holder](#). The initial position was of about a couple of millimeters off and is was corrected. [Figure 4.19](#) shows the result of it.

The nozzle was then properly lowered so that the beam goes through right. Below the nozzle's exit.

### 4.2.8 The Experimental array

#### 4.2.8.1 Scattering chamber

This is the chamber where we are the most interested in. It is where the jet is, the chamber is big enough to host many charged particle detectors and, as it has already been mentioned, the flanges can be replaced to host up to two [germanium detectors](#).

Given the modularity of the design, the entire [scattering chamber](#) could be replaced for another one if the experiment requires it.



**Figure 4.20: Inside The Scattering Chamber** - Shows the [nozzle](#), the catcher, the detectors and their improvised holders.

Part of the inside of the [scattering chamber](#) is shown in figure 4.20. The [nozzle](#)'s height can be adjusted through a special brass piece.

The brass piece has on one side a Qf40 connector, for connecting to the [nozzle](#). And from the other side it is threaded<sup>1</sup>, allowing us to change the height and angle of the [nozzle](#).

The steel pipe, that connects to the brass piece, has evidently a female threading. It goes through the center of an LF250 flange, the connection in the outside part of the pipe is a standard QF40 flange.

The detector holders were improvised. They were stolen, literally, clothe hangers from my house. Cut and reshaped, they proved a good quick hack for the experiment.

For stability of the holders, masking tape was used.

### 4.2.8.2 Recent Updates

A newer addition was made to the experimental setup. It consisted in a steel plane surface. The idea is to provide a surface so that the [solid state detectors](#) could be placed and prevent them from moving.

Figure 4.21 left shows the new system as seen from the top. The steel surface is held from the catcher through the middle. It has 3 screws to hold it tight.

It also has holes all over it, so that the pumping speed is not considerably reduced<sup>2</sup>. They also, conveniently, serve as placing points for the plastics wrapping belts for holding the [solid state detectors](#).

---

<sup>1</sup>Nylon was used when connecting to the flange's pipe. Also, all the QF40 connections that were attached to the [nozzle](#) had over pressure rings.

<sup>2</sup>This was experimentally observed.

## 4. EXPERIMENTAL METHODS

---

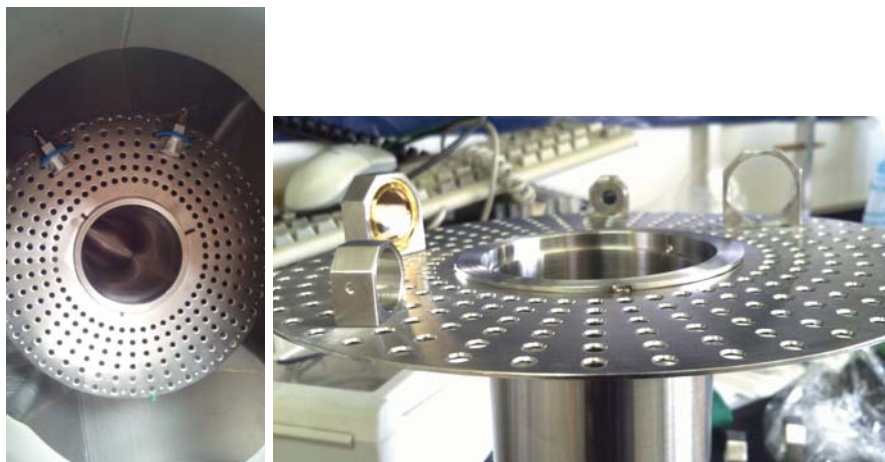


**Figure 4.21: Detector holders** - A newer more robust setup for the detectors.

It does have some inconveniences, the most important being that it does not allow to have the [germanium detector](#) placed. Since the steel surface gets in the way of the nose flanges.

In figure [4.21](#) right, the detector holders are also shown. They were made from stainless steel for 2 standard sizes. They keep the detector from inclining. In order to fasten a detector to its corresponding holder a lateral screw is tightened.

During the experiments, described in section [5.6](#), a 3 millimeter in diameter and 1 centimeter long collimator was placed in front of each detector.

### 4.2.8.3 EBS Setup

Tests of this experiment are shown in chapter [5](#) in sections [5.3](#), [5.4](#), [5.5](#), [5.5.1](#) an improved version of the experiment was finally made and it is shown in [5.6](#).

The experimental setup is shown in figures [4.20](#) and [4.22](#), where the rectangles represent the charged particle detectors.

Two solid state detectors, at the same angles relative to the beam, were used in order to have symmetric spectrums in each of them. This gives us good feedback on the data acquisition of the experiment. In case they are not symmetric, something is wrong.

During our experiments the expected symmetrical spectrums presented no asymmetry problems.



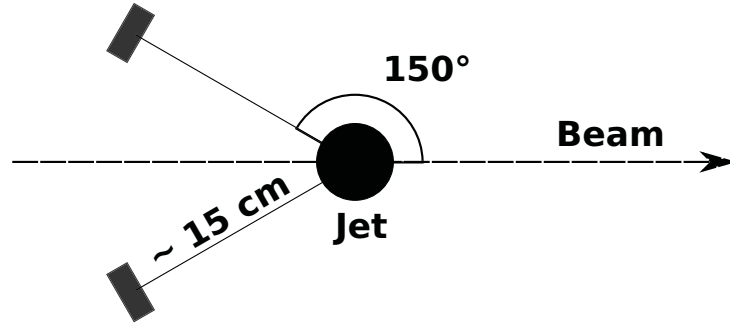


**Figure 4.22: EBS Setup** - The experimental setup for EBS seen from top.

The solid state detectors were connected to the outside of the [scattering chamber](#) via special QF40 standard connectors. Making the operation, of powering up the detectors and extracting the signals, very simple.

The QF40 feedthrough for the electrical signals for the detectors were additionally attached to QF40 flexible nipples in order to dampen the electrical noise generated by the vibration of the entire system (due to the pumps).

During the improvised setup, rotating the [nozzle](#) proved unpractical. Since the holders were directly attached to the brass part. Rotating the [nozzle](#) meant also rotating the detectors, changing the angle of the detectors with respect of the accelerator's beam.

The future formal setups, will make the [nozzle](#) movement independent of the detectors. Allowing us to experiment with the variable thickness property of the target, by rotating the [nozzle](#) and affecting the count-rate in the charged particle detectors.

#### 4.2.8.4 Germanium Detector Setup

Introductory theory of this is presented in section [3.3](#) and [3.3.2](#). The some data from the tests are shown in [5.5.2](#).

As mentioned before changing the experimental array to adapt a [germanium detector](#) is done by changing one (or both) of the side LF250 flanges.

## 4. EXPERIMENTAL METHODS

---



**Figure 4.23: Germanium Detector** - The experimental array with the germanium detector in place.

A picture of the [germanium detector](#), while an experiment is being performed, is shown in figure 4.23. The detector was placed as close as possible to the reaction zone, where the beam and jet meet.

Lead was used as shielding, it was used in the form of sea bags<sup>1</sup>. This allowed us to easily lift the shielding, one bag at a time, and also to tightly pack them surrounding the [germanium detector](#).

The nose flange was robust enough to handle the weight and, at the same time, not compromise the chamber's vacuum. As it can be seen from the picture, additional [clamps](#) were used to secure the flange.

Also in an improvised manner, a crane was used to lift the [germanium detector](#) to the proper height of the [beamline](#). It will eventually be replaced by a, proper height, table.

Much of the volume of the detector is taken by the cooling system, the liquid nitrogen Dewar. More modern [germanium detector](#) are much more portable and have an internal cooling system that does not require liquid nitrogen to be constantly refilled.

This could simplify the array, and the operation of the system, much more.

### 4.2.8.5 E- $\Delta$ E Telescopic detector array

The experimental array inside the scattering chamber is shown in figure 4.24. A 1 cm long 3 mm in diameter collimator was placed in front of a telescopic array of silicon detectors at 35° with respect to the beam. This long collimator stops particles produced

---

<sup>1</sup>Typically used by divers, they are bags filled with lead in a granular form.

by beam interactions with residual gas molecules in its path before or after the high density jet target.

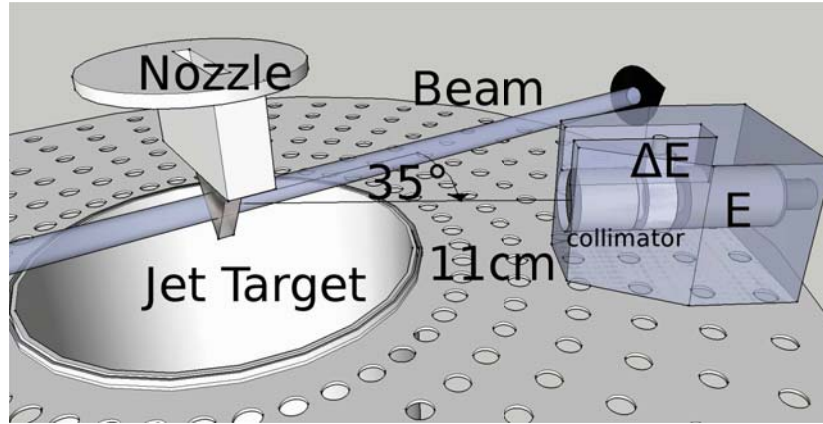


Figure 4.24: Telescopic array - The E- $\Delta E$  detector setup.

A very thin ORTEC planar detector ( $11\mu\text{m}$ , 9V) was used as “ $\Delta E$ ” and a thicker ( $300\mu\text{m}$ , 60V) CANBERRA PIPS detector as “E”. Light particles punch through the detector and, at these energies, stop in the E detector, allowing identification through the current  $E-\Delta E$  technique. Heavy ions are stopped by the detector no positive identification is possible, although some groups can be identified by its energy from kinematics. A standard triple alpha source ( $^{239}\text{Pu}$ ,  $^{241}\text{Am}$ ,  $^{244}\text{Cm}$ :  $E_\alpha = 5.15, 5.48$  and  $5.8$  MeV respectively) was used to calibrate in energy both elements of our telescope. The energy loss, in the “ $\Delta E$ ” detector, for each alpha was 2.55, 2.41 and 2.29 MeV respectively.

### 4.3 Optical Tests

Chapter 5 in section 5.2 presents the data obtained from this experimental setup.

The nozzles were subjected to a Schlieren experiment<sup>1</sup>. Schlieren is an experimental technique that allows us to visualize the flow. It uses the fact that the shocks, in the jet, present inhomogeneities in the flow. These are essentially differences in the local refractive index. Light transverses different optical paths and the technique helps contrast this, allowing to easily visualize the structure of the jet.

<sup>1</sup>Theory on this technique can be found in (48, 51)

## 4. EXPERIMENTAL METHODS

---

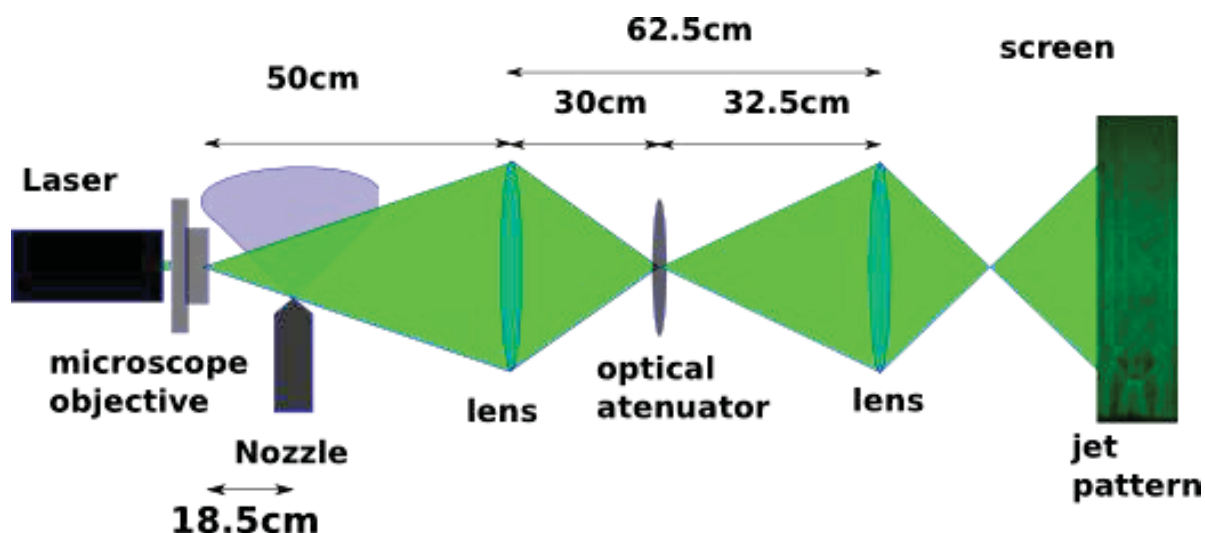


Figure 4.25: The Schlieren Setup - Optical array to visualize the jet.

Figure 4.25 shows the schematic of the array. Laser light is passed through a microscope objective, in order to broaden the light for the nozzle. Afterwards, the light passes through the jet flow of our nozzle.

Lenses are used to re-focus the light onto a screen and the attenuator helps to contrast the light, so that the shock patterns can be appreciated more easily in the screen.

In figure 4.26, the physical setup is shown. The assembly system for the nozzle is the same as the one shown in figure 4.16 without the LF250 central parts, additionally the circular nozzle was also used.

Arrangements have been made in order to perform the experiment inside the scattering chamber. LF250 flanges (already available) with QF40 adapters for view ports, can be placed in opposite sides of the scattering chamber while the jet is on.

The experiment will have to be moved to the Van de Graaff accelerator to perform the experiments<sup>1</sup>.

Previous tests with the QF40 view ports suggest that they won't pose much of a problem when performing the experiment, despite the fact that they may also distort the light because of their imperfect surface<sup>2</sup>.

---

<sup>1</sup>For obvious reasons.

<sup>2</sup>They may even replace the lenses needed for the Schlieren setup.



**Figure 4.26: The Schlieren Physical Setup** - Optical array to visualize the jet.

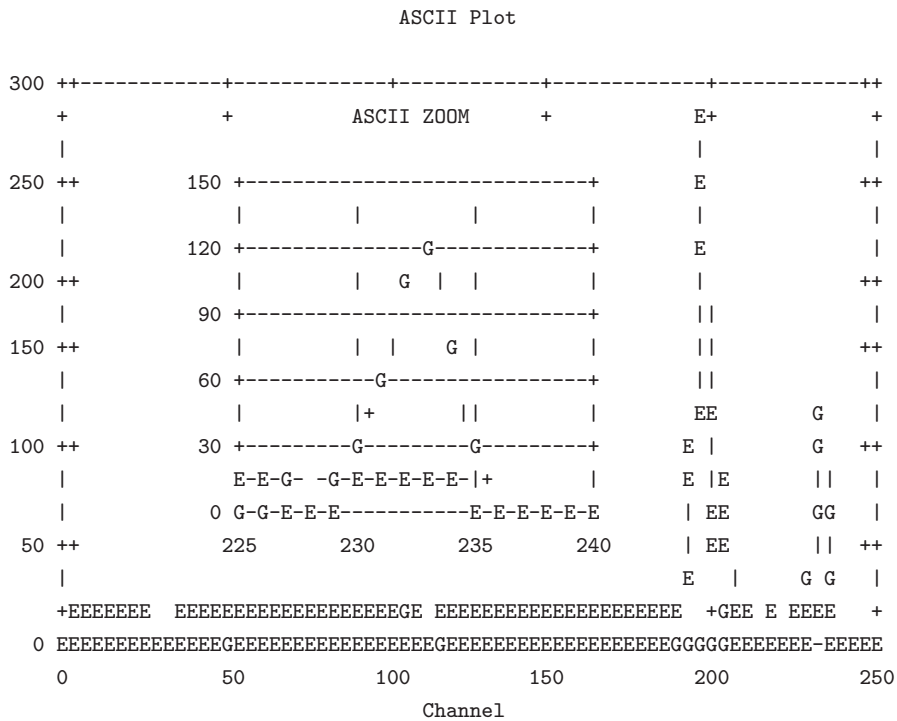
This will allow us to view and study the jet in, essentially, a vacuum environment. This extreme condition is interesting by itself for fluid experiments.

#### 4. EXPERIMENTAL METHODS

---

# 5

## Tests, results and discussion



“If you want to live a memorable life, you have to be the kind of person who remembers to remember.”

– *Joshua Foer*

2006 U.S. Memory champion.

## 5. TESTS, RESULTS AND DISCUSSION

### 5.1 Pump data

The first tests that were performed with the system were made for checking the that the available pumps performed as expected, and that the vacuum system did not have any leaks or unexpected problems.

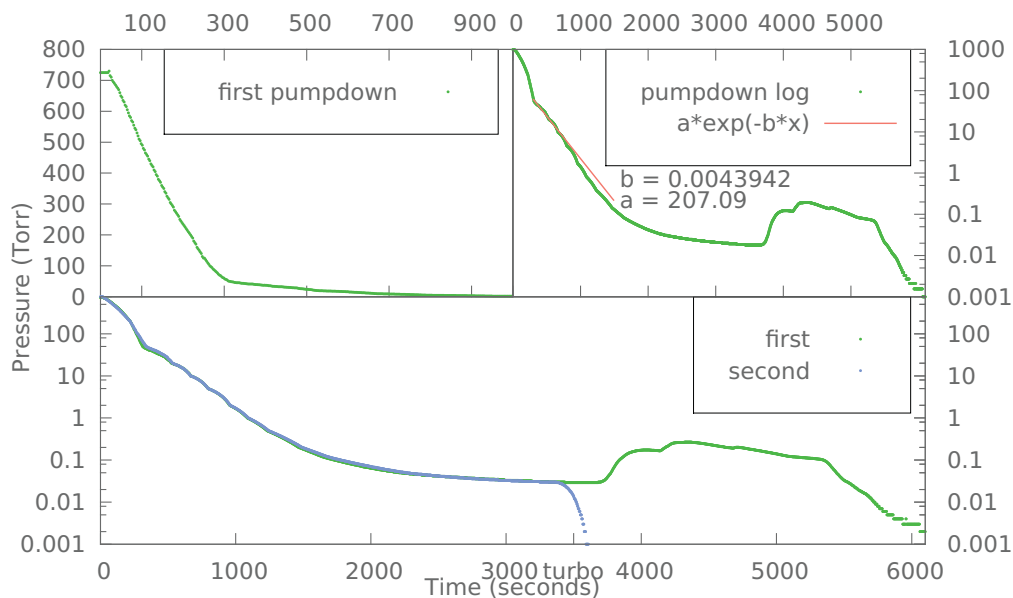


Figure 5.1: Turbo and mechanical data - Data from our pumps

In figure 5.1 the pumpdown of the first two chambers of the differential pumping system is shown, that is the turbo chamber and the diffusion chamber right next to it (see figures 4.5 or 4.8 for a better reference).

The pumpdown was performed from atmospheric pressure with the mechanical pump with the aperture, for the QF40 5mm aperture flange (figure 4.17 without the view port see also 4.18 for the aperture), open. The top left plot of figure 5.1 was the first pumpdown of the system.

As expected, the pressure in the chambers decreases as time increases, figure 5.1 top right shows the same data in logarithmic scale in pressure and over a longer period of time. It is important to notice that the pump-down curves are reproducible (almost identical). This indicates that the pumps and the system overall behavior is consistent.



The gauge that was used was a thermocouple. The performance, of this types of gauges, increases as the pressure decreases<sup>1</sup>. We notice that as the pressure decreases to less than 200 Torr, the pressure decrease behaves more or less as the expected exponential decreasing function, see section 3.4.2, the fitted values for the exponential decrease are also shown in the plot. This behavior continues for about 2 or 3 orders of magnitude.

Remembering equation 3.85 (from section 3.4.2):

$$P(t) = P_0 e^{-\frac{S}{V}t} \quad (3.85 \text{ revisited})$$

The fitted  $a$  value is the  $P_0$ , the point at which the exponential behavior was observed, around 200 Torr. The  $b$  value is simply  $S/V$ , we know  $S \approx 1$  liter/sec and the total volume to be pumped is around 130 liters<sup>2</sup> we have that:

$$\frac{1}{130} \approx 0.007$$

Which is more or less close to the fitted value  $b \approx 0.0043$ , the discrepancy would be expected to be reduced if we include in the pump down curve theory the conductance of the piping (take into account the shapes of the pumped volume).

As the pressure gets lower than 0.1 Torr, the flow regime of the gas enters the intermediate range, see section 3.4.1. The mean free path of the air molecules start to be of the order of the piping diameter (a few cm). Additionally the leak rate of the pump into the vacuum chamber can no longer be ignored.

A sudden burst in pressure of a few hundred mTorr is seen at about  $4k$  seconds, this is typical of “dirty systems”<sup>3</sup> numerous reasons for this can be given that go from grease deposited from human hands to literal dirt.

The turbo pump was then turned on, at about  $5.5k$  seconds, and the pressure went down at an even higher rate. The bottom part of figure 5.1 the initial pumpdown shown along a second test in the same system. The pumpdown curve was almost perfectly reproduced however this time, at about  $3.5k$  seconds, the **turbo pump** was turned on.

<sup>1</sup>At atmospheric pressure they usually gave a reading in between 760 Torr (too high given the altitude of Mexico city) and 500 Torr.

<sup>2</sup>The 2 chambers the attached pumps, diffusion turbo and their pipes not to mention the piping that connects to the accelerator etc.

<sup>3</sup>That is systems that have been without vacuum for a long time.

## 5. TESTS, RESULTS AND DISCUSSION

---

The **turbo pump** goes all the way down to  $10^{-7}$  Torr, but this is outside the range our thermocouple can measure<sup>1</sup>. Unfortunately, the gauge that can measure in this pressure regime lacked of a computer acquisition interface.

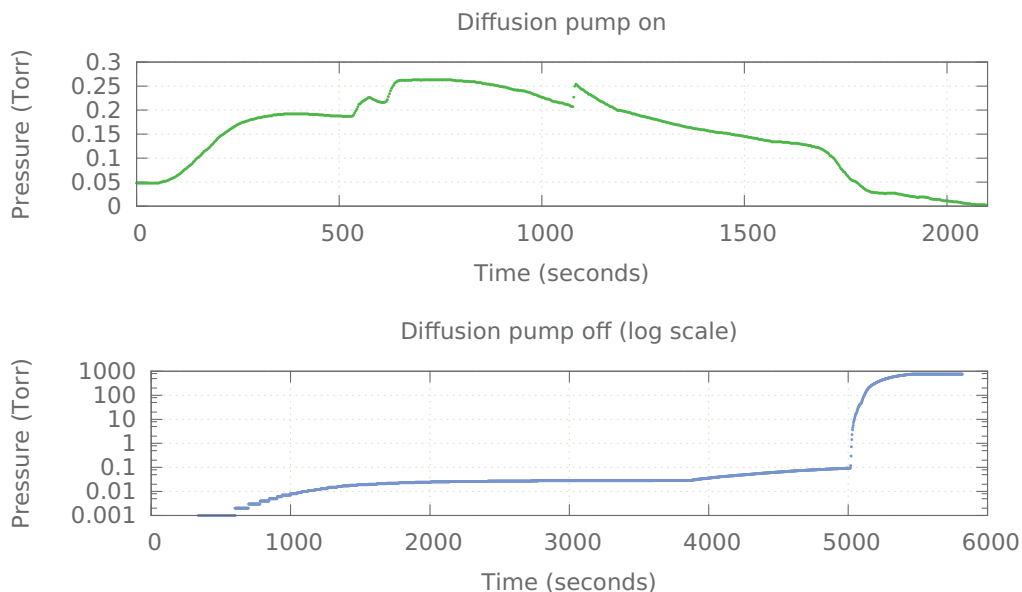


**Figure 5.2: Diffusion pump data - Diff data**

The **turbo pump**, pumps in the molecular flow regime. We would expect to have an even more perfect exponential decrease rate. However not at the beginning, since the **turbo pump** needs time to go from 0 rpm to about 25k rpm.

The middle chamber, in between the turbo and the other diffusion pump chambers, was isolated and pumped. Figure 5.2 shows the data taken.

The forepumping done by its respective mechanical pump is not shown, in the top side of figure 5.2 we are interested in the pressure fluctuations inside the chamber created when the diffusion pump is turned on<sup>2</sup>.

Note that it takes almost 2k seconds for the pressure to start lowering again. That is more than half an hour, in contrast of the turbo pump that started to act immediately.

---

<sup>1</sup>It can't go lower than mTorr.

<sup>2</sup>Note: there is no valve between the diffusion pump and the chamber, it would be convenient... but expensive. Also the cold trap of the diffusion pump is not used in any of our experiments.

This is important since we can estimate how long it would take us to make changes to the system, for example; aligning with the beam, as described in section 4.2.7.

The bottom plot of figure 5.2 shows a plot of the pressure increase after the pump has been turned off. It is incomplete due to the lack of interface between the computer and the low pressure gauge. Once the pressure gets back to the range the mechanical pump initially left, the diffusion pump is already cooled down and the system can be opened this happens in about 5k seconds or about 83 minutes. The plot illustrates the static pressure<sup>1</sup> behavior, even if the chamber is sealed shut. There will always be leaks, either from the outside or from the inside<sup>2</sup>. Vacuum pumps lower the pressure as long as the throughput of the pump is higher than the throughput of the leaks. Section 3.4.1 concerns of equilibrium conditions, equal pump and leak throughputs, but it gives some background in this.

The abrupt increase in pressure in the bottom plot of figure 5.2 is due an intentional venting of the system. The vacuum chamber was opened.

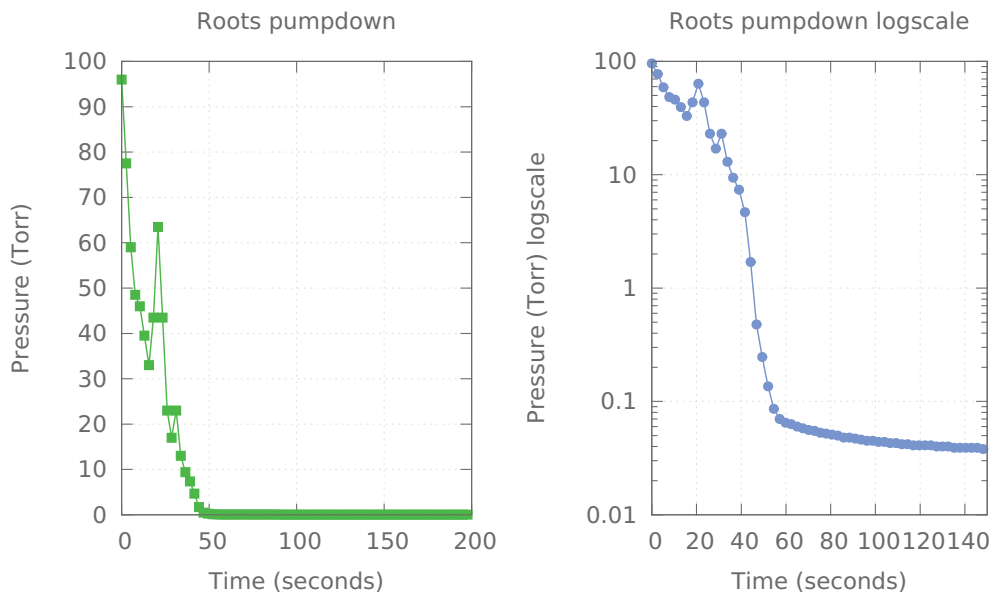


**Figure 5.3: Roots pumping - Data from the roots.**

Lastly, the [roots system](#) was tested, since it can start pumping at higher pressures

<sup>1</sup>Pumps off and mechanical pump sealed off by a valve.

<sup>2</sup>Sometimes called virtual leaks.

## 5. TESTS, RESULTS AND DISCUSSION

---

than the [turbo pump](#) or the [diffusion pump](#) can, the thermocouple can be used for pressure measurement and comparison.

However, even though the volume of the [scattering chamber](#) and its connector to the [roots system](#) (the [concentric pipes](#)) is considerably larger than the chambers in the [differential pumping system](#), the pressure drop was considerably larger. It reached its final pressure in a manner of seconds.

The [roots system](#) system consists of 3 pumps, a mechanical one, a medium sized roots and a large sized one. The pressure quickly dropped as the pumps were sequentially turned on. The plot shows two peaks, one where the medium sized roots was turned on and the other is when the large sized roots was turned on.

Table 5.1 shows a comparison between the measured pressure values and the estimated for the differential pumping system (see section 3.4.1).

Chamber	$P_{\text{estimated}}$ [Torr]	$P_{\text{measured}}$ [Torr]
Jet	0.1	0.115
D2	$8 \times 10^{-4}$	$2 \times 10^{-4}$
D1	$1.8 \times 10^{-6}$	$1 \times 10^{-5}$
T	$2 \times 10^{-8}$	$1.6 \times 10^{-6}$

**Table 5.1:** Estimated vs calculated pressures. In the different chambers.

In table 5.1 “T” represents the pressure in the turbo chamber, “D1” represents the pressure in the middle diffusion chamber, “D2” is the chamber with the diffusion pump that’s right next to the scattering chamber and finally “Jet” represents the pressure in the scattering chamber, it is not the pressure of the jet but the pressure of the surrounding region of the jet.

The  $Q_{\text{Leaks}}$  becomes important as the pressure is lowered, this also introduces more particles into the system as was mentioned in section 3.4.1. Nevertheless the throughput over estimation paid off in compensating the *leak throughput* allowing for the system to be connected to the accelerator, by having a pressure lower than the accelerator itself ( $\approx 5 \times 10^{-6}$  Torr), making the accelerator an additional leak source for the turbo chamber<sup>1</sup>.

---

<sup>1</sup>Also worth mentioning is that the cold traps of the diffusion pumps was not used.

## 5.2 Schlieren Tests

The experimental array for the Schlieren experiment was shown in figures 4.25 and 4.26 in section 4.3. The experiment was performed before the entire beamline was built.

Confidence and valuable experience were obtained from this first familiarization of the phenomena.

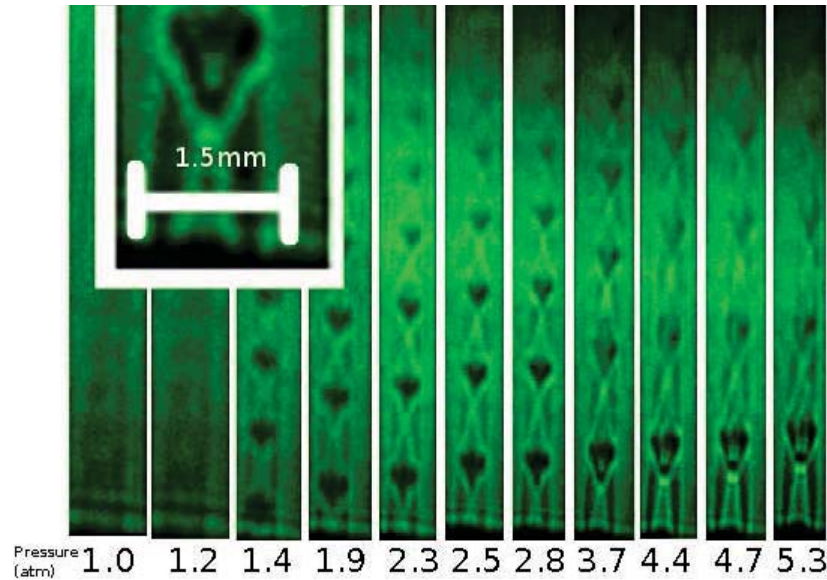


Figure 5.4: Supersonic flow - Air flow from one of our nozzles

Figure 5.4 shows the shock patterns of the air jet, from flow through the circular nozzle, at various pressures. The pictures were taken with a high resolution camera in the screen shown at the top right corner of figure 4.26.

The Mach number can be obtained from the angle defined in the shock patterns through equation (3.33), where the angle  $\alpha$  is the small angle in the shock region (Figure 5.4). We were able to measure the Mach number through these angles off the X patterns in the images giving:  $M = 2.1 \pm 14\%$ ,  $2.4 \pm 13\%$ ,  $2.8 \pm 12\%$  for pressures  $p = 2.5, 2.8, 3.7$  atm, respectively.

In the leftmost two images of Figure 5.4, the inlet to exit pressure ratios are not high enough to produce shock patterns. In the rightmost three photographs (the highest pressures), the pressure differences are too big, thus we are unable to determine the Mach number following the same procedure. Figure 5.4 also shows (in (b)) the typical

## 5. TESTS, RESULTS AND DISCUSSION

---

structure of supersonic flows; even though the gas is moving fast, the patterns remain stationary. And such patterns occur multiple times downstream.

The exit pressure of the flow is atmospheric pressure. That is why no patterns emerge from the first picture (counting from left to right), the critical ratio for supersonic flow has not been satisfied.

Remembering the result from equation 3.68, the critical pressure ratio for nitrogen<sup>1</sup> is:

$$r_c = 0.525 \quad (3.68 \text{ revisited})$$

This means that around two atmospheres ( $\approx 1.9$ ) the *shock* patterns should start to emerge. In figure 5.4 the 1.9 atmosphere picture does start to show the first *Mach* disk, the “*tongue*”.

There are two important observations to be made:

1. *Shock* patterns emerge with a straight tube *nozzle*.
2. The height of the “*tongue*” increases with the pressure.

Observation 1 conflicts with equation 3.32d (see also figure 3.4) :

$$\frac{A}{A'} = \frac{1}{M} \left[ \frac{1 + \frac{\gamma-1}{2} M^2}{\frac{\gamma+1}{2}} \right]^{\frac{\gamma+1}{2(\gamma-1)}} \quad (3.32d \text{ revisited})$$

Notice that for a straight *nozzle* the area ratio is exactly one, which invariantly implies that the *Mach* must also be one ( $M = 1$ ). Remembering equation 3.47, see also figure 3.5:

$$\mu = \frac{\pi}{2} - \tan^{-1} \sqrt{M^2 - 1} \quad (3.47 \text{ revisited})$$

We have that the second member vanishes making:

$$\mu = \frac{\pi}{2}$$

Just by comparing the patterns in figure 5.4 with the expected  $\mu$  angle in figure 3.5 one notices that they do not match up.

---

<sup>1</sup>Air is mostly nitrogen.

This behavior may be due to imperfections in the **nozzle**. Making the cross sectional area throughout the **nozzle** change, that resulting in a **Mach** greater than one and therefore the **shock** patterns emerge.

Observation 2 is also important since conventional theory leads us to believe that it does not depend on the inlet pressure. Remembering equation 3.49 we have:

$$e = \frac{d}{2} \tan \left( \frac{\pi}{2} - \mu + \frac{\alpha}{2} \right) \quad (3.49 \text{ revisited})$$

From figure 3.5  $e$  is the tongue height,  $d$  is the exit length (in our case, the diameter),  $\alpha$  is the opening angle from the **nozzle's** aperture and  $\mu$  is the angle between the tongue and the **nozzle's** opening surface.

As we just saw,  $\mu$  depends on the **Mach** speed and the area ratio. All the mentioned parameters do not depend in the inlet pressure. Therefore, as the previous equation states, the height should not change as the pressure increases.

However, as it can be shown if figure 5.4, this is not the case. The height of the tongue in terms of the intake pressure is shown in figure 5.5. Hatanaka (52) has similar results.

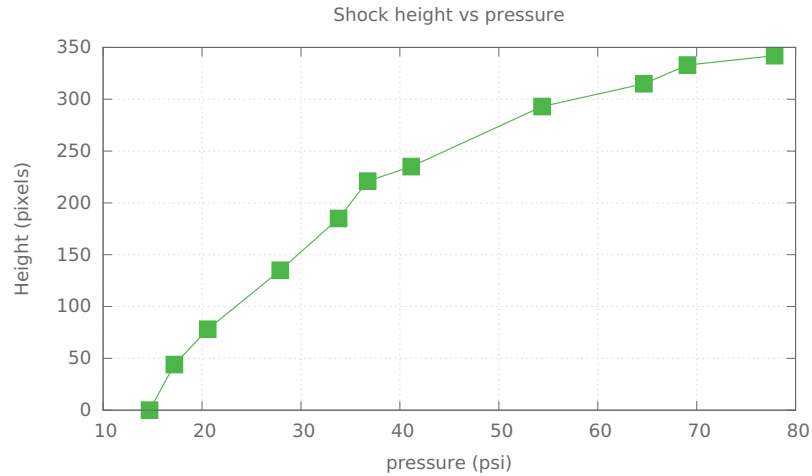


**Figure 5.5: Tongue Height** - Plot of the tongue height in terms of the inlet pressure measured from the gas bottle.

There are also interesting propositions in how to measure the speed of the flow directly (not just theoretically as in chapter 3). Moosmüller presents a technique for

## 5. TESTS, RESULTS AND DISCUSSION

---

measuring the speed of the flow from a supersonic Nitrogen jet using inverse Raman spectroscopy (53).

This is of interest since the Raman technique involves light, typically lasers. View port could be used to see through the scattering chamber the LF250 flanges could be modified relatively quick to adapt more view ports.

### 5.2.1 Rectangular Nozzle Schlieren

The rectangular nozzle did not present the shock patterns, in the Schlieren experiment, as in the case with the circular one. We believe that the shock occurred inside the nozzle and by the time the flow came out of the nozzle there were no more shocks.

Remembering equation 3.38, which gives us the number of molecules per unit volume for the jet flow, we have:

$$\frac{n}{n_0} = \left[ 1 + \frac{\gamma - 1}{2} M^2 \right]^{\frac{-1}{\gamma - 1}} \quad (5.1)$$

With the Mach speed of  $M \approx 4$  and specific heat ratio of  $\gamma = 1.4$  we have that :

$$\implies \frac{n}{n_0} \approx 10^{-2}$$

So even if the molecular density of the gas before the nozzle ( $n_0$ ) is 2, 3, or four times the atmospheric density. The molecular density of the exit flow ( $n$ ) is lower than the atmospheric density. Making the surrounding molecular density much higher than the jet, which is not typical and probably a sufficient condition for not having shocks outside the nozzle.

However we believe that somewhere in the inside of the nozzle there is a “break-down” of the shocks. All this while the density of the flow, inside the nozzle, is higher than the surrounding atmospheric density simply because of this extreme over expansion. Shocks in a simple rectangular opening were observed and the pattern is shown in figure 4.25.



## 5.3 EBS tests

### 5.3.1 EBS with air

We used the EBS setup as shown in figures 4.20 and 4.22. Two solid state detectors were placed at 150 degrees, relative to the beam direction, to detect backscattered particles.

As in the case of the Jet-Beam photograph experiment, the nozzle's valve was simply opened to let the laboratory's air through.

In figure 5.6 the data from the first EBS experiment is shown. The target was an air jet and the used beam was 2.8MeV protons. We were able to identify the various elements by their respective peaks, being the most representative the nitrogen and the Oxygen peaks.

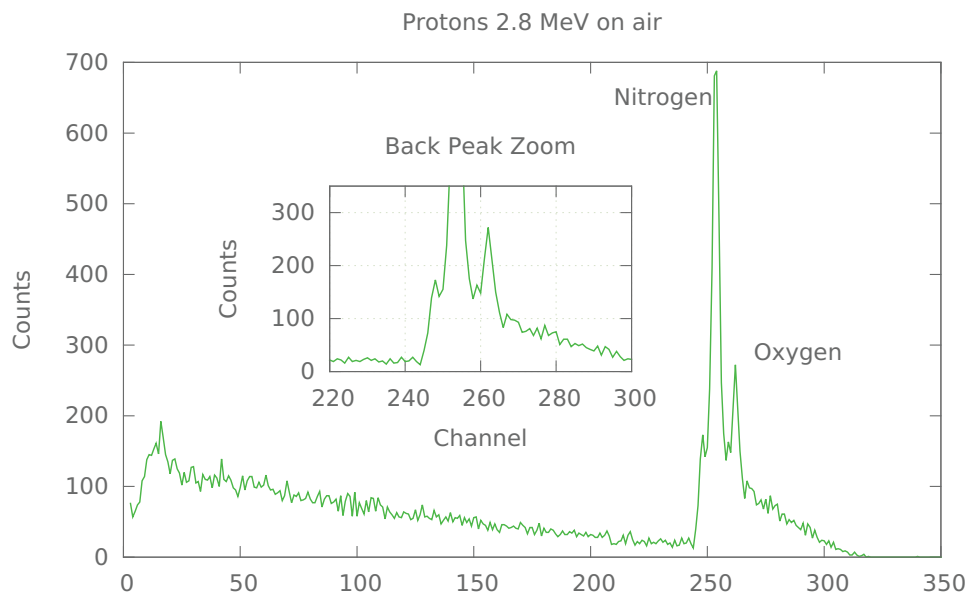


**Figure 5.6: Nitrogen and Oxygen** - Peaks from the EBS experiment from 2.8MeV protons with an air jet target.

There are a couple of observations that stand out immediately:

1. There is a background.

## 5. TESTS, RESULTS AND DISCUSSION

---

2. There are back peaks that are respectively behind the Nitrogen and Oxygen peaks.

Observation 1 is important since in principle there should be counts only in the channels that correspond to the components of air, having well defined peaks for each one. Not an energy<sup>1</sup> spread as shown in figure 5.6.

The background problem has been encountered by other authors (36), they have dealt with the problem by optimizing the jet changing many parameters, such as nozzle temperature and pressure.

Beam interaction with the low pressure residual gas left in the target chamber around the jet will scatter particles into the detectors from every point along its track, before and after the jet, producing the background present in figure 5.6. Significant background reduction is achieved by the introduction of collimators in front of the detectors (see section 5.6).

A closer look to the backpeaks is also shown in figure 5.6. At this point the nature of such backpeaks remains unclear. As it will be seen they are not present in every experiment and disappear when the collimators were placed. We speculate they may correspond to beam scattered by an unidentified target, solid and distant, and depend on the focusing details of the beam.

The height of the back peaks do not scale linearly with their respective main peaks, although there is a decrease in height of the Oxygen backpeak with respect the Nitrogen one.

Peak Name	Channel	Count
Nitrogen	254	688
Nitrogen backpeak	248	173
Oxygen	262	272
Oxygen backpeak	259	163

**Table 5.2:** Channel and height (count number) of the various peaks.

Table 5.2 shows the channels and heights of the peaks shown in figure 5.6. From size of the Nitrogen and Oxygen peaks we can infer the relative abundance of them in air.

---

<sup>1</sup>There is a linear relationship between the energy and the channels.

This of course ignores the fact that there are more components in air such as Argon and that we should integrate the counts over the peaks, the cross sections etcetera. Better data was produced latter worth a more detailed analysis. However, at this stage it was interesting to try a quick “back of the envelope” estimation:

The total count number is:

$$T_{\text{count}} = N_{\text{count}} + O_{\text{count}} = 688 + 272 = 960 \quad (5.2)$$

So we get for Nitrogen:

$$N_{\%} = \frac{N_{\text{count}}}{T_{\text{count}}} \approx 71\% \quad (5.3)$$

We therefore get for Oxygen:

$$O_{\%} \approx 29\% \quad (5.4)$$

The reported percentages at sea level are:

- Nitrogen 78.084%
- Oxygen 20.9476%

In section 5.6.1 the experiments were repeated and the analysis was properly done using SIMNRA. Se table 5.5 for a better reference.

## 5.4 Tests with Nitrogen

Our next experiment was done with nitrogen from a high pressure bottle as a target (at 1.5 bars) and a 1.3 MeV protons beam. The gas pressure is measured all the way back in the bottle, and not right behind the nozzle, as it would be the ideal case. This was done for the sake of simplicity. This is an obvious improvement for future setups.

Also, over pressure rings had to be placed on the outside of the chamber, in the connection of the gas bottle to the valve and from the valve to the scattering chamber, since the pressure in those sections could be higher than atmospheric pressure.

As in the case with air, we notice that there are counts in the channels surrounding the main peak. There is no back peak as in the case with air. This is close to what we would expect from a standard EBS experiment.

## 5. TESTS, RESULTS AND DISCUSSION

---

As it has the name suggests, the bottle pressure is measured all the way back in the bottle, and not right behind the [nozzle](#), as it would be the ideal case. This was done for the sake of practicality, however this is a an obvious improvement for a near future.

Also, the over pressure rings had to be placed also on the outside of the chamber. In the connection of the gas bottle to the valve and from the valve to the [scattering chamber](#), since the pressure in those sections was sometimes higher than atmospheric pressure.

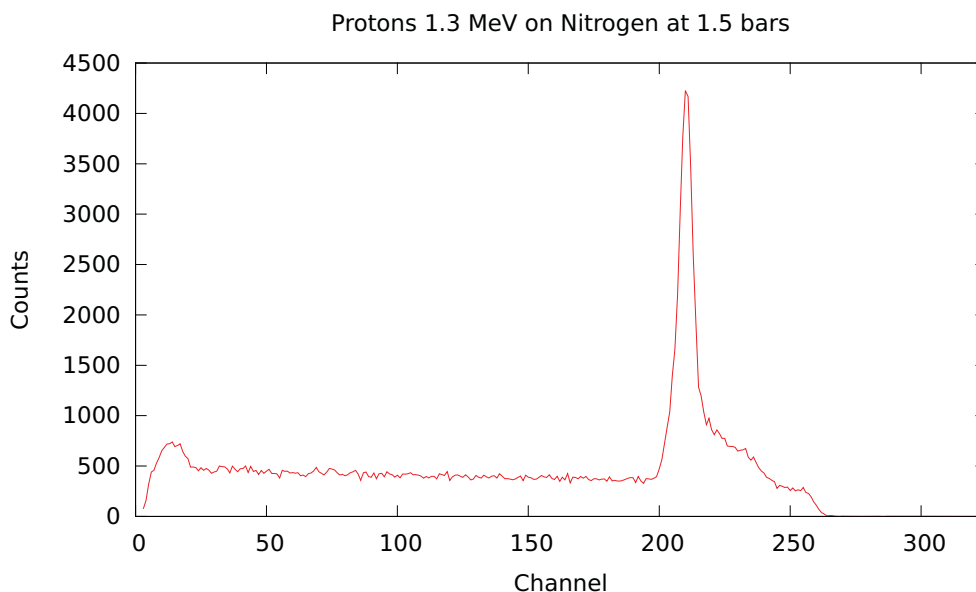


**Figure 5.7: Protons in Nitrogen - EBS** data from 1.3MeV protons in Nitrogen at 1.5 bar.

In figure 5.7, the Nitrogen peak is shown to be around [channel](#) 220. We no longer see the [Oxygen](#) peak, as expected. As a simple observation, the Nitrogen back peak did not emerge.

Figure 5.8 shows the [EBS](#) data from a 2.8 MeV proton beam on Nitrogen at 2 different pressure readings from the bottle: 3.5 and 4.5 bar. A third spectrum correspond to data taken with no jet. From the 3.5 and 4.5 bar experiments we can observe that:

- The main Nitrogen peak is well defined.

- The background, while is still non zero, it is well below the count rate of the main peak.
- A back peak can be shown in this case also (barely).

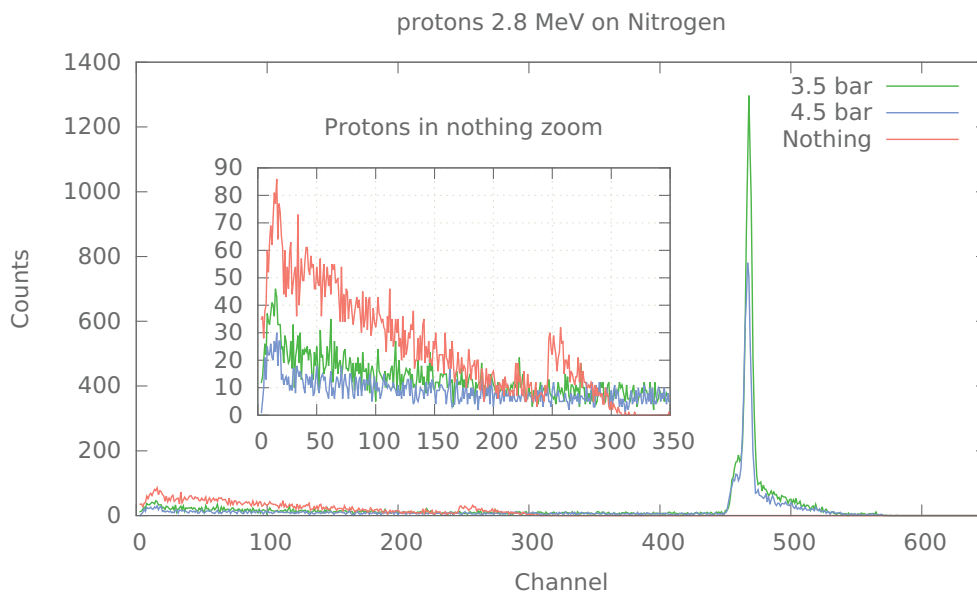


**Figure 5.8: 2.8 MeV protons in Nitrogen** - Various conditions in 2.8 MeV protons. The plot without jet (the “nothing” plot) took 4 times longer than the others.

Figure 5.8 shows the EBS data from the experiment. The respective proton energy for the projectile in this case is 2.8 MeV, we used in this case Nitrogen at 3 different conditions, 3.5 and 4.5 bar in the bottle’s pressure reading and finally a no jet experiment.

When we increased the bottle pressure to 4.5 bar, figure 5.8. We noticed that the plot was qualitatively the same. However, since the bottle pressure was increased the target density was increased, we expected the count rate to increase and this was not the case, the count rate actually decreased as can be seen in the figure.

Another experiment was done without the jet, with the pressure in the scattering chamber a bit lower than what we had previously worked with the jet, with 2.8MeV protons. The spectrum is also shown in figure 5.8 with a zoomed region. Data was taken with the same beam and no jet. The spectrum is shown in figure 5.8. The data

## 5. TESTS, RESULTS AND DISCUSSION

---

was taken for a longer period of time (4 times more than the others), however this time we got only part of the background. This is due to the fact that when the jet is not present, the pressure in the scattering chamber (and in the whole system) is lower. This data supports the idea that the background in the spectra is mainly due to beam interactions with the residual gas in the scattering chamber.

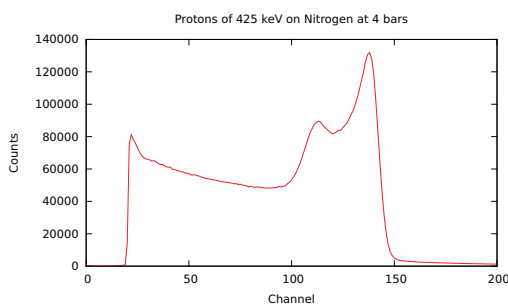


**Figure 5.9: Low energy protons - 425keV protons at 4 bars in the bottle.**

Since one of our scientific motivations is the study of nuclear reactions at very low energies to produce cross section data for stellar nucleosynthesis calculations, we try a scenario where the jet target is pushed up at higher densities and the accelerator pushed down at low energies. We used a 0.425 MeV (425 keV) [proton beam](#) and a Nitrogen jet target at 4 [bars](#) in bottle pressure, see [figure 5.9](#). Background shows up as a real problem, and the need for collimation is clear. There are two peaks reminder of the situation already seen before, suggesting that at such low energies the focusing conditions of the [beam](#) need to be improved.

### 5.5 Tests with Argon

Furthermore, experiments with Argon at 1,2 and 3 [bars](#) in bottle pressure were made (collimator was not in place), see [figure 5.10](#). The count rate distribution is somewhat similar to the previous plot however, besides the [channel](#) shift, two main differences can be noticed:

1. The main peak is better defined.
2. The back peak, has a higher count ratio, close to one with respect the main one.

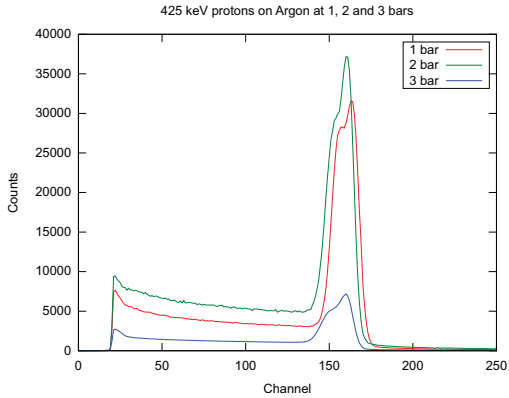


**Figure 5.10:** Argon Pressures - 425keV protons in Argon at multiple pressures.

The data was taken with different time intervals, we simply adjusted the data with respect to the first time interval:

Pressure (bar)	$\Delta t$ (sec)	Peak Channel	Adjusted Peak Counts
1	247	163	31483
2	85	160	37158
3	1184	160	7145

**Table 5.3:** Channel, height, peak channel and adjusted peak counts.

Table 5.3 shows two important things to notice:

1. The count rate increased with the pressure when going from 1 bar to two bar and afterwards it decreased to less than a fifth of the 2 bar value when going to 3 bar.
2. The peak channels are close to each other, in fact the second and third are exactly the same.

This leads us to speculate that there may be an optimum bottle pressure at which the count rate for the solid state detector is maximized.

The beam vs pressure experiments were performed again in order to see if this behavior could be reproduced, see section 5.6.

## 5. TESTS, RESULTS AND DISCUSSION

### 5.5.1 Argon and nitrogen pressure tests

A more systematic approach was taken this time. Protons at only one energy (1.8MeV) were used. This time, only the pressure and the gas were changed. In figure 5.11 the behavior of protons in Argon is shown. The collimators were not in place.

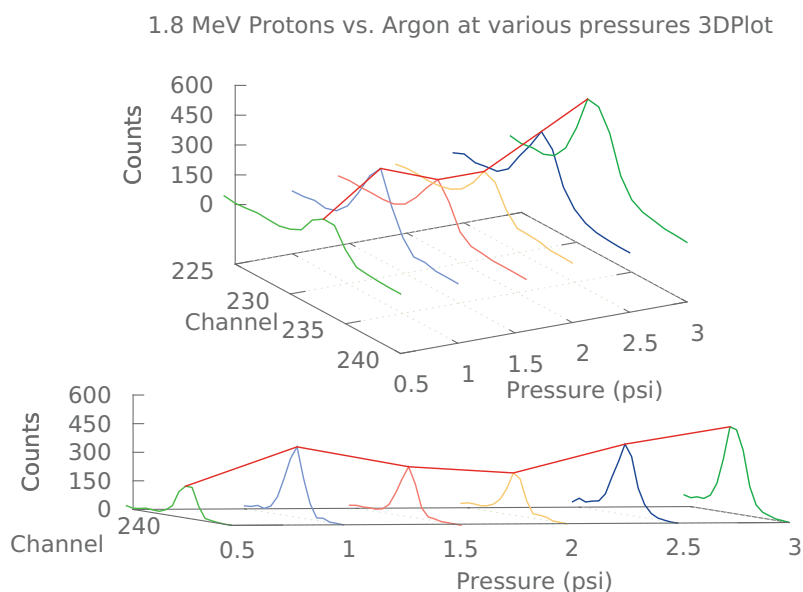


**Figure 5.11: 3D Argon** - View of the Argon data at different pressures.

The count rate changes with the pressure, measured from the bottle, more pressures were used this time (in comparison to figure 5.10) however the used energy was not the same<sup>1</sup>.

Figure 5.12 presents more angles to figure 5.11, including a channel shift, and therefore energy shift, see figure 5.12 (d).

It is worth mentioning that the count rate in figure 5.11 was much higher than in the newer case, figures 5.11 and 5.12 where 3mm collimators were used in front of the solid state detector.

They were not consistent with the relative channel shift, as can be seen by comparing the (d) part of figures 5.12 and 5.13.

<sup>1</sup>425keV before and 1.8MeV after



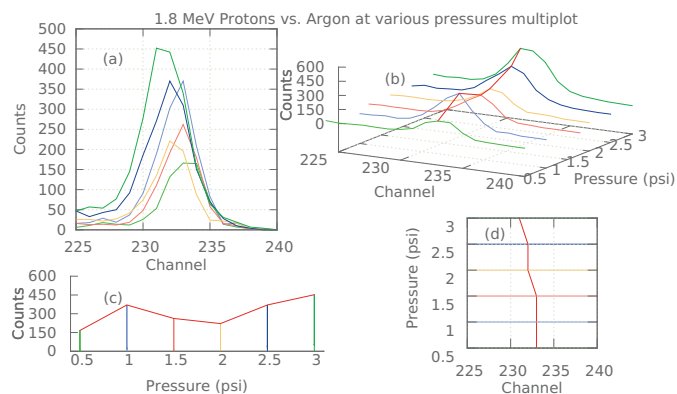


Figure 5.12: Argon various angles - The argon data seen from different perspectives.

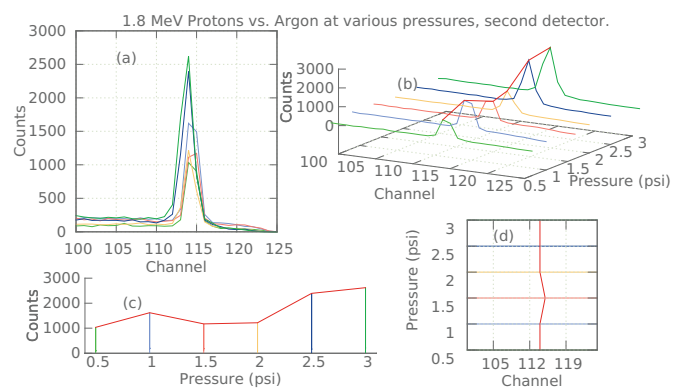
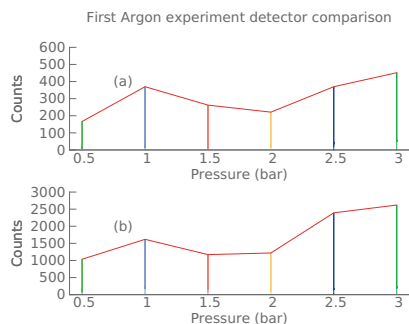


Figure 5.13: Argon various angles 60V - The argon data seen from different perspectives.

## 5. TESTS, RESULTS AND DISCUSSION

---

They were consistent with the count rate. Figure 5.14 compares the counts from the 40V detector (figure 5.14 (a)), with the 60V detector (figure 5.14 (b)). These are also shown separately in figures 5.12 and 5.13 (c). The relative changes are not exact but they agree with each other they show similar behavior.



**Figure 5.14: 40V vs 60V** - Comparison of the count rate of the 40V detector and the 60V.

Figure 5.15 makes a comparison of the detectors. This is the same data from the argon experiments.

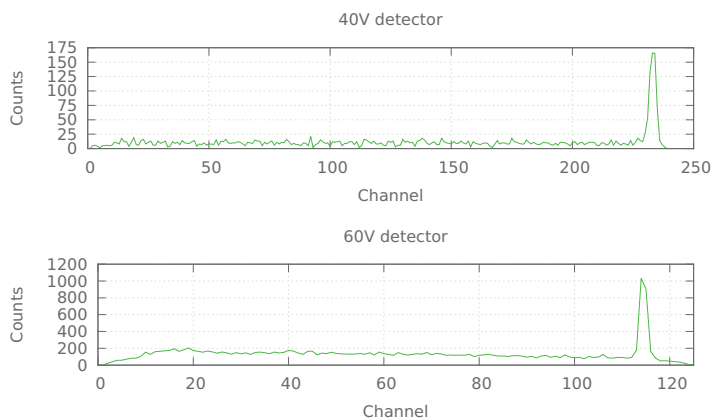


**Figure 5.15: Background detectors** - Compares the background between the detectors.

Choosing the same data set comparing the two detectors with their background we notice that the background count rate is higher for the 60V detector.

Since the count rate is different for both detectors we shall compare the background

to main peak pressure. From figure 5.15 we can extract the information shown in table 5.4.

Detector	background count	peak count	ratio
40V	25	160	0.15
60V	200	1000	0.2

**Table 5.4:** Background comparison.

Not only is the ratio higher for the 60 detector it also shows considerably more counts after the argon peak, we think it may be due to electronic noise, perhaps the gain factor was too large for the detector.

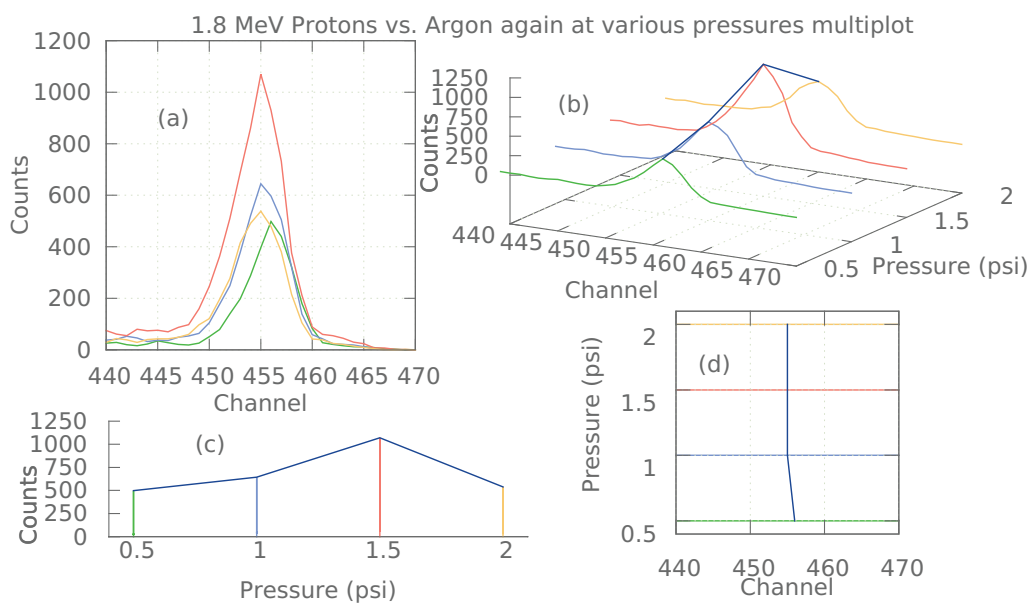


**Figure 5.16:** Argon again - Data of the repeated Argon experiment.

The accelerator's beam was not very stable, the 10 minute interval was used in order to average the ups and downs of the beam intensity. Assuming that the current oscillated around a central "average" value. This would imply that the past results of Argon that were performed the first time (the count rate variations in terms of the pressure) would be reproducible.

This was not the case, as it is shown in figure 5.16. The amount of measurements

## 5. TESTS, RESULTS AND DISCUSSION

were not as many as in figure 5.12 however 5.16 (c) differs from 5.12 (c).

The pressure measurement from the bottle was very stable as well as from the vacuum gauges throughout the system. The beam is to blame, a work around would be to acquire a digital integrator for the beam in order to monitor the total charge that reaches the Faraday cup during an experiment, not just at a particular time<sup>1</sup>.

A correct solution would be to check the integrity of the belt that delivers the charge in the accelerator, damages to it prevent a stable beam, replacing it would be optimal. Additionally a replacement of the ion source<sup>2</sup> will not only provide with a more stable beam, but also a much more intense one.

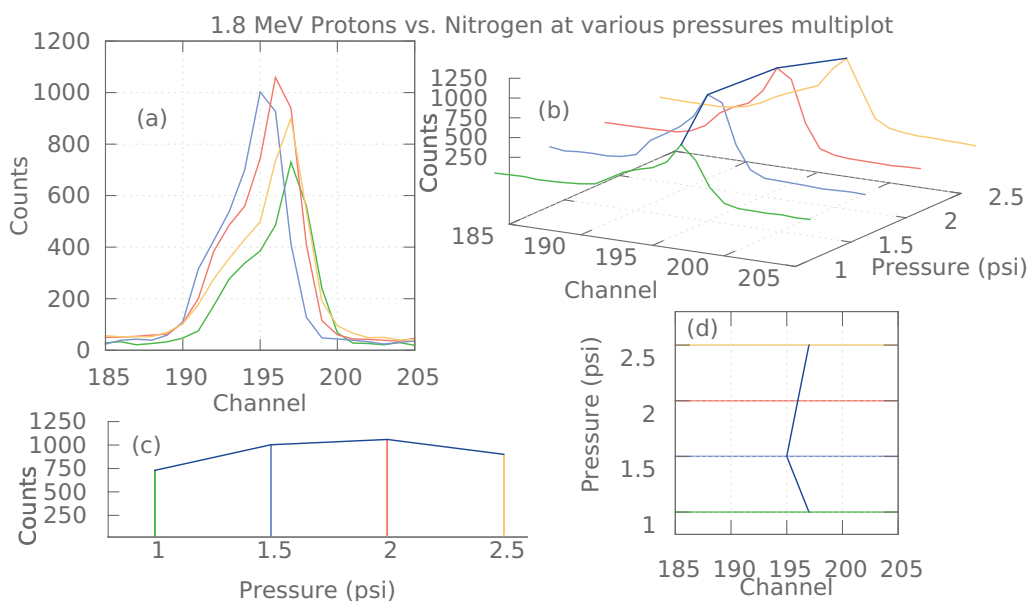


**Figure 5.17: Nitrogen data** - Data of Nitrogen.

The Nitrogen data is presented in figure 5.17. Similar to the past data from Argon. As expected, the count rate does change with the pressure. But as it has been mentioned before, the stability of the beam compromises a correct interpretation of the plots.

The nitrogen experiment was repeated. However, as in the case of Argon, the *pressure vs count* data does not agree with each other. But, as in the case of Argon, the data from the two detectors in a particular experiment was consistent.

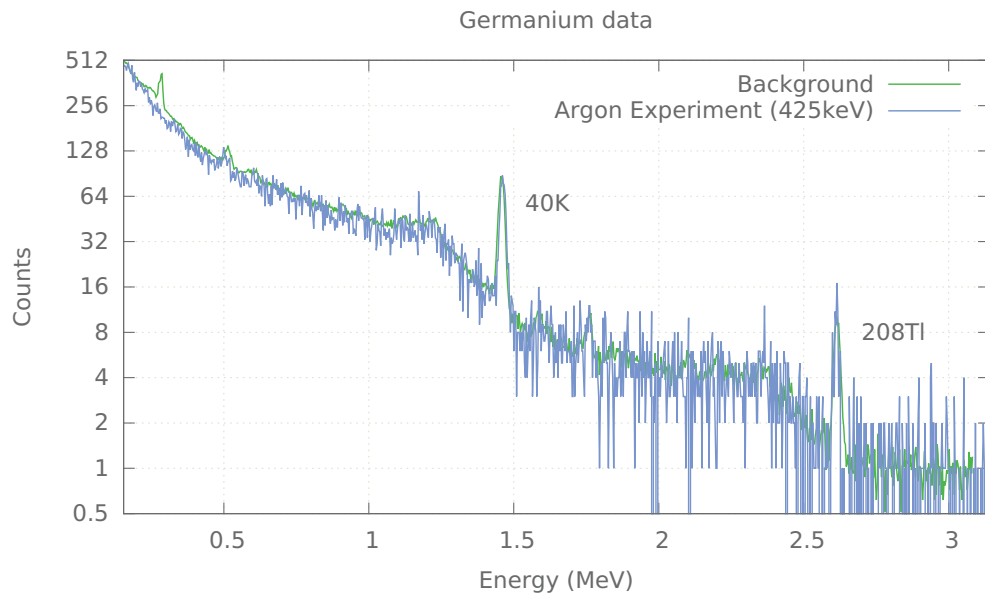
<sup>1</sup>Since it oscillates all the time.

<sup>2</sup>Already available in the lab.

### 5.5.2 Germanium Tests

The experimental array for this test is shown in section 4.2.8.4 and the respective theory is shown in section 3.3.2.1 and 3.3.2.

Experiments with a [germanium detector](#) were also performed, for this the [scattering chamber](#) was changed (in a matter of minutes) by replacing the LF250 blank flange with the special LF250 nose flange, as mentioned in section 4.2.8.4, this allowed for the placing of the [germanium detector](#) and the shielding, see figure 4.23.



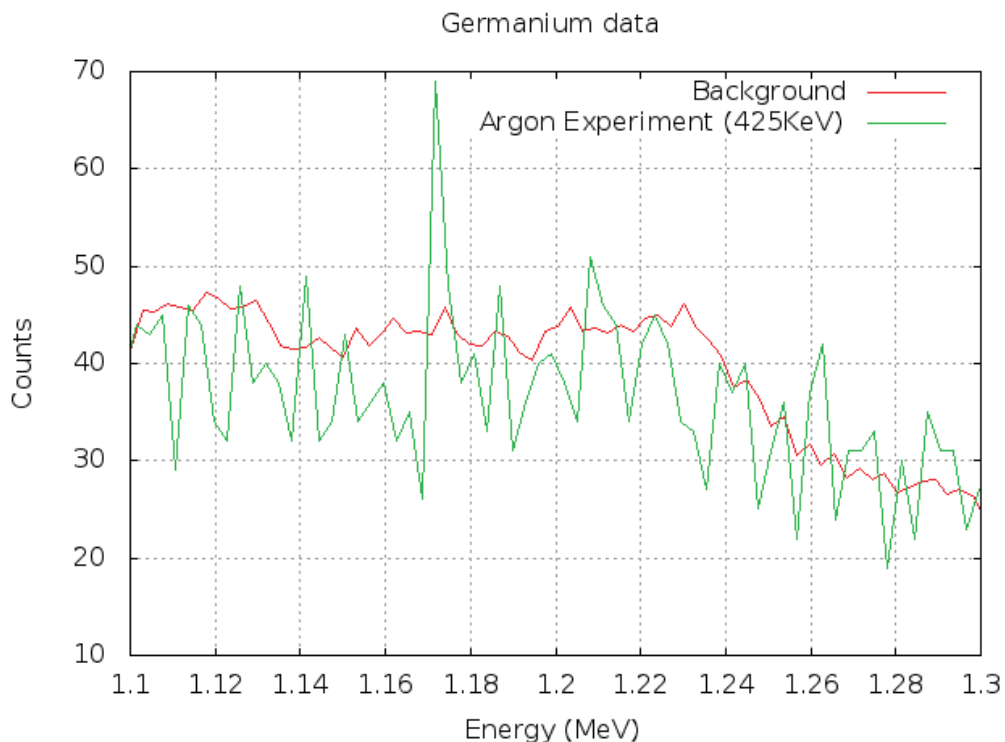
**Figure 5.18: Argon Germanium Data** - Data from the germanium detector.

Figure 5.18 shows the data from  $\approx 450\text{keV}$  [Protons](#) in Argon. This data was taken running the experiment as parasite of the low energy proton capture reaction  $^{12}\text{C}(p, \gamma)$  reaction being made in the astrophysics beam line during dead times in that experiment, the beam was just swung into our beam line to take data. The background was taken from the [germanium detector](#) for about 15 hours.

Two main peaks were identified from the background, the  $^{40}\text{K}$  peak (Potassium 40, 1.46083MeV) and the  $^{208}\text{Tl}$  (Thallium 208, 2.6146MeV). These nuclei form part of the natural background.

## 5. TESTS, RESULTS AND DISCUSSION

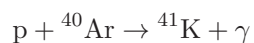
The data taken from the argon experiment is also shown in figure 5.18 the experiment only ran for a few minutes so the total gamma count was much less. The background was re-scaled so that it matched, for the most part, the Argon data.



**Figure 5.19: Argon Germanium Data Zoomed** - Data from the germanium detector, the background and the Argon data average are different.

The background data was also rebinned, using the program described in A.1, so that the  $^{40}\text{K}$  and the  $^{208}\text{Tl}$  peaks matched.

Some peaks seem to stand out from the background, a zoomed section of figure 5.18 is shown in figure 5.19. Between 1.16MeV and 1.18MeV there is a peak that could represent a fusion reaction. As discussed in section 3.1, if there is fusion between a proton and Argon then the resulting potassium would be left in an excited state and gammas would be emitted, as shown in equation (3.6b):



There happens to be a gamma of 1.1633MeV in the 2.1438MeV excited level of  $^{41}\text{K}$  energy spectrum.

The re-scaling of the counts was done from the  $^{40}\text{K}$  peak, however and improved re-scaling could make the background and the Argon data average approximately the same. Something that differs from what happens in figure 5.19, where the background is a bit above average.

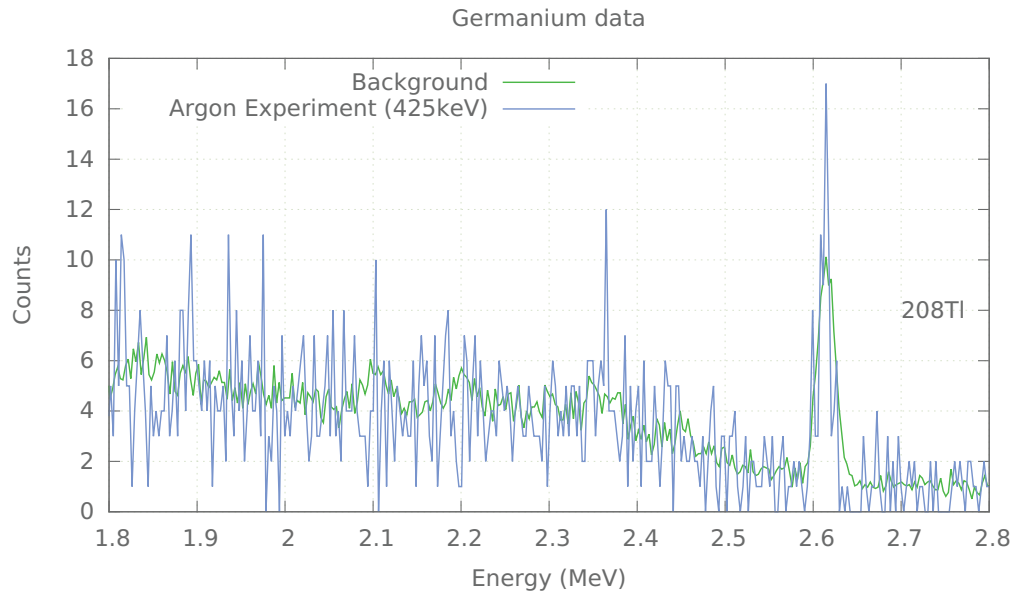


**Figure 5.20: Argon Germanium Data  $^{40}\text{Tl}$  Zoom - Higher energy peaks.**

Figure 5.20 show another section of the data. This time, close to the  $^{208}\text{Tl}$  peak. The counts tend to vary from zero to four times the respective background count. In the case of the Thallium peak the count rate seemed above the background one.

## 5.6 Experiments

The accelerator went through a scheduled maintenance and it gave the shop time to finish building the new set of holders.

## 5. TESTS, RESULTS AND DISCUSSION

### 5.6.1 EBS of air, nitrogen and argon experiments

The experiments were done, using the EBS setup with the new updates as described in section 4.2.8.2. That is the steel plane surface with holes and the detector holders, also shown in figure 4.21. The collimator is in place.

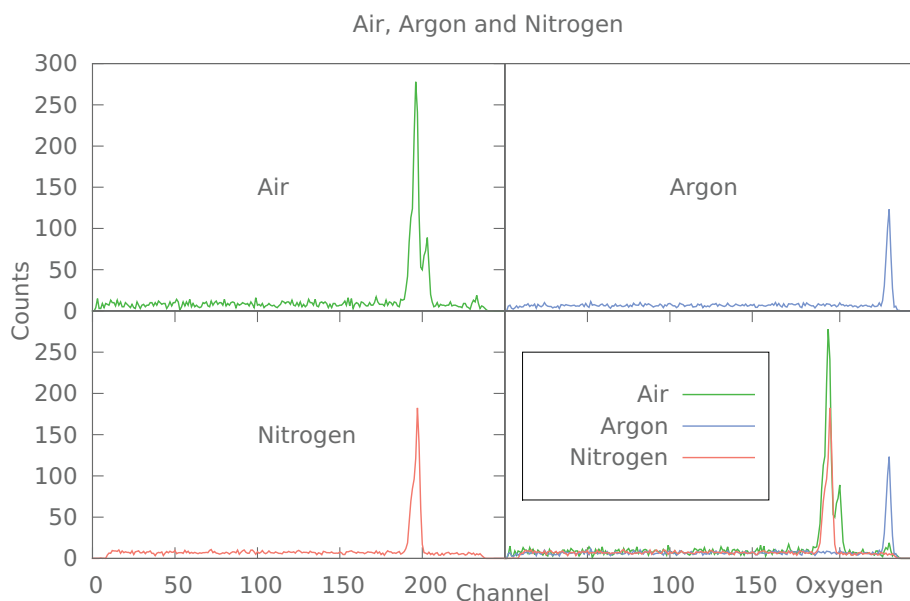


**Figure 5.21: Air multiplot** - Shows the air plot, the nitrogen peak, the argon peak and the superimposed plot of all of them.

Each of the new experiments were performed during a 10 minute acquisition time. Except the first one, performed with air, where the acquisition was for 20 minutes and the beam current was between  $100nA$  and  $1\mu A$ . Figure 5.21 shows this data as well as data for Nitrogen and Argon.

Note that the Nitrogen peak matches almost perfectly with the expected one in air. Being the acquisition time so long for the first air experiment, the Argon peak started to show. Note the Oxygen peak right after the Nitrogen one.

The Nitrogen experiment was done after a computer problem, it had to be restarted however the detector gains were, unintentionally changed. The Nitrogen peak appeared in a higher channel, the data had to be rebinned (see section A.1. In order to re-calibrate another air experiment was made and the Nitrogen and Oxygen peaks were used as



reference. The Nitrogen peak and the respective one in the Air experiment, in this scenario, matched perfectly.

The Nitrogen and the Argon data were re-scaled for better contrasting with the Air data. For Nitrogen the count data was divided over 4 and the Argon count data was divided over 3.

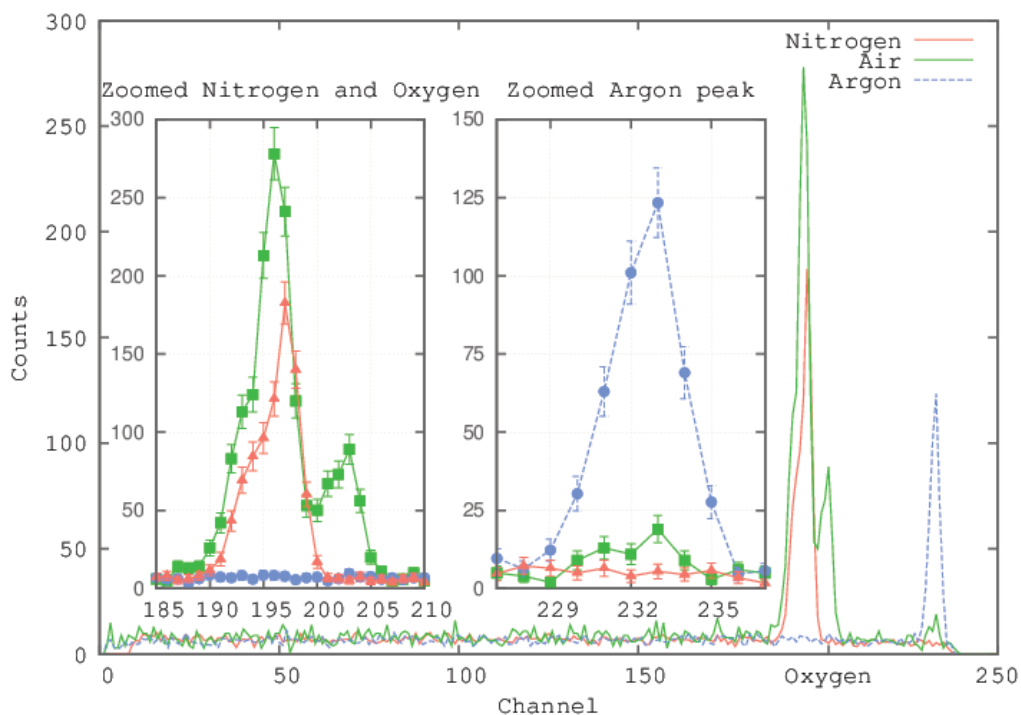


**Figure 5.22: Argon peak** - The Argon and the corresponding peak in air.

Figure 5.22 shows a closer look of the Argon peak and the corresponding one in air. The average background count is around 8 counts.

Table 5.5 shows a comparison of the old measurements, the first experiments performed with the jet vs the new ones. The percentages shown here show a closer value to the reported typical values, than the measurements from the first experiments shown in section 5.3.

The in the case of Argon the elevated percentage could be because of the fact that Argon experiments were also performed in the lab and the concentration of Argon inside the lab was elevated, however the SIMNRA fit analysis shown in figure 5.24 does

## 5. TESTS, RESULTS AND DISCUSSION

---

Peak Name	Old	New	New with SIMNRA	reported
Nitrogen	71%	74.5%	78.0%	78.09%
Oxygen	29%	22.5%	21.3%	20.95%
Argon	not shown	3%	0.97%	0.93%

**Table 5.5:** Comparison of the old vs new and reported percentages in Air.

show a better fit to the reported values as shown in table 5.5. In any case, the use of the collimators and the increased acquisition time did seem to help a lot in improving the measurement.

The oxygen air abundance measurement was consistent with the reading of an oxygen detector placed in a new newly opened accelerator that's near the jet setup.



**Figure 5.23:** Oxygen detector - Reading from the Oxygen detector in a nearby lab.

Figure 5.23 is a picture of the reading, we notice that it is precisely the same value as the measured one, shown in table 5.5. This gives us good confidence in our numbers.

The SIMNRA analysis also gave an estimate of the density of the jet  $n$ :

$$n \approx 2.1 \times 10^{18} \text{ atoms/cm}^2 \quad (5.5)$$

Equation 5.5 is consistent with the calculated values in section 3.4 in equations 3.44 and 3.45, were the calculated values was  $5.25 \times 10^{17}$  molecules/cm<sup>3</sup>, multiplying by the nozzle thickness (0.75cm) and considering molecular nitrogen (N<sub>2</sub>) we get  $1.5 \times 10^{18}$  atoms/cm<sup>2</sup>. However the value in equation 5.5 is actually a lower bound under the most pessimistic conditions. Given the fact that the beam was not stable enough.

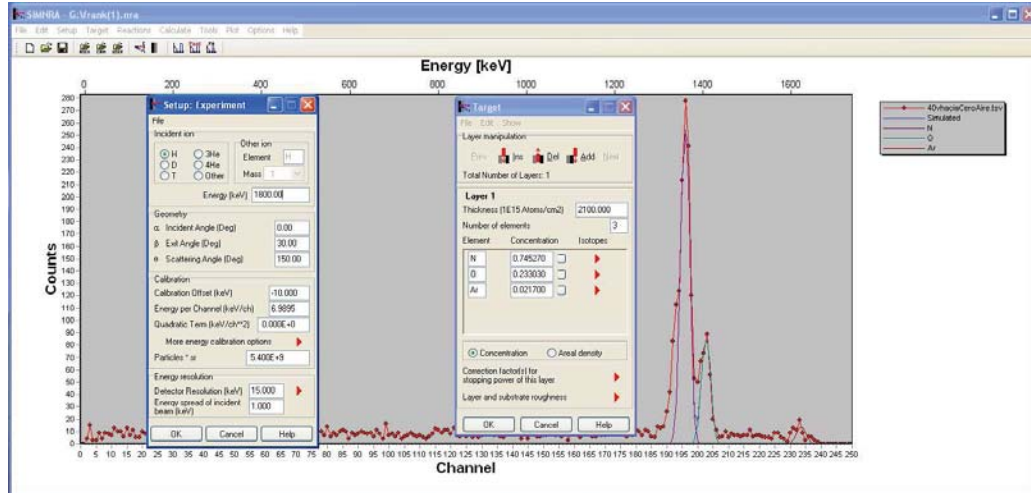


Figure 5.24: SIMNRA air fit - Shows a fit to the air data.

### 5.6.2 Nuclear Physics Experiments

The theory regarding this section can be found in the beginning of chapter 3, mostly section 3.3 and section 3.3.1. The experimental array is shown in section 4.2.8.5, it is an E- $\Delta$ E telescopic detector array. A complete description in how the histograms, in this section, were calibrated is shown in appendix B.

The gas jet target was produced by injecting air at atmospheric pressure (78% nitrogen, 20% oxygen and 2% other elements).

Deuteron energies were varied between 2.2 and 3.36 MeV. Beam intensities were measured in a faraday cup before the scattering chamber during beam setup and optimized before data taking. Typical beam currents were between 200 and 1000 nA. Signals from the silicon detector array were handled by standard NIM electronics.

Data acquisition ran in a PC with a Windows platform. The control program has been developed with Labview software. A CAMAC interfaces the PC and the detection system. In this experiment the trigger was provided by the  $\Delta$ E detector signals. The logic signal was produced by a discriminator keeping the threshold just above the electronic noise to include low energy signals.

The  $^{14}\text{N} + \text{d}$  reaction has several exit channels with relatively high Q values, (Table 2.3). The Coulomb barrier is around 2.3 MeV to form the  $^{16}\text{O}$  compound nucleus. Since the Q-value for fusion is very large (20.74 MeV) we are able to study a high excitation

## 5. TESTS, RESULTS AND DISCUSSION

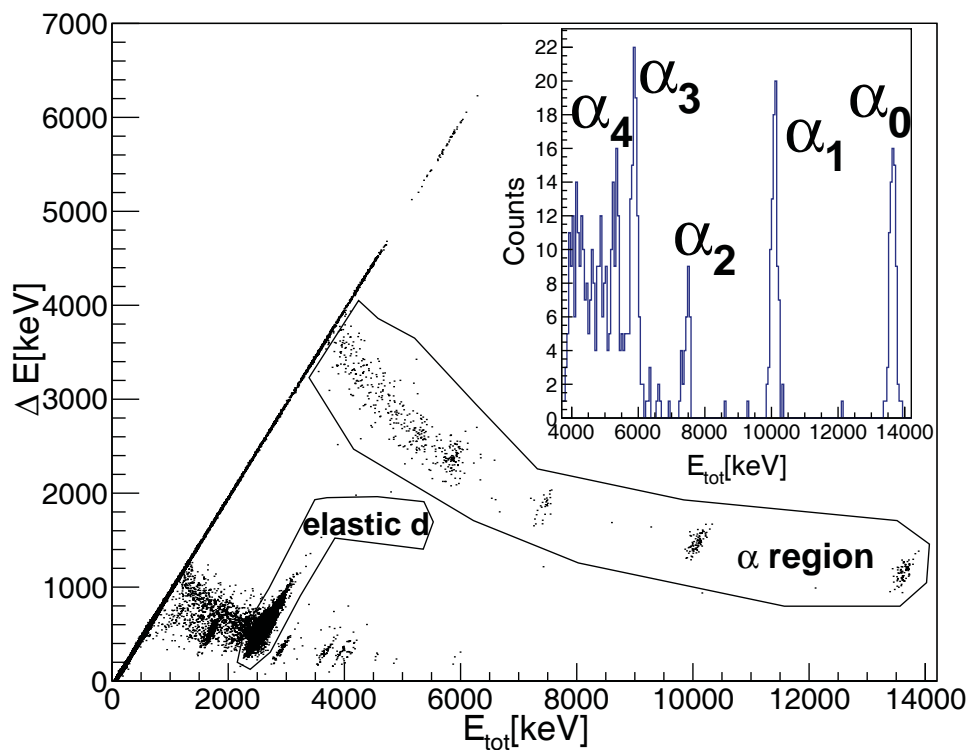


**Figure 5.25: 2D  $\Delta E$  vs  $E_{tot}$  histogram** - Typical 2-dimensional histogram  $\Delta E$  vs  $E_{tot}$  of the  $d + {}^{14}\text{N}$  reaction ( $E_{cm} = 2.51\text{MeV}$ ). Deuterons and alphas are clearly identified. The elastic peak is used in each case to extend and confirm the energy calibration and for normalization purposes (see text). In the sub-frame, a projection from the total energy spectrum of the  $\alpha$  banana, is shown.

region in  $^{16}\text{O}$ .

We concentrated on the  $^{14}\text{N}(d,\alpha)^{12}\text{C}$  channel where alpha particles are detected at a fixed angle in the laboratory, while the bombarding energy is changed between 2.2 and 3.36 MeV. So our study spans an energy interval right at and above the top of the barrier.

Data reduction and analysis was done with the software ROOT (54). All histograms showed here (1 and 2d) were generated with it. A typical two dimensional histogram from our data is shown in Figure 5.25. In the vertical axis we plot the energy calibrated signal from the  $\Delta E$  detector and in the horizontal axis, the calibrated total energy recorded by our telescope  $E_{tot} = E + \Delta E$ . Section B concentrates in how this calibration was performed. Elastically scattered deuterons were used to verify the energy calibration of the beam.

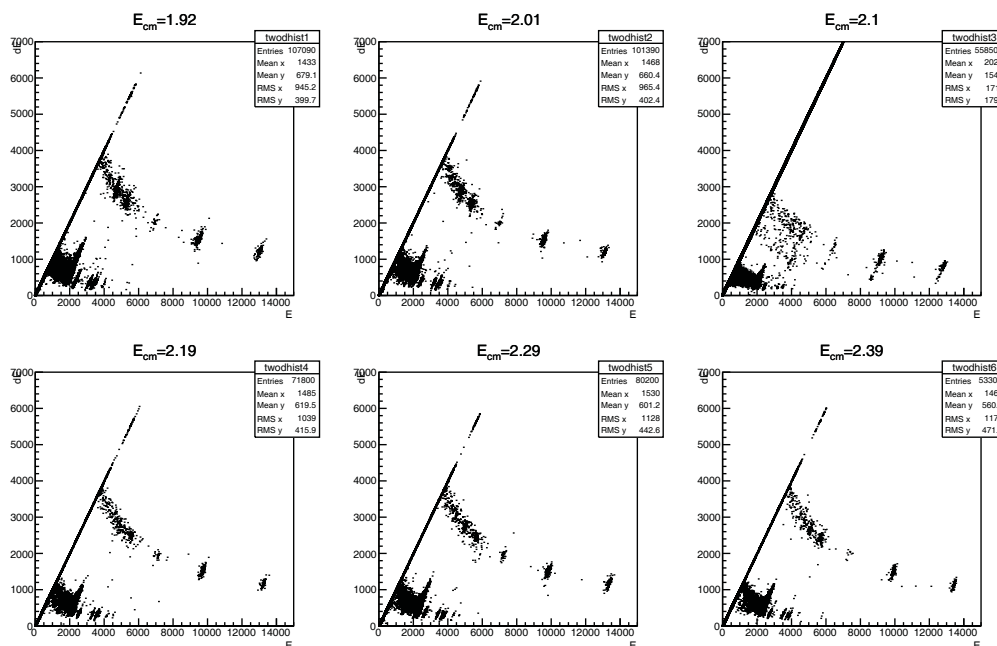


Figure 5.26: 2D histograms - Set of 2D histograms

Figures 5.26 and 5.27 show multiple calibrated  $\Delta E$  vs  $E$  two dimensional histograms at various energies. The elastically scattered deuterons and the alphas are easily identifiable, in the same manner as in figure 5.25.

## 5. TESTS, RESULTS AND DISCUSSION

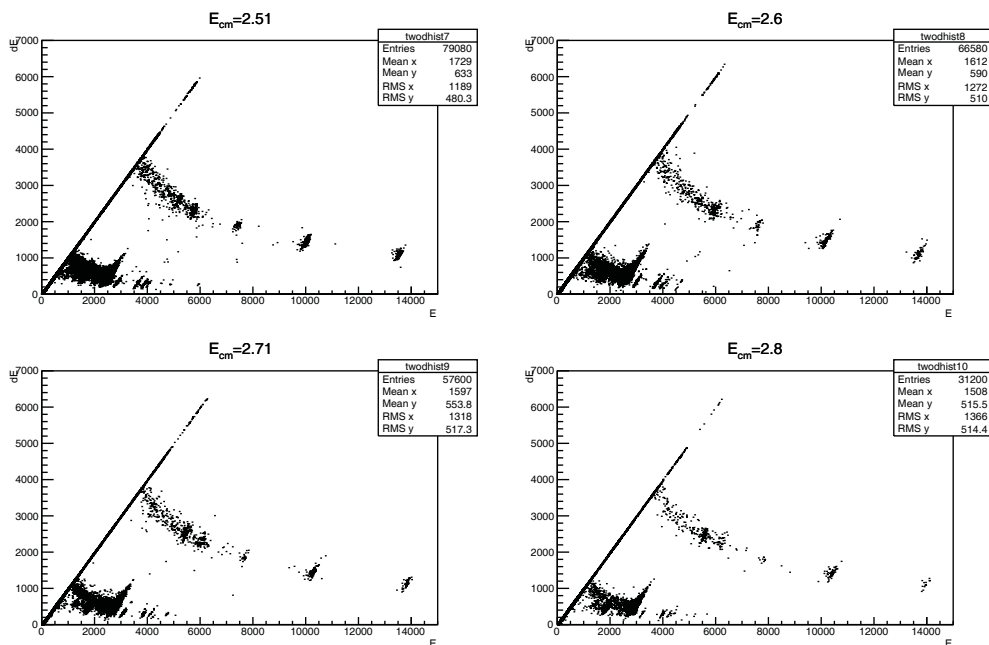


Figure 5.27: 2D histograms 2 - Second set of 2D histograms

The straight line in all of the plots are simply noise events or particles that got stopped by the  $\Delta E$  detector not reaching the E detector. The data under the line represents particles that managed to reach the E detector.

Figures 5.28 and 5.29 are the total energy projections of the alpha particle region at each respective energy given by the Figures 5.26 and 5.27.

In the same manner as the subplot of Figure 5.25, the alphas in Figures 5.28 and 5.29 can be identified by enumerating the peaks from right to left.

Values in Table 5.6 represent the expected energies of the resulting scattered alpha particles from multiple excitation levels in  $^{12}\text{C}$  Figures 5.28 and 5.29 correspond nicely to the Table values. The table was made with the help of isonav (see section A.4 in appendix A).

It is important to notice the  $\alpha_2^1$  in Figures 5.28 and 5.29 since this corresponds to the famous Hoyle state in Carbon 12. It is on average the smallest peak when compared to the rest of the alphas. Also notice that the obtained spectra are in essence noise free, if this wasn't the case then probably the background noise would have hidden the

<sup>1</sup>Third peak from the right.

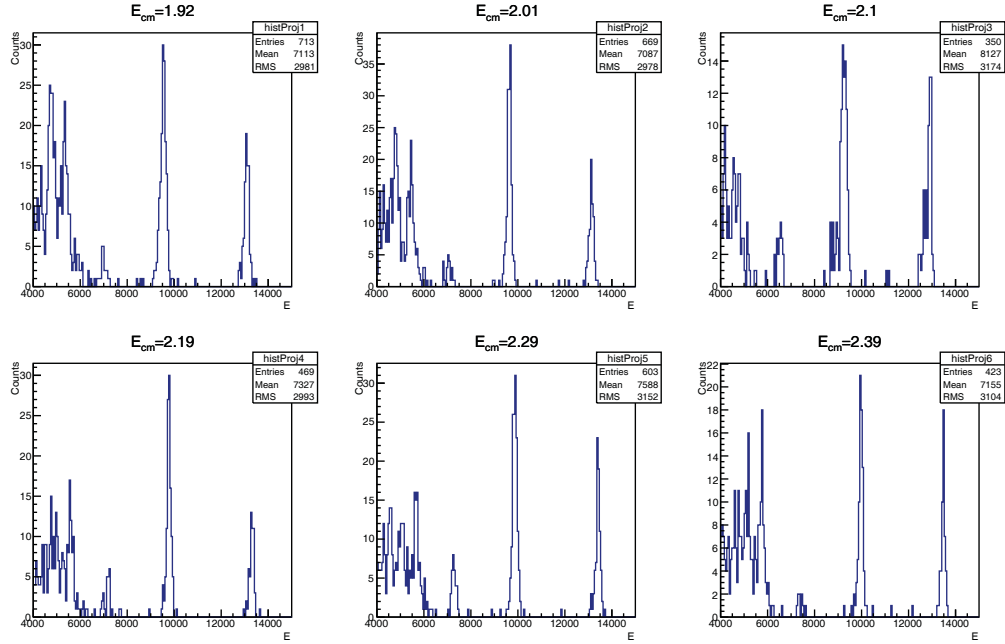


Figure 5.28: histogram projection 1 - 1D histograms, from  $E_{CM} = 1.92$  to  $2.39$  MeV, the energy unit on the histograms is in keV

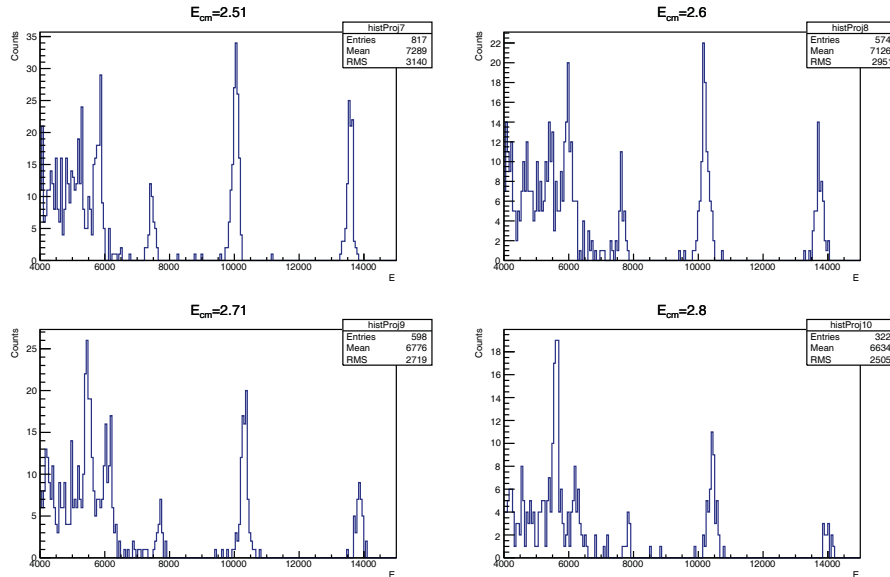


Figure 5.29: histogram projection 2 - 1D histograms, from  $E_{CM} = 2.51$  to  $2.8$  MeV, the energy the unit on the histograms is in keV

## 5. TESTS, RESULTS AND DISCUSSION

---

Carbon						
Excitation		Base	First	Second	Third	Fourth
Energy [MeV]		0	4.43	7.65	9.65	10.3
$E_{Lab}$	$E_{cm}$	$\alpha_0$	$\alpha_1$	$\alpha_2$	$\alpha_3$	$\alpha_4$
2.20	1.92	13.11	9.55	6.94	5.31	4.76
2.29	2.01	13.20	9.64	7.03	5.4	4.8
2.40	2.1	13.31	9.75	7.13	5.50	4.95
2.50	2.19	13.42	9.85	7.23	5.59	5.04
2.61	2.29	13.53	9.96	7.33	5.14	5.14
2.73	2.39	13.65	10.07	7.45	5.81	5.26
<b>2.87</b>	<b>2.51</b>	<b>13.79</b>	<b>10.21</b>	<b>7.58</b>	<b>5.94</b>	<b>5.38</b>
2.97	2.6	13.89	10.31	7.68	6.03	5.48
3.10	2.71	14.02	10.43	7.8	6.15	5.6
3.26	2.85	14.18	10.59	7.95	6.3	5.74
3.36	2.95	14.28	10.68	8.07	6.39	5.83

**Table 5.6:** Center of mass energies and the corresponding alpha energies for the different  $^{12}\text{C}$  excitation levels for all deuteron beam energies ran in this experiment. The values in bold correspond to Figure 5.25. **Note:** All energies are in MeV.

alpha peaks in particular the Hoyle state alpha. Perhaps this is one of the reasons it went unnoticed for many years. Notice that  $\alpha_2$  has on average the lowest differential cross section, when compared to the other alphas.

Cross sections were measured, using equation 3.17 from section 3.3.1, they are shown in figure 5.30.

From Figures 5.28 and 5.29 it is worth also noting that the relative height of  $\alpha_3$  and  $\alpha_4$  increases considerably as the energy increases. This is also reflected in the cross section plot (Figure 5.30).

For the  $\alpha_4$  case there could be an overlap from a reaction with oxygen (since it was an air jet and not pure nitrogen):



It is possible that the  $\alpha_0$  from equation 5.6 overlaps with the  $\alpha_4$  from  ${}^{14}\text{N}(d, \alpha){}^{12}\text{C}$ .

A common maximum for the different  $\alpha$ 's can be noticed around  $E_{cm} = 2.01\text{MeV}$  (figure 5.30). This can be explained through a compound nucleus reaction from an  ${}^{16}\text{O}$  resonance, figure 5.31.



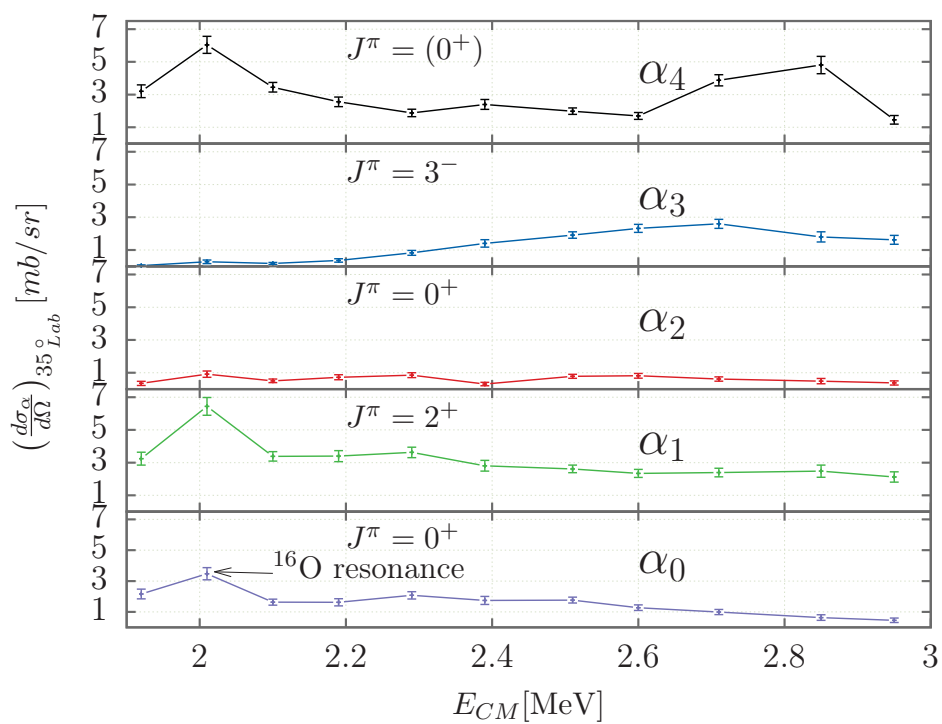


**Figure 5.30: Alpha cross section** - Differential cross section at  $35^\circ$  in the laboratory system for alpha decays to the lowest lying  $^{12}\text{C}$  nuclear states, statistical error bars are also shown (the average error is around 15% with a minimum of 8% and maximum of 35%, no systematic errors are reported). Quantum numbers (spin and parity) of each state are given. The lines are drawn to guide the eye.

## 5. TESTS, RESULTS AND DISCUSSION

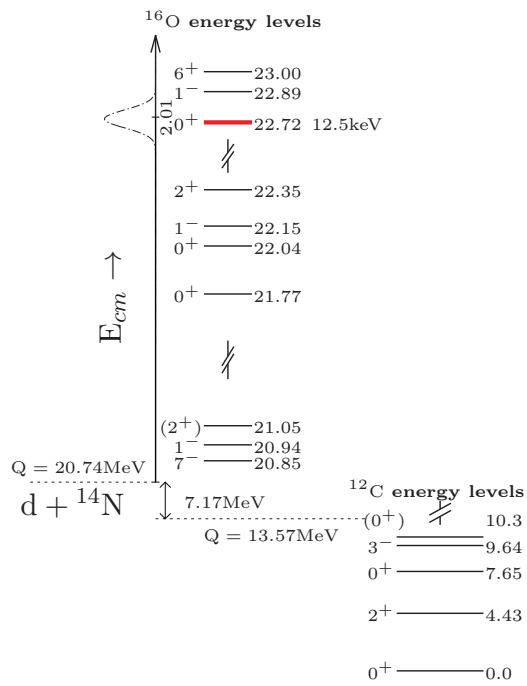


**Figure 5.31: Oxygen levels** -  $^{16}\text{O}$  nuclear level scheme. On the left, the entrance channel ( $d + ^{14}\text{N}$ ) is marked. On the right,  $\alpha$  emission to different excited states in  $^{12}\text{C}$  is also shown.

The  $d+^{14}\text{N} \Rightarrow ^{16}\text{O}^*$  reaction, leaves the Oxygen in a highly excited state ( $Q=20.74$  MeV). The Oxygen could de-excite via gamma emissions (as in section 3.3) or it could breakup into other particles. In particular we were interested in the  $^{16}\text{O}^* \Rightarrow \alpha + ^{12}\text{C}^*$  channel, since the alphas are easily identifiable and it allows us to study different states of carbon 12 ( $Q=13.57$  MeV).

If the available energy ( $Q+E_{CM}$ ) is near an excitation level in the compound nucleus ( $^{16}\text{O}$ ), as shown in figure 5.31, then the probability of forming the compound nucleus is increased and therefore the number of breakup particles should increase<sup>1</sup>.

---

<sup>1</sup>As noted through the increase of the differential cross section.

## 5. TESTS, RESULTS AND DISCUSSION

---



## 6. CONCLUSIONS AND FUTURE OF THE PROJECT

---

### 6.1 Conclusion

This work describes the supersonics gas jet target system (**SUGAR**) in all its parts. It has been designed to take advantage of parts that can be found commercially, decreasing considerably the need for special parts and adaptors custom made in a mechanical shop. Spare parts and extensions to SUGAR can then be found and installed very easily.

The performed experiments provided a good proof of principle for the future of the project. The overall system worked remarkably well, the [differential pumping system](#) allowed us to lower the pressure several orders of magnitude from the [scattering chamber](#) all the way to the connection to the accelerators [beam selector magnet](#).

The pressure was even lower on the side of the jet [beamline](#) than on the accelerator's side! All this was done through connected chambers that allow gas flow in between the chambers. The apertures that connect them are 5mm in diameter, they had to be perfectly aligned in order to let the beam go through.

The beam was partly lost in the way through the system, however approximately 60% was allowed to go through. A very positive result since the count rate is not greatly affected by the [differential pumping system](#) itself.

The [EBS](#) also showed positive results, we were able to distinguish different components of air. That is; Nitrogen, Oxygen and even Argon. We were able to verify this claim theoretically as well as experimentally.

The experimental verification for the peaks was done by connecting the respective gas bottles to the system and verifying that it was in fact in the same channel as the respective peak in the air data.

From the peak height we were able to obtain the abundance of the main components of air noted that the measured abundance is close to the reported one.

The first set of data was a bit noisy however this was partly fixed with a newer experimental setup that included collimator ridding us from the back peaks.

The germanium experiments gave us a good proof of principle experiment, since we were able to detect gammas with count rates above the background radiation. Unfortunately we were unable to calibrate properly the [germanium detector](#) making us uncertain of the proper energy-channel relationship. More experiments are needed once the detector gets repaired.

The [Schlieren](#) technique allowed us to visualize the jet from the straight tube nozzle, however not from the rectangular one<sup>1</sup>. The reason for this, as explained in section 5.2.1, the theoretical exit density is much smaller than the atmospheric pressure. The flow is so “thin” that the behavior is simply different.

As a first case study for nuclear physics, we took data from the  $^{14}\text{N}(\text{d}, \alpha)^{12}\text{C}$  reaction around the Coulomb barrier. This is one of the most prolific reactions induced by deuterons on an air supersonic gas jet target. We extracted excitation functions for  $\alpha_0$ ,  $\alpha_1$ ,  $\alpha_2$ ,  $\alpha_3$  and  $\alpha_4$  (35° lab). The behavior of these excitation functions is consistent with the presence of a previously reported excited state of  $^{16}\text{O}$  ( $0^+$  at 22.72 MeV). It is worth mentioning that previously published work on this reaction is scarce or nonexistent. Especially for the  $\alpha_3$  and  $\alpha_4$  at forward angles at the energies we report here. We plan to pursue this measurements both with pure nitrogen and air jets as well as with solid thin ( $\text{Si}_3\text{N}_4$ ) targets. Hauser-Feshbach calculations will be made to understand the relative intensities of the alpha decays observed.

Air gas targets are quite practical: they never run out (no bottle to change), no need to recover at the exhausts of the pumping systems or dumping pure gases into the environment, provides a well-known target composition (N-O-Ar) always fresh and immutable, it is perfect for setup and fine-tuning of the system, there is even a variety of research problems to work out with and it’s free. For any other kind of target, a bottle is needed. For higher areal density targets, we produced and characterized jets with inlet pressures of up to 5 bar of **pure** nitrogen and argon from gas bottles.

The system is now known as **SUGAR** (SUpersonic GAs jet taRget).

## 6.2 Future of the project

A test using the Schlieren technique was made outside the system to visualize the supersonic flow produced by our nozzles. The stationary shock patterns of the flows were shown. We were able to measure Mach numbers at different pressures. Following to this successful tests, a similar setup is being designed and tested to monitor the supersonic gas jet targets used in future experiments.

---

<sup>1</sup>Except from a simple rectangular aperture nozzle.

## 6. CONCLUSIONS AND FUTURE OF THE PROJECT

---

The system is expected to work from [EBS](#) and conventional nuclear experiments to astrophysics and even neutron production. Some of these experiments can already be performed and others can be done with the proper upgrades.

The system is functional, however there are also some upgrades that will improve the performance of the system greatly by, for example, reducing the time to get the system ready.

The germanium detector should be fixed in order to continue the astrophysics experiments with the system.

<b>Problem</b>	<b>Solution</b>
Differential pumping system gets misaligned with earthquakes	Supports for differential pumping system Flexible LF250 nipple for quickly aligning the scattering chamber
The beam is not stable	Digital integrator for the Faraday cup New ion source
Can't open differential pumping system once started	Valves for the pumps
Accidental venting	Protection system for pumps that includes a set of automatic valves
Monitor the flow rate from the bottles	Adapt a flow meter
Experimental setup won't fit in the scattering chamber	The entire chamber can be replaced the modular design allows this.
Higher throughput must be handled	Replace the catcher pump, replace or increase pumps in the differential pumping system.
Expensive and hazardous gases have to be used	Recirculation system and a security protocol are in order.

**Table 6.1:** Shows a set of problems with solutions for the system

Table 6.1 shows a set of problems and solutions for the system. It literally takes weeks to realign the system and only a few seconds to get misaligned by an earthquake<sup>1</sup>.

The [differential pumping system](#) is rather heavy and the lever arm made from the [diffusion pumps](#) connected to the chamber is quite large. If the system also supported

---

<sup>1</sup>However the extra tightening of the system has proved useful.



the end that is not connected to the [differential pumping system](#) chambers it would be much more robust.

The LF250 flexible nipple could also increase the speed in aligning, since a much finer control of the [scattering chamber](#) is given<sup>1</sup>.

The fact that we cannot have a correct measurement of the beam in function of time is also a problem that has to be addressed. The main reason is the stabilization sensor. It compensates a magnet is the beam is going to low or too high, in order to keep it centered. This causes a small angle shift, which is negligible at small distances. But at greater ones such as in the case of our beamline, it poses a problem. Remembering the fact that we also need the beam to go through small apertures.

A new ion source will have a much higher current throughput and will be more stable. This is more of a long term solution.

To be able to open part of the [differential pumping system](#) while it is still running will literally reduce days (or even weeks) of work into minutes. Because we do not have to bring the entire system up to air and down again. Considering that the [diffusion pumps](#) need at least 40 minutes of cooling time.

Opening the the system like this help us align rather easily with the beam, as explained in section [4.2.7](#).

The [scattering chamber](#) can be opened and closed in a matter of minutes for various reasons, like changing the experimental setup. This chamber is isolated from the [differential pumping system](#) through a manual valve. Once the [roots system](#) is running, the pressure is low enough for the valve to be opened. However, if it is mistakenly opened while the whole system is up to air the pumps will overload with a hundred times more pressure than they can handle.

This most definitively would wreck the pumps and take the [turbo pump](#) beyond any hope of being repaired. Accidentally venting the pumps through their mechanical backing pump would be even more disastrous.

These were only a couple of examples in showing just how vulnerable the system is to total disaster just by accidentally venting. Automatic valves would protect the system and decrease greatly the risk of such an event.

Apart from the theoretical calculations, that calculate the flow rate in terms of pressure and the [nozzle](#)'s throat, an experimental measurement would be much more

---

<sup>1</sup>Remember that the scattering chamber is connected to the roots system.

## 6. CONCLUSIONS AND FUTURE OF THE PROJECT

---

accurate. The correct instantaneous flow rate may help us to determine properly the target properties.

The flow meter is already available at the lab, and it can be calibrated with various gases and with various throughput ranges the proper adapters are yet to be designed, in order to adapt it to the system.

In case the [scattering chamber](#) is too narrow for the experimental setup, for example, a wider angle [germanium detector](#). The entire [scattering chamber](#) can be replaced, it only needs to adapt to the [concentric pipes](#), two [QF40](#) connectors<sup>1</sup> and an adapter for the [nozzle](#).

In case higher throughput has to be handled, the central pump, used for the catcher, can be replaced with a medium sized [roots system](#). The pumps in the [differential pumping system](#) can also be replaced with faster (and even cleaner) pumps. The chambers allow up to 4 pumps in each stage, this can even reduce the length of the entire system by removing chambers.

A systematic optimization of the system could also improve the performance of the system such as in (5, 36) by changing the nozzles, temperatures and catchers<sup>2</sup>.

In order to achieve the final aim described in section 2.1, upgrading the system to recirculate gas is paramount. Not only do we need to **protect** the precious  $^2\text{H}$  gas, we also need to **protect** ourselves from it! The volatility of the gas is **important** to handle but also the proper radiological protection from the resulting [neutrons](#) produced in the reaction described in chapter 2. However it is still important to note that the alternative reactions shown in section 2.1.1 could prove better candidates. Experiments with MONDE (the neutron detector) will prove useful for making a smart decision.

---

<sup>1</sup>For the beam entrance and exit

<sup>2</sup>Our design is as flexible as theirs.



## A. SOFTWARE DEVELOPMENT

---

The main program used for parameter search is called `gasflow`, it was a program written in the *C programming language*. And it is too big to be included in the present work, however chapter 3 gives a good outline in how it works.

This appendix concentrates in some of the developed scripts written in `Bash` and `AWK`. Together, this 2 languages can achieve very powerful tasks. Fantastic for data extraction and manipulation. The data was afterwards plotted and tweaked with `gnuplot` scripts, not discussed in this chapter.

Plenty of `ROOT` macros, bash and python scripts were written but are not included for the sake of brevity. They were important for much of the analysis shown in section B. A description of such scripts is briefly mentioned in A.4 .

### A.1 Rebinning

Comparing data that has different bin distribution can be a tricky task. Two plots can have, essentially, the same data. However one of them can have 256 bins (or channels) and the other one 512. Simple tasks such as subtracting the data is not so straight forward.

With the next scripts, squeezing the data *properly* from the larger plot to adapt to the smaller plot is an easy task. It is only needed to have a linear relationship from the large bin data to the smaller one. Identifying two peaks is more than enough for each set.

The code consists of two parts, a `Bash` script that requires an *input file* and handles some simple tasks. The script calls an `AWK` script that handles the heavy loading for the rebinning.

The program is called `reBin.sh`<sup>1</sup> and it calls an `AWK` script called `newAwkscript.awk`

```
1 #!/bin/bash
2
3 # A simple script for changing the bins in the
4 # (already) formatted
5 # data file for the plots. It uses linear reBining.
6
7 if [ $# != 1 ]
```

---

<sup>1</sup>Note: equivalent scripts were also made for rebinning in `ROOT`.

```
8 then
9     echo "Error: $0 Needs exactly one argument." >&2
10    exit 1
11 elif [ ! -f $1 ]
12 then
13     echo "Error: File \"$1\" does not exist." >&2
14     exit 2
15 fi
16
17 awk -f newAwkscript.awk $1
18
19 exit 0
```

The important parts are done by the `newAwkscript.awk` program, `AWK` programs have a simple structure, it consists of three parts. The `BEGIN` section, a middle section that is optionally preceded by a regular expression<sup>1</sup>, and an `END` section.

```
1 awk BEGIN{initialization} [regexp] {commands} END{finishing stuff}
```

The `BEGIN` and `END` sections are also optional. The language has a whole set of internal variables that do complex data manipulation tasks in a very reduced space. `AWK` is famous for making *one liners*. *Note:* The `$N` syntax is different from `Bash` where it represents the  $N^{\text{th}}$  argument, in `AWK` it represents the  $N^{\text{th}}$  column<sup>2</sup>.

`AWK` programs can be extended in a file to be called later as in our case for the `newAwkscript.awk` program:

```
1 #!/usr/bin/awk -f
2 #This script does the heavy loading for reBining
3 #It is called by reBin.sh
4 #The first column has to be sorted etc.
5 #It is assuming the reBining is linear
6 #We'll use m for the slope an c for the constant.
7 #Awk can handle multiple regexp!
8 BEGIN {
9     m=2.0;#Note: make sure that m>1
10    c=-5;
```

---

<sup>1</sup>The middle section can be repeated multiple times, with multiple regular expressions

<sup>2</sup>More properly the *field*.

## A. SOFTWARE DEVELOPMENT

---

```
11     n=0;
12     count=0;
13 }
14 #This regexp finds the time parameter
15 $0 ~ /#[[:digit:]]+.[[:digit:]]*[:space:]*$/ {
16     t=strtonum(gensub(/#/,"",1))
17     printf "%.6g\n", t
18 }
19 #This one finds the two columns and does the rebining
20 #It can also use the time parameter.
21 $0 ~ /^[[:digit:]]+[:space:]+[[:digit:]]+/ {
22     count += $2;
23     if( ! ((n+c)*m <= $1 && $1 < (n+1+c)*m)){
24     print n, "\t", count;
25     n++;
26     count = 0;
27     }
28 }
29 # END {
30 #     print "#-DONE-";
31 # }
```

Once the proper constants<sup>1</sup> were extracted from the peaks linear relationship, we include them in the script in the BEGIN section.

The program has 2 regular expressions, we are concerned about the second one. Since that is the one doing the actual rebining. It is very *important* to note that the  $m$  (the slope) has to be greater than one. That is, the linear relationship goes from the small bin plot to the large bin plot.

```
1 $0 ~ /^[[:digit:]]+[:space:]+[[:digit:]]+/ {
2     count += $2;
3     if( ! ((n+c)*m <= $1 && $1 < (n+1+c)*m)){
4     print n, "\t", count;
5     n++;
6     count = 0;
7     }
```

---

<sup>1</sup>the  $m$  and the  $c$ .

However, as can be seen from the code, the rebining is done from the large bin set to the smaller one, with the linear constants going from the small to the large bin set.

It is perhaps a bit counterintuitive, but it actually rebins the data in a very clean manner. The count variable gets track of the bin data and stacks them in the corresponding new bin.

It has been observed, that in some cases some bins have unexpected peaks. Specially in the cases where the original bins (`channels`) are very close to the rebined ones.

These peaks have to be trimmed carefully. Software improvements have to be made in order to correct this bug.

## A.2 columnScript

Another simple `Bash` script is `columnScript.sh`, it also uses `AWK` however all the code for it is given in only one line:

```
1 #!/bin/bash
2 #Progress on the script
3
4 tsvFile=tsvForPlotting
5
6 if [ ! -d $tsvFile ]
7 then
8     echo "$tsvFile directory does not exist, creating one."
9     mkdir $tsvFile
10 fi
11
12 for i in *.tsv
13 do
14     echo "Processing $i in $tsvFile/$i"
15     echo \#$(grep "Elapsed Real Time:" $i | cut -f2) > $tsvFile/$i
16     awk '/^[[:digit:]]+[[:space:]]+[[:digit:]]+/{print $0;}' $i >> ←
17     $tsvFile/$i
17 done
18
19 exit 0
```

## A. SOFTWARE DEVELOPMENT

---

It basically creates<sup>1</sup> a directory called `tsvForPlotting`. Looks for the time parameter in the `tsv` file and trims everything else except the column data.

### A.3 matchColumns

The `matchColumns.sh` is actually more powerful than `columnScript.sh`, since it merges many `tsv` files into one it is actually more convenient to plot multiple data files this way since it allows to easily manipulate data in gnuplot (*Note*: the data has to be rebined first, in case it needs it).

```
1 #!/bin/bash
2 #Preparing the rendering file for awk
3 dir=$(dirname $0)
4 $dir/forFormating.sh $@ > $dir/render.awk
5
6 let j=1
7 echo -en "# channel\t"
8 for i in $@
9 do
10  if [ ! -e "$i" ]
11  then
12    echo "Error:$0 The file $i doesn't exist" >&2
13    exit 1
14  fi
15
16  file "$i" | grep ASCII > /dev/null
17  eStatus=$?
18  if [ $eStatus != 0 ]
19  then
20    echo "Error:$0 The file $i is not an ASCII file" >&2
21    exit 1
22  fi
23  #val is temporal and it's used for making temporary files
24  #and pasting them in a single file.
25  val="silly_"$i"_file"
26  echo -en "$( basename "$i" .tsv )\t"
27  if (( "$j" == 1 ));then #for pasting the first column the ↔
    channels
```

---

<sup>1</sup>In case it doesn't already exist



```

28   awk '$0 ~ /^[[:digit:]]+[[:space:]]+[[:digit:]]+/' {print $1,"\t"↵
    , $2,"\t";} ' $i > $val
29   else #only paste the second column
30
31
32   awk '$0 ~ /^[[:digit:]]+[[:space:]]+[[:digit:]]+/' {print $2,"\t"↵
    ;} ' $i > $val
33   fi
34   let j++
35 done
36
37 echo ""
38 #Getting rid of the weird carriage return baheaviour "^M"
39 pr -m -t -s\  silly*_file | awk -f $dir/render.awk
40 #Deleting the temporary files
41 rm silly*_file
42
43 exit 0

```

It uses 3 [AWK](#) programs of which two of them have their source code in the [Bash](#) file!

The program `forFormatting.sh` actually renders the code for the last [AWK](#) program.

```

1  #!/bin/bash
2  # for the render.awk file
3  echo -n "{print "
4  for i in $( seq 1 $# )
5  do
6    if [ "$i" = 1 ]
7    then
8      echo -n "\$$i,"'\t",'"\$"$(( $i+1))
9    else
10     echo -n ', "\t", "'"\$"$(( $i+1))
11   fi
12 done
13
14 echo "};}"
15
16 exit 0

```

## A. SOFTWARE DEVELOPMENT

---

The file it creates is called `render.awk`, as can be seen almost at the top of the `matchColumns.sh` file. A sample `render.awk` file is as the following:

```
1 {print $1,"\t",$2,"\t",$3,"\t",$4,"\t",$5,"\t",$6,"\t",$7,"\t",$8,↵  
   "\t",$9;}
```

It is a format allowing the `matchColumns.sh` to place 9 columns of 8 data sets for plotting in a single file. The first column is reserved for the channel number.

### A.4 isonav

A command line program for nuclear physics calculations. It is still work in progress. And some of the nuclear physics calculations were made using this program. It can be downloaded from:

<https://github.com/ffavela/isonav>



Figure A.1: QR - Scan to go to isonav's github repo.

## Appendix B

# E- $\Delta$ E detector array calibration

```

      *   .--.
      / /  '
+      | |
      ,   \ \__,
      *   + '---' *
      +  /\
+      .' '. *
      *  /=====\  +
      ;:~ _ ;
      |: ( ) |
      |: _ |
+      |: ( ) |      *
      ;:~ _ ;
      .' \:~ / ' .
      / .-'':_.' '-. \
      |/   /||\   \
      jgs _..---""'""'""'---.._
      _.-'""
      _'                               "'-._

```

<http://www.ascii-art.de/ascii/pqr/rockets.txt>

For someone who was never meant for this world I must confess I'm suddenly having a hard time leaving it. Of course they say **“Every atom in our bodies was once part of a star”**. So maybe I'm not leaving... maybe I'm going home.

-*Vincent*  
Gattaca

## B. E- $\Delta E$ DETECTOR ARRAY CALIBRATION

Energy calibration for the telescope detector system shown in figure 4.24 in section 4.2.8.5 is discussed here with more detail. An “ $\Delta E$ ” ORTEC planar detector ( $11\mu\text{m}$ ) was used as “ $\Delta E$ ” and a thicker ( $300\mu\text{m}$ , 60V) CANBERRA PIPS detector as “E”.

Element	$\alpha$ Energy[MeV]	Energy loss [MeV]
$^{239}\text{Pu}$	5.15	2.55
$^{241}\text{Am}$	5.48	2.41
$^{244}\text{Cm}$	5.80	2.29

**Table B.1:** Alpha energy and energy loss in the telescopic detector array.

Table B.1 list part of the results of this analysis. The energy loss in the  $\Delta E$  detector is in agreement with the computer simulation done in SIMION.

The detector and amplifier conditions are briefly shown in table B.2.

Detector	Voltage [V]	Amp. Model	CG	FG	ST
E	+9	??	10	15	2
$\Delta E$	+60	2026	20	10	1

**Table B.2:** Telescope detector array conditions. The threshold for the  $\Delta E$  detector was set at -92mV.

First, the calibration of the E detector was done with the standard triple alpha source, see figure B.1.

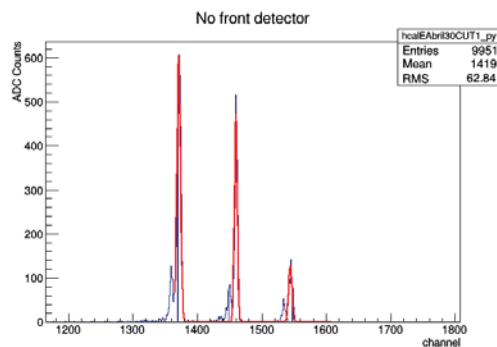


**Figure B.1: Alpha Peak Calibration** - A channel to energy relationship is established for the E detector.

The well known energies of the alpha peaks were identified and a linear relationship was established. Even the back peaks, of the respective first excited level, are shown.

---

Giving the following parameters for the linear relationship.

- $a1=-6.256984$
- $b1=267.217092$
- $E = (y-a1)/b1$

The corresponding plot is shown in figure B.2. Error bars are shown, however they are indeed very small.

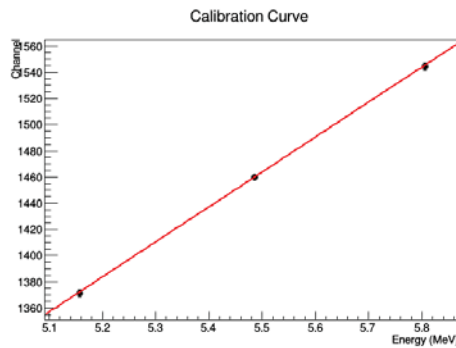


**Figure B.2: Energy to channel relationship** - The linear relationship parameters, between the channel and energy, are found

Later, the  $\Delta E$  detector is placed in front of the E detector. Then the triple alpha source is placed in front of the E detector. A two dimensional plot was generated using the new data and it is shown in figure B.3.

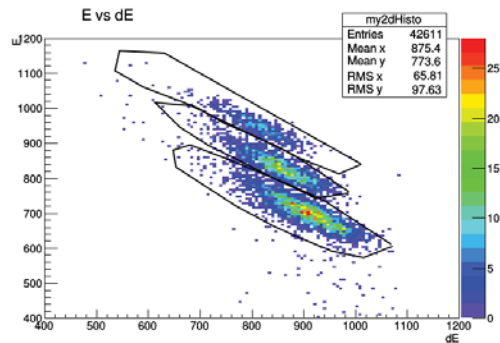


**Figure B.3: 2D histogram for calibration** -  $\Delta E$ -E histogram of the triple alpha source.

## B. E- $\Delta E$ DETECTOR ARRAY CALIBRATION

---

The 3 surrounded regions correspond to the respective alpha energies of the triple alpha source. Doing the projection downwards (E detector) a new histogram is formed (figure ), which clearly differs from figure B.1.

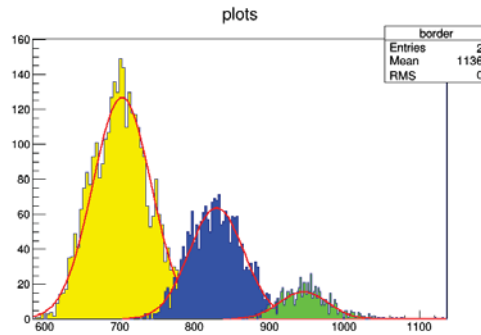


**Figure B.4: E projection** - Projection of the individual peaks with the  $\Delta E$  detector placed in front.

The alpha particles have lost part of their energy in the  $\Delta E$  detector causing the peaks to shift to lower channels and also widen. The energy loss depends on the energy, this is the reason why the peaks start to overlap. Using the linear channel to energy relationship, the peak energies were identified. From there, the energy lost on the front ( $\Delta E$ ) detector was identified (see table B.1).

The energy loss values were used to calibrate the  $\Delta E$  detector. Figure B.5 shows the  $\Delta E$  projection of the 2D histogram.

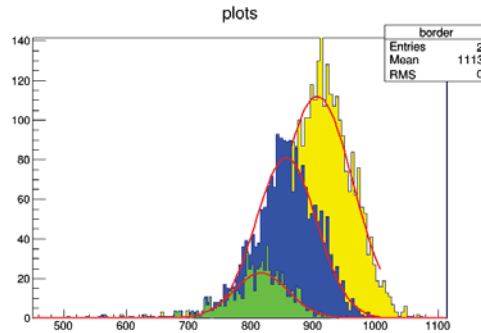


**Figure B.5:  $\Delta E$  projection** - Projection of the individual peaks of the  $\Delta E$  detector.

Same colors in figures B.4 and B.5 mean same alpha particle region. Note that the higher the energy an alpha particle has, the less energy it losses. Also note that

---

if the individual cuts (in figure B.3) were not made, then figure B.5 wouldnt show the 3 different peaks. It would be next to impossible to locate the peaks, except for the tallest one.

Knowing the energies and the peak's channels a new linear parameter fit can be performed, the parameters are:

- $a_2 = 18.775618$
- $b_2 = 348.232846$
- $dE = (x - a_2) / b_2$

The fit was done in ROOT and the corresponding plot is shown in figure B.6, notice that the error bars are wider. The reason for this is that the peaks are wider in the front detector. There is no reason for using the front detector setup for calibrating the back detector (E), the first calibration is much better suited for this.

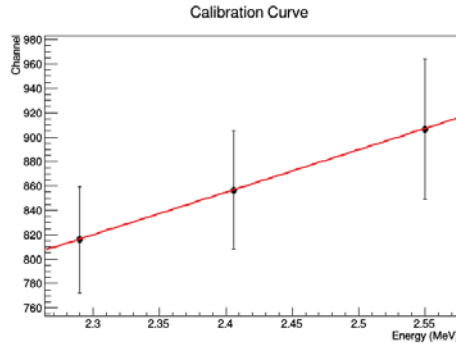


**Figure B.6:  $\Delta E$  calibration** - Energy to channel relationship of the  $\Delta E$  detector.

The calibration information of both detectors is used to make a plot of energy loss vs total energy ( $E_{tot}$ ). Were  $E_{tot} = \Delta E + E$ , a 2D histogram of the calibration is shown in figure B.7.

The alpha regions are now straightened (horizontal) when compared with B.1 (slanted). A projection of the total energy is shown in figure B.8 showing the energy values close to the expected ones.

This gives good confidence that the calibration is good and the experimental data can be calibrated with the obtained parametrization. Notice that the peaks are wider

## B. E- $\Delta$ E DETECTOR ARRAY CALIBRATION

---

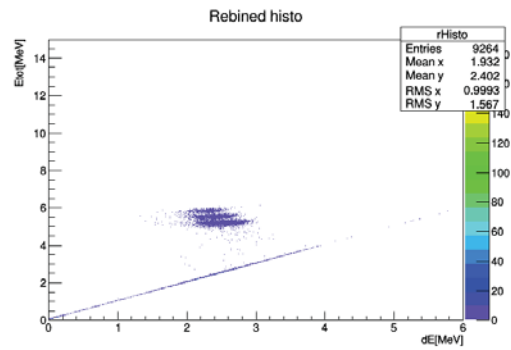


Figure B.7:  $E_{tot}$  vs  $\Delta E$  - Energy loss vs total energy histogram.

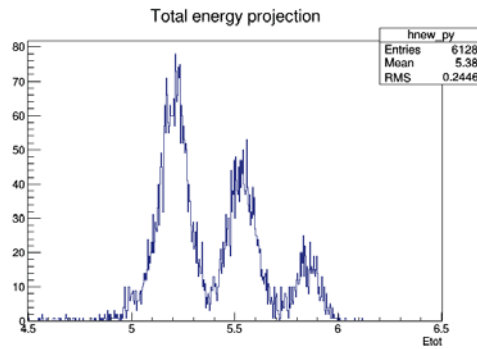


Figure B.8:  $E_{tot}$  projection - Recuperated total energy from the telescope detector array setup.



---

(see figure [B.1](#) for comparison). This is because of the inclusion of the  $\Delta E$  detector, but the loss of resolution is compensated by the ability of creating 2 dimensional histograms that allows us to easily discriminate particles from each other.

A combination of Bash and [ROOT](#) scripts automated the calibration process, by simply loading the file without the front detector and the file with both detectors.

## B. E- $\Delta$ E DETECTOR ARRAY CALIBRATION

---

# Appendix C

## Published Articles

```
- ##.#_## - ##_#.### .- ##.#_## ##.#_##
( ) / ) ##/##/## ( ) #(_#/1### /1 ) ##/11_### / ##/1( )##
( ) ( ) /_ ##|#/## ( ) ##_)##|### 1 /_ ##|#_)## ( ) #'-1#/##
#####
-- #####_### - - #####_### ##_#_### - - ##_#_### . .
/ ##( )### ) ) ##/#_## /1 / ###/## ( _ / \ #(_#_)## /1 /1
/ #####/##### /_ /_ #(_#_)## 1( ) ###/##### _)\_/ ##_#_)## 1'-1
#####
. - #####.### - - ##.#.### - - ##.#_## . - #####_###
/ /1( ) ##/#/1### )/\ ##/1#/1## ( _ ) ##/1#_)## /1( ) ##( _#####
( ) 1( ) #(_#)# /_ \ / ##|###|## ) /_ ##|#_)## '-1( ) #####_###
#####
- ##_#.#.# . - ##_#_### . ##_#_### . ##_#.### - .
|_ #####|#/1## /1 / \ #####|#_)## / /1 ##_)##/# / / ##_)#|### ( _ /1
_) ##/_#|#|## 1 \ / ##/_#_)## ( )'-1 ##_)##/# ##_'-1( ) ##_#|#|### )'-1
#####
. - ##.#_## - - ##.#_## - - ##_#_### . ##.#_## . ##.#_##
/1 / / \ ##/1( )## ) ( ) ##/1( )## ) ##)##/# /1 ##/1##/##
'-1 ( ) \ / ##|#/## ) ( ) #'-1#_)## ) /_ ##/_#/# ##_'-1 #'-1#/##
#####
- ##_#_### . . ##.#.### - . #####_### - ##_#_### - -
_) ##_#_### /1 /1 ##/1#/1## ) /1 #####_### ) / #(_#_### ) / \
_) ##_#_###/'-1'-1 #'-1|##|## /_'-1 #####_### ) ( ) ##_#_### ) \ /
#####
- . - ##_#_### - ##_#_### - ##_#_### - ##_#_###
) /1 ) #(_#( )## ) ##_#_)## ) ( ) #(_#/#/# ) / ##_)1_###
( \ ==- /_ '-1 /_ ##_#_### /_ ##_#_)## /_ ( ) ##_#_### /_ ( ) ##_#_#_)##
// . \ #####
( ( \ \ . ##### . - ##.#_## - - ##_#_### - . ##_#_### -
) ) '\_ ) /1 ##|/1### /1 / \ ##/1#_)## ( _ ( ) ##|)_### ) /1 ##|)_### ( _ /
( / \ \ 1 #####|#####'-1 \ / #'-1|#_)## ) ( ) ##/_#_)## )'-1 ##_#_#/# ##_#_#_)##
| | #####
) =====
}===== {      ^      -      -      -      -      -      -      -      -
( _ _ _ _ _ ) / - \ 1 ) / - 1 \ 1_ 1_ 1_ / / 1_1
```

“Daring ideas are like chessmen moved forward. They may be beaten, but they may start a winning game.”

– *Johann Wolfgang von Goethe*

German writer

## C. PUBLISHED ARTICLES

---

Links to some of the articles published through this project.



**Figure C.1:** Phys. Rev. ST - <http://journals.aps.org/prab/abstract/10.1103/PhysRevSTAB.18.123502>



**Figure C.2:** X LASNPA - [http://pos.sissa.it/archive/conferences/194/051/X%20LASNPA\\_051.pdf](http://pos.sissa.it/archive/conferences/194/051/X%20LASNPA_051.pdf)



**Figure C.3:** Cocoyoc 1 - <https://iopscience.iop.org/article/10.1088/1742-6596/492/1/012010/meta;jsessionid=9841717F8C72C27F3AC6859E9CA98023.c1.iopscience.cld.iop.org>



**Figure C.4:** Cocoyoc 2 - <https://iopscience.iop.org/article/10.1088/1742-6596/578/1/012001/meta>

**C. PUBLISHED ARTICLES**

---

# References

- [1] D. SHAPIRA, J.L.C. FORD JR., R. NOVOTNY, B. SHIVAKUMAR, R.L. PARKS, AND S.T. THORNTON. **The HHIRF supersonic gas jet target facility.** *Nucl. Instr. and Meth. in Physics Research Section A: Accelerators, Spectrometers, Detectors and Associated Equipment*, **228(23)**:259–266, 1985. 4
- [2] D. SHAPIRA, J.GOMEZ DEL CAMPO, J.L.C. FORD JR, B. SHIVAKUMAR, P.H. STELSON, B.A. HARMON, R.L. PARKS, AND S.T. THORNTON. **Nuclear physics experiments with the ornl-hhirf supersonic gas jet target.** *Nucl. Instr. and Meth. in Physics Research Section B: Beam Interactions with Materials and Atoms*, **1011, Part 1(0)**:436–440, 1985. 4
- [3] H.W. BECKER, L. BUCHMANN, J. GÖRRES, K.U. KETTNER, H. KRÄWINKEL, C. ROLFS, P. SCHMALBROCK, H.P. TRAUTVETTER, AND A. VLEIEK. **A supersonic jet gas target for  $\gamma$ -ray spectroscopy measurements.** *Nucl. Instr. and Meth. in Phys. Res.*, **198(23)**:277–292, 1982. 4, 28
- [4] K.A. CHIPPS, U. GREIFE, D.W. BARDAYAN, J.C. BLACKMON, A. KONTOS, L.E. LINHARDT, M. MATOS, S.D. PAIN, S.T. PITTMAN, A. SACHS, H. SCHATZ, K.T. SCHMITT, M.S. SMITH, AND P. THOMPSON. **The Jet Experiments in Nuclear Structure and Astrophysics (JENSA) gas jet target.** *Nuclear Instruments and Methods in Physics Research Section A: Accelerators, Spectrometers, Detectors and Associated Equipment*, **763**:553–564, 2014. 4
- [5] ANTONIOS KONTOS, DANIEL SCHÜRMANN, CHARLES AKERS, MANOEL COUDER, JOACHIM GÖRRES, DANIEL ROBERTSON, ED STECH, RASHI TALWAR, AND MICHAEL WIESCHER. **HIPPO: A supersonic helium jet gas target for nuclear astrophysics.** *Nucl. Instr. and Meth. in Phys. Res. S. A*, **664(1)**:272–281, 2012. 4, 116
- [6] J J DAS, H K CARTER, J R BEENE, AND B M SHERRILL. **Helium jet ion source in FRIB era.** *Journal of Physics: Conference Series*, **420(1)**:012165, 2013. 4
- [7] ALFONSO MARTÍNEZ BACA. *Blanco de gas sin paredes para reacciones nucleares.* Tesis para obtener el título de físico, U.N.A.M. Facultad de ciencias, México D.F., 1964. 4
- [8] A. DI LEVA, M. DE CESARE, D. SCHRMANN, N. DE CESARE, A. D’ONOFRIO, L. GIALANELLA, R. KUNZ, G. IMBRIANI, A. ORDINE, V. ROCA, D. ROGALLA, C. ROLFS, M. ROMANO, E. SOMORJAI, F. STRIEDER, AND F. TERRASI. **Recoil separator ERNA: Measurement of  $3\text{He}7\text{Be}$ .** *Nucl. Instr. and Meth. in Physics Research Section A: Accelerators, Spectrometers, Detectors and Associated Equipment*, **595(2)**:381–390, 2008. 4
- [9] S. R. SALISBURY, G. HARDIE, L. OPLIGER, AND R. DANGLE. **Proton-Oxygen Differential Scattering Cross Sections. II.** *Phys. Rev.*, **126**:2143–2147, Jun 1962. 4
- [10] P. HARTIGAN, J. M. FOSTER, B. H. WILDE, R. F. COKER, P. A. ROSEN, J. F. HANSEN, B. E. BLUE, R. J. R. WILLIAMS, R. CARVER, AND A. FRANK. **Laboratory Experiments, Numerical Simulations, and Astronomical Observations of Deflected Supersonic Jets: Application to HH 110.** *The Astrophysical Journal*, **705(1)**:1073, 2009. 4
- [11] SHIH-CHIEH LO. **Numerical simulations of supersonic jet flows**, 2010. Copyright - Copyright ProQuest, UMI Dissertations Publishing 2010; Última actualización - 2012-07-05; Primera página - n/a; M3: Ph.D. 4
- [12] AL-QADI AND IBRAHEEM M. *Three-dimensional numerical simulation of a supersonic under-expanded rectangular jet.* PhD thesis, Ohio State University, 2003. 4, 31
- [13] L. BARRÓN-PALOS AND ET AL. **Absolute cross sections measurement for the  $^{12}\text{C} + ^{12}\text{C}$  system at astrophysically relevant energies.** *Nuclear Physics A*, **779**:318–332, 2006. 4
- [14] L. BARRÓN-PALOS AND ET AL., editors. *The 4th International Conference on Exotic Nuclei and Atomic Masses*, 2005. 4
- [15] L. BARRÓN-PALOS AND E. CHÁVEZ L. **Low-energy cross section measurements through detection of secondary gamma emission and thick target.** *Rev. Mex. Phys.*, **50**:18–23, December 2004. 4
- [16] C. R. BRUNE, W. H. GEIST, R. W. KAVANAGH, AND K. D. VEAL. **Sub-Coulomb  $\alpha$  Transfers on  $^{12}\text{C}$  and the  $^{12}\text{C}(\alpha, \gamma)^{16}\text{O}$  S Factor.** *Phys. Rev. Lett.*, **83**:4025–4028, Nov 1999. 4
- [17] P. ROSALES AND E.F AGUILERA. **Sub-Coulomb fusion excitation function for  $^{12}\text{C} + ^{12}\text{C}$ .** *Rev. Mex. Phys.*, **49**:88–91, August 2003. 4
- [18] A. LEMUT, D. BEMMERER, F. CONFORTOLA, R. BONETTI, C. BROGGINI, P. CORVISIERO, H. COSTANTINI, J. CRUZ, A. FORMICOLA, ZS. FÜLÖP, G. GERVINO, A. GUGLIEMMETTI, C. GUSTAVINO, GY. GYRKY, G. IMBRIANI, A.P. JESUS, M. JUNKER, B. LIMATA, R. MENEGAZZO, P. PRATI, V. ROCA, D. ROGALLA, C. ROLFS, M. ROMANO, C. ROSSI ALVAREZ, F. SCHÜMANN, E. SOMORJAI, O. STRANIERO, F. STRIEDER, F. TERRASI, AND H.P. TRAUTVETTER. **First measurement of the  $^{14}\text{N}(p, \gamma)^{15}\text{O}$  cross section down to 70 keV.** *Phys. Lett. B*, **634(56)**:483–487, 2006. 5
- [19] A FORMICOLA, G IMBRIANI, H COSTANTINI, C ANGULO, D BEMMERER, R BONETTI, C BROGGINI, P CORVISIERO, J CRUZ, P DESCOUVEMONT, Z FÜLÖP, G GERVINO, A GUGLIEMMETTI, C GUSTAVINO, G GYRKY, A.P JESUS, M JUNKER, A LEMUT, R MENEGAZZO, P PRATI, V ROCA, C ROLFS, M ROMANO, C ROSSI ALVAREZ, F SCHÜMANN, E SOMORJAI, O STRANIERO, F STRIEDER, F TERRASI, H.P TRAUTVETTER, A VOMIERO, AND S ZAVATARELLI. **Astrophysical S-factor of  $^{14}\text{N}(p, \gamma)^{15}\text{O}$ .** *Phys. Lett. B*, **591(12)**:61–68, 2004. 5
- [20] **Gran Sasso National Laboratory.** Gran Sasso official site. [online] [http://www.lngs.infn.it/lngs\\_infn/index.htm?mainRecord=http://www.lngs.infn.it/lngs\\_infn/contents/lngs\\_en/public/about/](http://www.lngs.infn.it/lngs_infn/index.htm?mainRecord=http://www.lngs.infn.it/lngs_infn/contents/lngs_en/public/about/). 5

## REFERENCES

- [21] A. FORMICOLA, G. IMBRIANI, M. JUNKER, D. BEMMERER AND R. BONETTI, C. BROGGINI, C. CASELLA, P. CORVISIERO H. COSTANTINI, G. GERVINO, C. GUSTAVINO, A. LEMUT P. PRATI, V. ROCA, C. ROLFS, M. ROMANO, D. SCHÜRSMANN F. STRIEDER, F. TERRASI, H.-P. TRAUTVETTER, AND S. ZAVATARELLI. **The LUNA II 400kV accelerator**. *Nucl. Instr. and Meth. in Physics Research Section A: Accelerators, Spectrometers, Detectors and Associated Equipment*, **507**(3):609–616, 2003. 5
- [22] D.S. TODD, D. LEITNER, M. LEITNER, R. MARUYAMA, P.A. VETTER, AND K.N. XU. **Design of the low energy astrophysics research facility CLAIRE**. *Nucl. Instr. and Meth. in Physics Research Section B Beam Interactions with Materials and Atoms*, **261**(1-2):544–548, 2007. The Application of Accelerators in Research and Industry Proceedings of the Nineteenth International Conference on The Application of Accelerators in Research and Industry Nineteenth International Conference on The Application of Accelerators in Research and Industry. 5
- [23] D.D. CLAYTON. *Principles of Stellar Evolution and Nucleosynthesis*. University of Chicago Press, 1968. 5
- [24] H. REEVES. *Stellar evolution and nucleosynthesis*. Documents on modern physics. Gordon and Breach, Science Publishers, 1968. 5
- [25] GARY STEIGMAN. *Light Element Nucleosynthesis*. IOP Publishing, 2006. 5
- [26] CARMEN ANGULO. *Experimental Tools for Nuclear Astrophysics*. Springer Berlin Heidelberg, 2009. 5
- [27] R.D. HOFFMAN AND T. RAUSCHER, editors. *Proceedings of the International Conference on Nuclear Data for Science and Technology*, October 2001. 5
- [28] BLAIR C. STRINGFELLOW, ADAM T. BUJAK, D.DUANE CARMONU Y.H. CHUNG, JAMES E. FINN, LASZLO J. GUTAY, ANDREW S. HIRSCH MOHAMED MAHI, GARY L. PADEREWSKI, NORBERT T. PORILE AND THOMAS C. SANGSTER, ROLF P. SCHARENBERG, AND FRANK TURKOT. **Accelerator internal target experiments using a supersonic gas jet**. *Nucl. Instr. and Meth. in Phys. Res. S. A*, **251**(2):242–253, 1986. 5
- [29] ULRICH WIEDNER. **The PANDA experiment at FAIR**. *Nucl. Phys. B*, **147**(0):119–123, 2005. HIF 2004 Proceedings of the High Intensity Frontier Workshop. 5
- [30] A. J. KONING AND J. P. DELAROCHE. **Local and global nucleon optical models from 1 keV to 200 MeV**. *Nucl. Phys. A*, **713**:231–310, January 2003. 8
- [31] JOSÉ FRANCISCO FAVELA PÉREZ. *Efectos no nucleares en interacciones de neutrones con blancos pesados*. Tesis para obtener el título de físico, U.N.A.M. Facultad de ciencias, México D.F., 2007. 8, 10
- [32] PENÉLOPE RODRÍGUEZ ZAMORA. *Estudio teórico-experimental de la dispersión elástica de neutrones en plomo a ángulos pequeños*. Tesis para obtener el título de físico, U.N.A.M. Facultad de ciencias, México D.F., 2008. 8, 10
- [33] GERALD A. MILLER. **Charge Densities of the Neutron and Proton**. *Phys. Rev. Lett.*, **99**:112001, Sep 2007. 8
- [34] VALERY V. NESVIZHEVSKY. **Quantum states of neutrons in the Earth’s gravitational field**. *Nature*, **415**:297–299, January 2002. 8
- [35] ALEJANDRO FRANK, PIET VAN ISACKER, AND JOAQUIN GÓMEZ-CAMACHO. **Probing additional dimensions in the universe with neutron experiments**. *Phys. Lett. B*, **582**:15–20, February 2004. 10
- [36] J.E DOSKOW AND F SPERISEN. **Development of internal jet targets for high-luminosity experiments**. *Nucl. Instr. and Meth. in Physics Research Section A: Accelerators, Spectrometers, Detectors and Associated Equipment*, **362**(1):20–25, 1995. Proceedings of the 17th World Conference of the International Nuclear Target Development Society. 10, 84, 116
- [37] K.S. KRANE. *Introductory Nuclear Physics*. Wiley, 1987. 18, 19, 23
- [38] PETER EKSTRÖM. **Nuclear structure and decay data**. Web application for Q values. 19
- [39] PETER EKSTRÖM. **Isotope Explorer**. Software for database nuclear analysis. The link may be broken, their main page (<http://ie.lbl.gov/>) says that due to lack of funds they may close in 2013. 20
- [40] M. COTTEREAU AND F. LEFEBVRES. *Recueil de problèmes de physique nucléaire et de physique des particules*. Masson et Cie, 1971. 22
- [41] C M H SMITH. **The power of the Sun**. *Eur. J. Phys.*, **4**(3):134, 1983. 23
- [42] D.K. NADYOZHIN. **Gamow and the physics and evolution of stars**. *Space Science Reviews*, **74**(3-4):455–461, 1995. 23
- [43] P.J. PRITCHARD. *Fox and McDonald’s Introduction to Fluid Mechanics*. John Wiley & sons, 2011. 28, 30
- [44] J. A. D. ACKROYD. *Fluid mechanics considerations in supersonic jet target design*. Science Research Council, DARESBURY LABORATORY, 1975. 28
- [45] A.H. SHAPIRO. *The dynamics and thermodynamics of compressible fluid flow*. Number v. 1 in The Dynamics and Thermodynamics of Compressible Fluid Flow. Ronald Press Co., 1953. 28
- [46] T BOTTO, M BOUWHUIS, D DIMITROYANNIS, M DOETS, C.W DE JAGER, R.L.J VAN DER MEER, M SCHARLOO, H DE VRIES, B.E NORUM, AND T.P WELCH. **Supersonic gas jets as internal targets at NIKHEF**. *Nucl. Instr. and Meth. in Physics Research Section A: Accelerators, Spectrometers, Detectors and Associated Equipment*, **362**(1):26–31, 1995. Proceedings of the 17th World Conference of the International Nuclear Target Development Society. 31
- [47] E.T. VERKHOVTSOVA, E.A. BONDARENKO, V.I. YAREMENKO, AND YU.S. DORONIN. **The effect of non-equilibrium gas condensation in vuv spectra of electron-excited supersonic argon jet**. *Chem. Phys. Lett.*, **97**(45):483–487, 1983. 36
- [48] G. S. SETTLES. *Schlieren and shadowgraph techniques*. Springer, 2001. 36, 69
- [49] A. ROTH. *Vacuum technology*. North-Holland Physics Publishing, second edition edition, 1986. 37
- [50] GERHARD LEWIN. **An elementary introduction to vacuum technique**. *American Vacuum Society monograph series*, 1987. 37



## REFERENCES

---

- [51] W. MERZKIRCH. *Flow Visualization*. Academic Press, 1987. 69
- [52] K. HATANAKA AND T. SAITO. **Influence of nozzle geometry on underexpanded axisymmetric free jet characteristics**. *Shock Waves*, **22**(5):427–434, 2012. 81
- [53] H. MOOSMÜLLER, G. C. HERRING, AND C. Y. SHE. **Two-component velocity measurements in a supersonic nitrogen jet with spatially resolved inverse Raman spectroscopy**. *Optics Lett.*, **9**:536–538, 1984. 82
- [54] R. BRUN, F. RADEMAKERS, ET AL. **ROOT web page**, <http://root.cern.ch/>, 2001. 103